2013

A Strategy for Minimizing Parkinsonian Noise from a Joystick Controlled Wheeled Mobile Robot

Fabian Just
Purdue University, walbijust@gmx.net

Graduate School ETD Form 9
(Revised 12/07)

PURDUE UNIVERSITY
GRADUATE SCHOOL
Thesis/Dissertation Acceptance

This is to certify that the thesis/dissertation prepared

By Fabian Just

Entitled
A Strategy for Minimizing Parkinsonian Noise from a Joystick Controlled Wheeled Mobile Robot

For the degree of Master of Science in Electrical and Computer Engineering

Is approved by the final examining committee:

RAYMOND A. DECARLO, Co-Chair
Chair

MILOS ZEFRAN, Co-Chair

MICHAEL D. ZOLTOWSKI

To the best of my knowledge and as understood by the student in the *Research Integrity and Copyright Disclaimer (Graduate School Form 20)*, this thesis/dissertation adheres to the provisions of Purdue University's "Policy on Integrity in Research" and the use of copyrighted material.

Approved by Major Professor(s): RAYMOND A. DECARLO, Co-Chair

Approved by: V. Balakrishnan 10/7/2013
Head of the Graduate Program Date

A STRATEGY FOR MINIMIZING PARKINSONIAN NOISE FROM A JOYSTICK CONTROLLED WHEELED MOBILE ROBOT

A Thesis

Submitted to the Faculty

of

Purdue University

by

Fabian Just

In Partial Fulfillment of the

Requirements for the Degree

of

Master of Science in Electrical and Computer Engineering

December 2013

Purdue University

West Lafayette, Indiana

ACKNOWLEDGMENTS

The author would like to thank Professor Ray DeCarlo for his permanent support and the time and energy dedicated to this project. His consistent encouragement has made this project a possibility.

The author also thanks Professor Richard Meyer for assistance in programming and his significant help.

TABLE OF CONTENTS

Page

Page

LIST OF TABLES

LIST OF FIGURES

Figure Page

Figure Page

SYMBOLS

d	Distance to the wall
d_{ref}	Reference distance to the wall
F_x	Forward ground reaction force
F_y	Sideways ground reaction force
F_{static}	Static friction force
g	Gravitational acceleration
I_b	Inertia of the body
I_v	Inertia of a wheel around the center of rotation
I_w	Inertia of a wheel
m_w	Mass of a wheel
m_b	Mass of the body
r	Radius of a wheel
u_1	Torque of the right wheel
u_2	Torque of the left wheel
v_x	Forward velocity
v_y	Sideways velocity
v_r	Relative velocity
v_{ref}	Reference velocity
$\overline{x}_c$	Center of rotation
θ	Angle between forward direction and x-axis
ω	Turning velocity

ABSTRACT

Just, Fabian M.S.E.C.E., Purdue University, December 2013. A Strategy for Minimizing Parkinsonian Noise from a Joystick Controlled Wheeled Mobile Robot . Major Professor: Raymond A. DeCarlo.

This thesis investigates movement of an electric wheelchair as a wheeled mobile robot (WMR) with a battery rechargeable through regenerative braking.The WMR has two wheels, each of which can propel or brake. This leads to four modes of operation: propel-propel, brake-brake, propel-brake, and brake-propel. Braking can be either done by a propelling wheel using negative torques or by regenerative braking which also applies a negative torque.

The thesis begins with a presentation of the WMR model. Performances Indices (PI) are introduced as metrics for specific driving scenarios. For almost all scenarios, the PI is used in a model predictive control (MPC) strategy for the following set of scenarios with and without noisy measurements on the distance to a wall which simulate a noisy sensor measurement for:

-a wall following scenario
-a wall cornering scenario
-a combined scenario

Results of a combined scenario with Parkinsonian noise on distance to the wall measurements and velocity with and withoutthe use of a notch filter are presented and interpreted.

Finally Parkinsonian noise is imposed on a joystick wheelchair control scenario with and without the use of a notch filter.

The central result of this thesis is to erase the Parkinsonian tremor from the input of the joystick of a electric wheelchair to improve the life quality of disabled users.

1. WHEELED MOBILE ROBOT SYSTEMS AND PARKINSON'S DISEASE: BACKGROUND AND INTRODUCTION OF RESEARCH OBJECTIVES

1.1 Introduction of the problem in general terms

People with Parkinson's disease have problems with interacting with their environment. Specifically in regards to limb tremors. The most simple all-day tasks like eating, drinking and writing can become difficult and exhausting problems. Elderly people, who are the main target group of this disease, need help and lose more and more independence. Devices like personal computers, smartphones and electric wheelchairs are built to make life easier and strengthen our communication and movement abilities. All these devices have input/output interfaces. A correct handling of these interfaces is needed to obtain the desired support for people who suffer from Parkinson's disease.

The Parkinsonian tremors are especially responsible for incorrect input signals to the above named interface devices. This makes it nearly impossible for some Parkinson patients to drive safely with an electric wheelchair. In this thesis the effect of Parkinson Disease tremor on the joystick controller of an electric wheelchair are analyzed and a solution to the underlying control problem is given. The goal of this thesis is to minimize the influence of the disease tremor on a joystick operated wheelchair and to make it possible for the wheelchair to operate as if it's users were having no tremors in their limbs. The idea and algorithms presented in this thesis are not only valid for electric wheelchairs, but might apply for other devices like personal computer mouse devices and smartphones. We note that a wheeled mobile robot (WMR) is used synonymously with an electric wheelchair.

1.2 Past work in the research area

1.2.1 Parkinson's disease tremor

The Parkinson's disease (PD) is caused by a degenerative dysfunction of the central nervous system. For PD the tremor is the most significant symptom. It is necessary to mention that the exact medical origin of Parkinson's disease remains unknown. [1] Classical Parkinsonian tremor is defined as a rest tremor and postural/kinetic tremor. Both tremors have a slightly different frequency. Mostly the rest tremor is inhibited during movement and may reoccur at the same frequency when adopting a fixed posture. [2] The cardinal frequency range of the tremor is between 3 Hz ad 6 Hz, but the exact frequency depends on multiple factors. [3]. Actually it is possible that in the early stage of the illness the tremor frequency is between 3 Hz and 9 Hz. [2] After the early stage, where the cells are attacked for the first time and the impact on the tremor is causing more fluctuations, the tremor frequency is in a more steady frequency range.

Another interesting characteristic of PD is a gained freedom of pattern movements. Normal humans can't execute rhythm patterns simultaneously with different frequencies and only professional musicians are trained to deal with these frequency dissociations. People with PD in general have more frequency independence in that involuntary tremor movements, because they can occur synchronously with other independent wanted movements in the same limb. An interesting fact is that if you consider a different tremor frequency at an arm (5.2 Hz) and at a leg (3.8 Hz) and the contralateral arm has to perform for example tapping movements at 2 Hz, we will recognize a common frequency of 4.6 Hz in the specific arm and leg. This implies the existence of more than one oscillator system in the brain. It shows that the frequency dissociation in PD of different limbs imply more degrees of independence, but a stimulation with a special frequency can influence and change another contralateral PD tremor frequency. [4]

For our investigations the tremor of the wrist is important. Given test data shows that the tremor with the highest consistency overall involved wrist flexors in PD. The instantaneous frequency for one test user is 4.3 Hz $\pm$ 0.05 Hz for 102 out of 120 time periods of 0.5 s. [4] This shows the extraordinary consistency of the wrist tremor of PD. In the case of electric wheelchairs a user gives input values to the system with a controlled joystick. For the movement of the joystick, mostly the wrist flexors are used, because the rest of the arm is lying on an arm rest. For the research objective to erase the tremor caused by PD given on the input joystick of a WMR, these results emphasize the stationary behavior of the specified tremor frequency. In this thesis a Parkinsonian main frequency of 3.8 Hz is used, because it is a common frequency for Parkinsonian wrist tremor. [5]

It is important to know that the overall frequencies of PD decrease for the rest tremor at 0.09 $\frac{\text{Hz}}{\text{year}}$ and for PD postural tremor at about 0.08 $\frac{\text{Hz}}{\text{year}}$. [6] This suggests that an adaptive filter is the long term objective of this first study.

As a main result out of these investigations, it is possible to obtain the tremor frequency of a PD user during a test trial and then adapt the software to this frequency. Another main result is a recognized bias in the Parkinsonian noise affecting the movements, which can be erased to achieve better results. As we have seen the frequency is steady state and slowly decreasing over years. More clinical data is needed to determine the frequency variation during WMR operations. With this technique we can improve the driving ability of a PD user immensely by using adaptive notch filtering.

1.2.2 Wheeled mobile robot systems

A wide and challenging research area is motion planning with an underlying WMR dynamic system. Therefore robot dynamics have to be derived to build up a high fidelity simulation model. [7] A system of states, algebraic variables and constants

with physical content is modeled and can be used with different driving modes and switches to perform sliding and rolling movements. [8]

There are approaches for driving scenarios like modeling and feedback linearizing control of an autonomous powered wheelchair for a wall following and a cornering scenario. Infrared sensors are used to get information about the distance to the wall and wheel encoders give exact measurements of angular velocities of the wheels. [9] Standard electric wheelchair skill tests are used to estimate the behavior of the user and joystick signals are sampled at 200 Hz. [10]

1.3 Structure of the thesis

After starting with a discussion about the dynamics of the WMR, autonomous switches for the WMR wheels are introduced in chapter 2. Four modes of operation are used: propel-propel, brake-brake, propel-brake, and brake-propel. A high fidelity simulator based on projection is developed and the model is validated with acknowledged research results. In chapter 3, wall following driving scenarios with the electric wheelchair are presented. Regarding to safety issues of a human user these scenarios are efficiently solved. Model predictive control (MPC) is introduced and used to solve the same scenarios. In chapter 4 a cornering scenario is introduced. Additionally a combined scenario with two wall following parts and a cornering part in the middle is solved via MPC. Random Gaussian noise is added on this scenario to count for distance to the wall measurement errors of sonar sensors. In chapter 5, Parkinsonian like noise is added to the distance and velocity references to mimic the joystick input behavior of a user with PD. With erasing the bias and the use of a constructed notch filter, the Parkinsonian tremor is filtered out of the input of the joystick. Plots with and without filtering of the simulated driving scenarios are compared. In Chapter 6, real joystick data is taken as the reference and Parkinsonian noise is added on it to simulate the same scenarios with human joystick input data. Again the posi-

tive impact of the used filtering strategies are shown. In chapter 7, further research perspectives are shown. Improvements of the used model, modes and strategies are described and explained.

2. HILARE WHEELED MOBILE ROBOT MODEL

In this chapter the concept of the Hilare Robot Model is presented and the state equations of the robot model are derived. All characteristics and abilities of the used system model is described. The system is compared with acknowledged research results, after it is implemented in MATLAB.

2.1 Robot dynamics and equations of the Hilare Robot Model

The robot dynamics and structure of the robot model is introduced and with different shown scenarios the state equations of the robot model are properly derived. Autonomous switches for the wheels for changes between rolling and sliding are introduced and integrated in the system.

2.1.1 Robot Dynamics

The Hilare Robot Model consists of two wheels treated as right circular cylinders with radius r and a rectangular parallelepiped body with length and width equal to $2L$. The red arrow in Fig. 2.1. shows the forward direction of the WMR and the wheels are marked with their reference number. For the robot model it is important to define I_w as the moment of inertia of a wheel around its rotational axis, I_b as the moment of inertia of the square cube body and I_v as the moment of inertia of a wheel

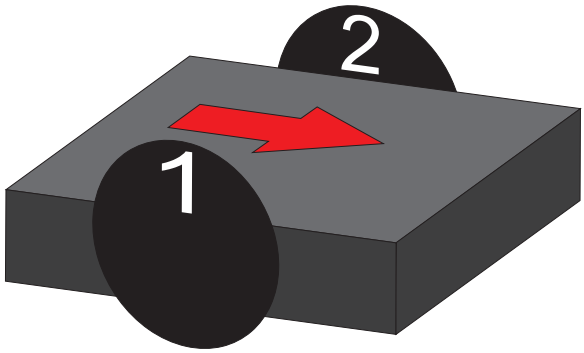

Fig. 2.1. Isometric 3D view of the WMR

around the center of rotation of the whole WMR. That means for the calculation of inertias: [11]

$$\begin{aligned} I_b &= \frac{2L^2 m_b}{3} \\ I_w &= \frac{r^2 m_w}{2} \\ I_v &= m_w \left(\frac{r^2}{4} + L^2 \right) \end{aligned} \tag{2.1}$$

These formulas are important for the derivation of the state equations. The mass of a wheel will be defined as m_w and the mass of the WMR body will be stated as m_b. For further considerations and because of clarity arguments it is necessary to define a total inertia I_t and a total mass m_t of the WMR with the following connection.

$$\begin{aligned} I_t &= I_b + 2I_v \\ m_t &= m_b + 2m_w \end{aligned} \tag{2.2}$$

It is important to mention that the used robot model includes regenerative braking for every wheel individually and natural drag caused by friction forces, which will all be introduced precisely in further explanations.

2.1.2 Derivation of the state equations

The used Hilare Robot Model has two independently driven wheels. Every wheel of the WMR can either slide or roll depending on the magnitude of the constraint forces and friction coefficients. Every wheel related variable will be marked with the related wheel number. The control inputs $u = (u_1, u_2)$ drive wheels 1 and 2 with the power provided by a rechargeable battery pack. [8] The following graph shows how the velocities v_x and v_y are integrated into the coordinate system.

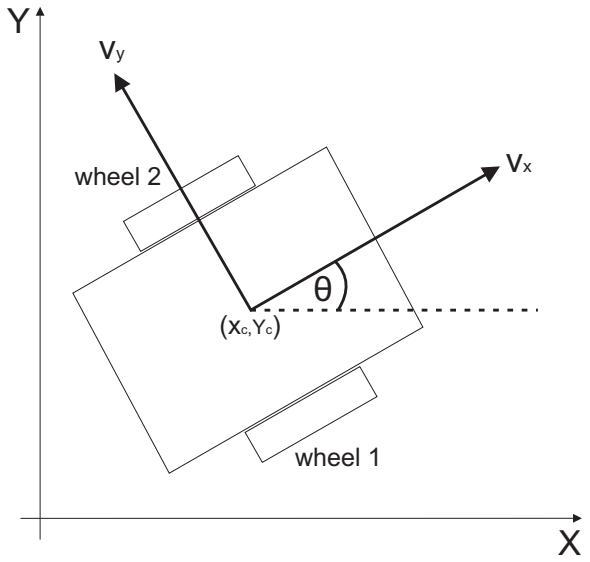

Fig. 2.2. Orientation of used robot velocities based on the coordinate system

A positive velocity v_x implies a forward movement consequently a negative v_x indicates a backward movement. A positive velocity v_y means a sliding drive to the left and a negative velocity v_y indicates a sliding drive to the right. The point $\overline{x}_c$ =(x_c,y_c) is the center of rotation of the WMR and will be considered as the center of reference for all equations. By inspection the following state equations can be derived:

$$\dot{x_c} = v_x \cos(\theta) - v_y \sin(\theta) \tag{2.3}$$

$$\dot{y_c} = v_x \sin(\theta) + v_y \cos(\theta) \tag{2.4}$$

The turn velocity ω is defined as follows:

$$\dot{\Theta} = \omega \tag{2.5}$$

This means a forward left turn results in a positive ω and for a forward right turn a negative turning velocity ω follows. By derivation of (2.3) and (2.4) and considering the related ground reaction forces the next two state equations describing the derivatives of the WMR velocities in the local robot coordinate system can be constructed. As seen in Fig. 2.2 the formulas for the velocities are:

$$\dot{v}_x = \omega v_y + \frac{F_{x1} + F_{x2}}{m_t} \tag{2.6}$$

$$\dot{v}_y = -\omega v_x + \frac{F_{y1} + F_{y2}}{m_t} \tag{2.7}$$

The following state equations have to be derived with the existing wheel forces equilibrium equations. Fig. 2.3 shows these components of wheel 1. The direction v_x indicates the forward direction. A positive input u_1 causes an acceleration in the

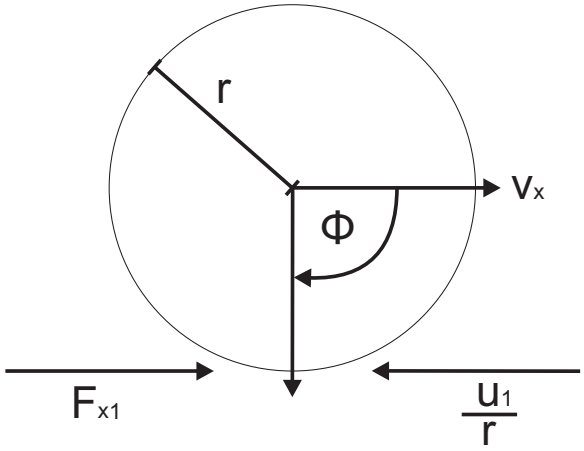

Fig. 2.3. Wheel 1 with radius r and considered angle ϕ

forward direction. The ground reaction force F_{x1} works against the input torque u_1 and has do be considered in the equilibrium force equation. By inspection you can see that the applied input torque minus the ground force multiplied with the radius

of the wheel has to be the inertia of the wheel multiplied with the rotation velocity of the considered wheel. The state equations for the rotation velocities of the wheel 1 and wheel 2 arising out of these equilibriums are:

$$\dot{\mathrm{w}}_1 = \frac{-F_{x1}r + u_1}{I_w} \tag{2.8}$$

$$\dot{\mathrm{w}}_2 = \frac{-F_{x2}r + u_2}{I_w} \tag{2.9}$$

The last of the eight state equations describing the WMR model delineates the behavior of the derivative of the turning velocity ω. As already mentioned a forward left curve causes a positive turning velocity. If a positive derivative of this velocity is wanted, the ground reaction force of the right wheel has to be higher than the ground reaction force of the left wheel. For the derivation you have to consider the inertia of the whole system introduced in equation (2.2) as I_t. It follows the equation:

$$\dot{\omega} = L\frac{F_{x1} - F_{x2}}{I_t} \tag{2.10}$$

As already mentioned the input to the presented robot system are the input torques $u_1, u_2 \epsilon [-60, 60]$. When the regenerative brake is on, the input torques slow the WMR down depending on the rotation velocity of the related wheel. [8]

$$u_{(i)} = \begin{cases} -K_b \mathrm{w}_i, & \text{if } |\mathrm{w}_i| \leq 6 \\ -60\mathrm{sgn}(\mathrm{w}_i) & \text{if } |\mathrm{w}_i| > 6 \end{cases} \quad i = 1, 2 \tag{2.11}$$

A drag function is added to the model. The input torques have to be subtracted by the rotation velocity of related wheel multiplied by a constant to imitate the drag behavior on arbitrary grounds. In this thesis $c = 0.09$ is used.

$$\begin{aligned} u_1 &= u_1 - \mathrm{w}_1 c \\ u_2 &= u_2 - \mathrm{w}_2 c \end{aligned} \tag{2.12}$$

2.1.3 Derivation of the algebraic variables for rolling wheels

For the difference between the rolling and sliding mode it is important to introduce relative velocities. They are zero if there is no difference between movements caused by the rotation of the wheel and the total movement in the coordinate system. This means the following formula has to hold:

$$v_{r1,r2} = \begin{pmatrix} v_{rx1,rx2} \\ v_{ry1,ry2} \end{pmatrix} = \begin{pmatrix} v_x \pm L\omega - rw_{1,2} \\ v_y \end{pmatrix} = \begin{pmatrix} 0 \\ 0 \end{pmatrix} \tag{2.13}$$

To present the equation for the ground reaction forces F_{x1}, F_{x2}, F_{y1} and F_{y2} in the rolling mode, the formula (2.13) is derived in the next equation.

$$\begin{pmatrix} \dot{v_x} + L\dot{\omega} - r\dot{w}_1 \\ \dot{v_x} - L\dot{\omega} - r\dot{w}_2 \\ \dot{v_y} \end{pmatrix} = \begin{pmatrix} 0 \\ 0 \\ 0 \end{pmatrix} \tag{2.14}$$

With insertion of the affiliated state equations and solving the system of equations the wanted ground reaction forces are:

$$F_{x1} = \frac{I_w L^2 m_t \left(r\left(u_1 + u_2\right) - 2I_w v_y \omega\right) + I_t r \left(m_t r^2 u_1 + I_w \left(u_1 - u_2 - m_t r v_y \omega\right)\right)}{\left(2I_w L^2 + I_t r^2\right)\left(2I_w + m_t r^2\right)} \tag{2.15}$$

$$F_{x2} = \frac{I_w L^2 m_t \left(r\left(u_1 + u_2\right) - 2I_w v_y \omega\right) + I_t r \left(m_t r^2 u_2 - I_w \left(u_1 - u_2 + m_t r v_y \omega\right)\right)}{\left(2I_w L^2 + I_t r^2\right)\left(2I_w + m_t r^2\right)} \tag{2.16}$$

The ground reaction forces in y direction $F_{y1} = F_{y2} = \frac{Fy}{2}$ is defined with the equation:

$$F_{y1} = F_{y2} = \frac{\omega v_x m_t}{2} \tag{2.17}$$

2.1.4 Derivation of the algebraic variables for sliding wheels

In the sliding mode the relatives velocities are not zero. This could be in a scenario, where the WMR has less grip because of the ground, velocity, acceleration or other operating forces.

$$v_{r1,r2} = \begin{pmatrix} v_{rx1,rx2} \\ v_{ry1,ry2} \end{pmatrix} = \begin{pmatrix} v_x \pm L\omega - rw_{1,2} \\ v_y \end{pmatrix} \neq \begin{pmatrix} 0 \\ 0 \end{pmatrix} \tag{2.18}$$

In the sliding mode the ground reaction forces originiate from Coulomb's law. [8]

$$F_{x1} = \mu_d \frac{m_t g}{2\|v_r^i\|} v_{rx1} \tag{2.19}$$

$$F_{x2} = \mu_d \frac{m_t g}{2\|v_r^i\|} v_{rx2} \tag{2.20}$$

$$F_{y1} = \mu_d \frac{m_t g}{2\|v_r^i\|} v_{ry1} \tag{2.21}$$

$$F_{y2} = \mu_d \frac{m_t g}{2\|v_r^i\|} v_{ry2} \tag{2.22}$$

With these equations the algebraic variables in the sliding mode are described. For the modeling of a flexible WMR wheel system, which can change between the two modes, rules for the change between them have to be set up. The static friction force is important as a limit for the applied forces to secure rolling for the WMR. The formula can be easily derived with the gravitational acceleration $g = 9.81$, the static coefficient of static friction μ_s and the total mass m_t of the WMR.

$$F_{static} = \frac{m_t}{2} \mu_s g \tag{2.23}$$

In this consideration an autonomous switching process from rolling to sliding of wheel 1 or wheel 2 occurs, when the related magnitude of the constraint force $F_{1,2} = \begin{pmatrix} F_{x1,x2} & F_{y1,y2} \end{pmatrix}$ is higher as the magnitude of the static friction $F_{static} < \|F_{1,2}\|$.

For the change from sliding to rolling two conditions have to apply. First the magnitude of the constraint force of the appropriate wheel has to be lower or equal to the magnitude of static friction $F_{static} \geq \|F_{1,2}\|$ and second the relative velocity of the related wheel 1 or wheel 2 has to be zero.

$$v_{r1,r2} = 0 \tag{2.24}$$

If these equations hold, then the related wheel mode switches to rolling again.

2.1.5 Introduction of mode projection

For the use of cost functions and control in the next chapters four different modes $v_i, i = 1, 2, 3, 4$ have to be initialized.

$$\begin{aligned} v_1 &= \text{wheel 1 propelling and wheel 2 propelling} \\ v_2 &= \text{wheel 1 propelling and wheel 2 braking} \\ v_3 &= \text{wheel 1 braking and wheel 2 propelling} \\ v_4 &= \text{wheel 1 braking and wheel 2 braking} \end{aligned} \tag{2.25}$$

All mode values $v_i, i = 1, 2, 3, 4$ have to sum up to 1 to be a valid mode structure $v_1 + v_2 + v_3 + v_4 = 1$, which is a convex combination of the modes. Every scenario uses the associated formulas for each wheel and has independent variables for the calculation of the whole setting. The mode with the highest $v_i, i = 1, 2, 3, 4$ has the biggest impact on the actual torque given on the system. With a projection method, shown in the next section, the input torques u_1 and u_2 are calculated and integrated in the high fidelity simulator.

2.2 Implementation and comparison with proved research results

In this section the implementation of the WMR model in the programming environment MATLAB is shown and results are compared with known research results of Prof Zefran from University of Illinois at Chicago.

2.2.1 Simulink and MATLAB implementation

One way of approaching the problem is a implementation in Simulink.

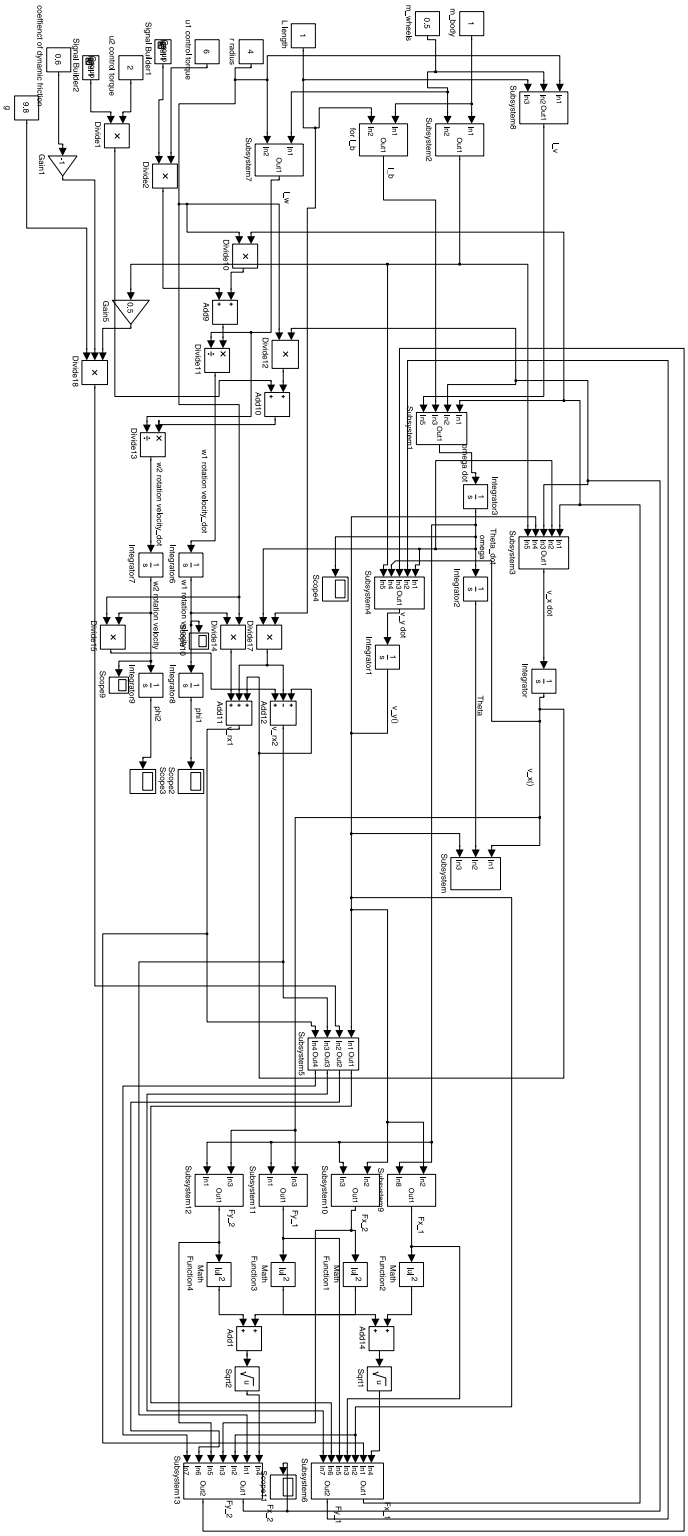

Fig. 2.4. Simulink model

Fig. 2.4 gives a short overview over the implementation of the model with all implied bigger subsystems described as boxes too. Because of the mass of blocks and subsystems needed, the higher complexity of the system is easy to see. A lot of simulation time was needed to finish easy tasks, due to the amount of calculations and the way of subsystem integration in Simulink. This approach has a big weakness, when model changes occur. Code can easily be changed, but the structure of a Simulink model sometimes needs to change radically. This is why for the simulations in the next chapter a coding approach is taken, which is more clear and better performing in simulation time. For the simulation in MATLAB the nonstiff differential equations solver ode23 is used. This solver is used for high fidelity simulations in every following chapter too. The implementation is devided in two programs.

The first program contains the equations. This function has as an input the element time t, the states x, actual input torques u_1 and u_2 and the needed physical constants. Every needed constant and algebraic variable is calculated. All result values are inserted into the state equations and the derived state vector $\dot{x}$ is given back to the main function.

This main function is the second program, which includes the call of the ode23 solver. Starting conditions for the states are given and updated each call of the equation solver. The time intervals for t can be varied and input torques for the WMR system are calculated there. Everything is included in a for loop, because it is necessary to call ode23 consistently until the simulated time interval ends.

This coding approach is more clear and better performing in simulation time. Changes to the program can easily be integrated.

2.2.2 Comparison with acknowlegded research results

Professor Zefran's simulation results are used for this comparison. [8] With this given torque data it is possible to start the same simulations with the ode23 nonstiff differential equations solver. Therefore it is necessary to change the main function to a loop to enter input data for the solver about the regenerative brakes and input torques for the wheels used. For every following simulation in the thesis the following projection method is used for the imposed input torques u_1 and u_2 on the WMR:

$$\begin{aligned} u_1 &= u_{11}v_1 + u_{12}v_2 + u_{13}v_3 + u_{14}v_4 \\ u_2 &= u_{21}v_1 + u_{22}v_2 + u_{23}v_3 + u_{24}v_4 \end{aligned} \tag{2.26}$$

In Professor Zefran's datasets the regenerative braking signifier is a boolean variables, where 1 means regenerative brake of related wheel is on and 0 that the regenerative brake is off. Drag is not used in Professor Zefran's simulations, but as already shown it is possible to add this for following considerations in the next chapters. Prof. Zefran's input torque sequence for the simulation is used as the input for the simulation

With the given data the WMR is starting with the center of rotation at $(x_c, y_c) = (0, 4)$ in the coordinate system with both wheels in the sliding mode. The used constant values for this simulation are $m_b = 1$, $m_w = 0.5$, $L = 1$, $r = 4$, $\mu_d = 0.6$, $\mu_s = 0.7$ and $g = 9.8$ and the used initial state is $z_0^T = (x_0, y_0, \theta_0, v_{x,0}, v_{y,0}, \omega_0, w_{1,0}, w_{2,0})^T = (0, 4, 1, 1, 2, 0, 0.5, 1)^T$. All the data is one to one taken from Prof. Zefran's data.

The given input torques get both wheels back into the rolling mode and the robot stops at the origin. The differences in the trajectories, as seen in Fig. 2.5, lie in the different equation solvers used and in not exact equal conditions for a change between rolling and sliding, but it shows that the used underlying code is correct and can be used as a basis for upcoming WMR simulations.

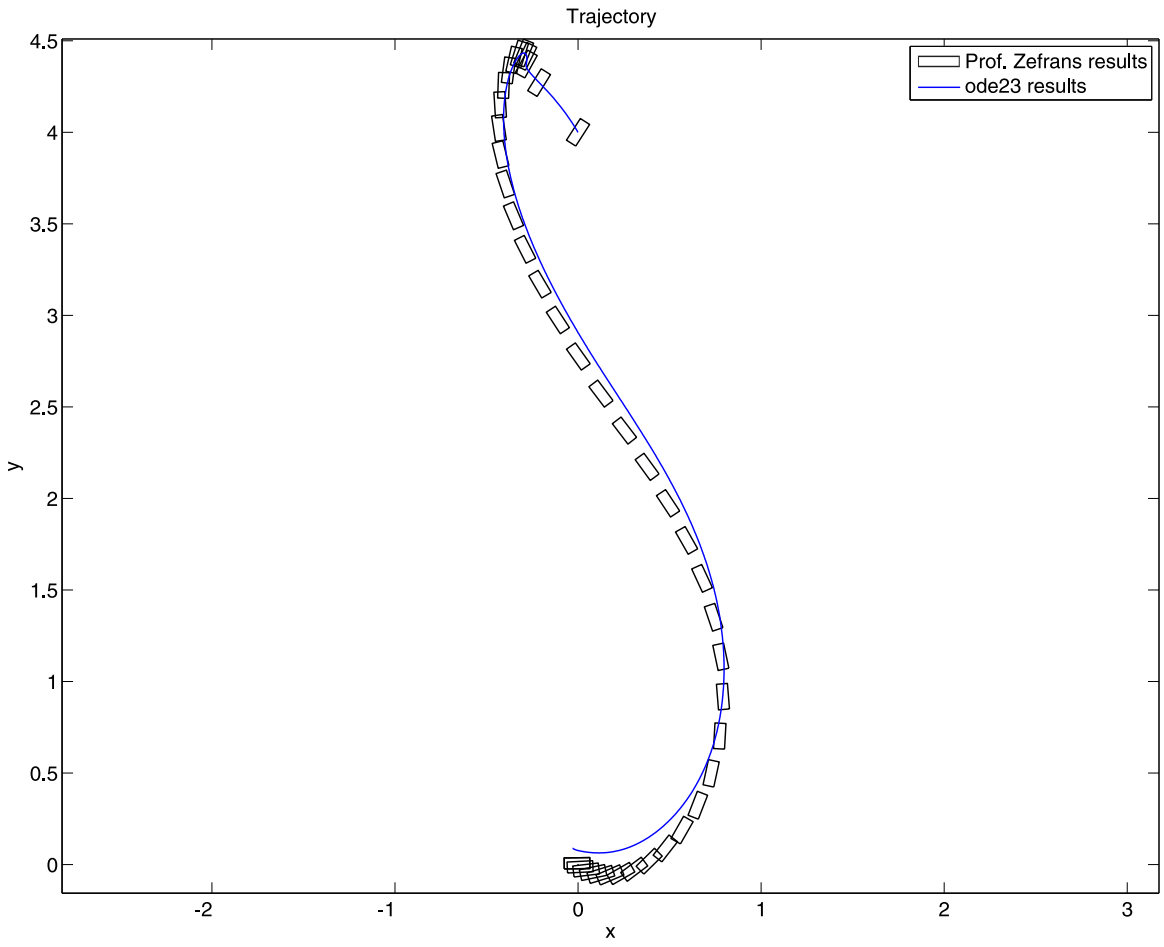

Fig. 2.5. Comparison between Prof. Zefran's results and ode23 results

3. CONTROL STRATEGIES FOR THE WALL FOLLOWING SCENARIO

In this chapter driving scenarios for electric wheelchairs with exact measurements of the environment are presented and needed variables for the simulation are derived. The results of controlled simulations are presented and differences are discussed.

3.1 The wall following scenario

In this section the wall following scenario will be presented. First the Performance Index is developed and constants for the simulation are chosen. Simulation results will be shown to evaluate the driving behavior of the WMR.

3.1.1 Introduction of the wall following scenario

This scenario is set in a cartesian coordinate system as in Fig. 3.1. The WMR with the center of rotation (x_c, y_c) should have the distance d_{ref} to the wall, which is shown as the shaded area in Fig. 3.1. R is an offset of the wall from the origin of the coordinate system. The objective is to drive the WMR from an initial point $(x_c(t_0), y_c(t_0)) = (x_0, y_0)$ to a final point $(x_c(t_F), y_c(t_F)) = (x_F, y_F)$ along a trajectory parallel to the wall, but with a distance d_{ref} from the wall. The angle of the wall in the coordinate system is arbitrary, but denoted by the value of $90° - \gamma$. $d = d(t)$ denotes the actual distance from the center of rotation of the WMR to the wall as shown in Fig. 3.1.

Movement requires velocity and human safety requires bounds on the velocity and

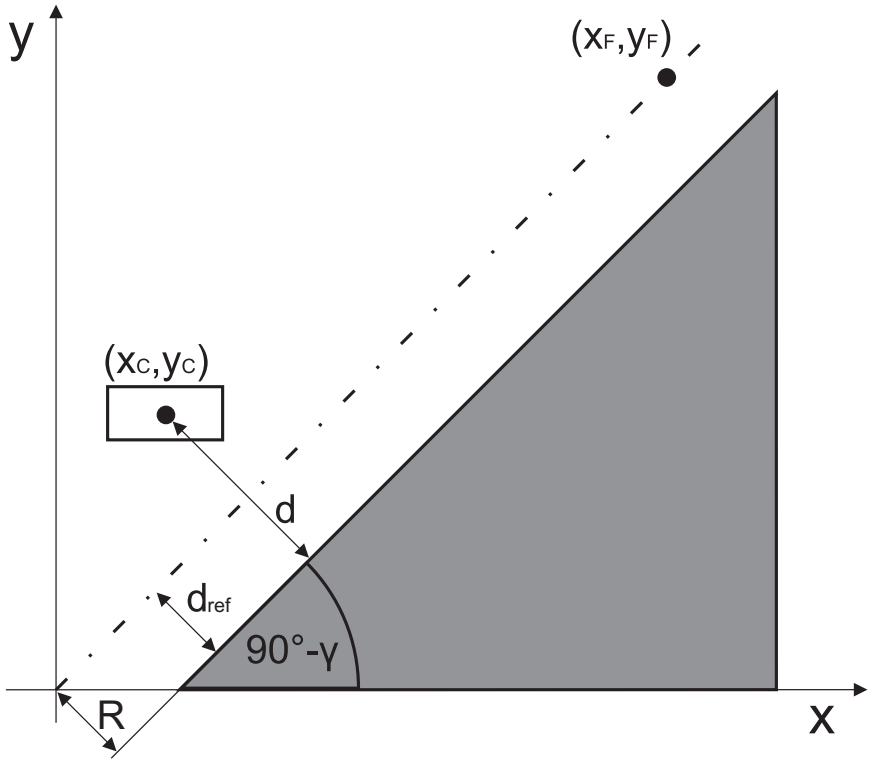

Fig. 3.1. Geometry of wall following scenario

its derivative. For the investigation in this chapter the safety bound for the forward velocity is orientated at the maximum speed of the electric wheelchairs:

$$|v_x(t)|^2 = \left(1.8\frac{\mathrm{m}}{\mathrm{s}}\right)^2 \tag{3.1}$$

The velocities $v_x(t)$ and $v_y(t)$ are the velocities in respect to the local coordinate system of the robot, whereas x and y and their derivative denote the global cartesian coordinate system. If a parallel wall following with $90° - \gamma = 45°$ and $\theta = 45°$ is considered, the axis bounds $\dot{x}(t)$ and $\dot{y}(t)$ as seen in equation (2.3) and (2.4) for movement in the coordinate system have the same value. The maximum speed of $1.8\frac{\mathrm{m}}{\mathrm{s}}$ from a standstill should be reached in a minimum time of 2s to fulfill safety preconditions. Therefore bounds on the forward acceleration require:

$$|\dot{v_x}(t)| \leq 0.9\frac{\mathrm{m}}{\mathrm{s}^2} \tag{3.2}$$

Finally for a maximum of safety, sliding should be prevented. We require that the following inequalities for the ground reaction force F_i of the i'th wheel of the WMR is satisfied:

$$|F_i| \leq F_{static} = \mu_s \left(\frac{m_b}{2} + m_v \right) g \tag{3.3}$$

In the next subsection we take up the problem of intuitively developing the needed PI to achieve wall following as in Fig 3.1.

3.2 Heuristic Development of the Performance Index

3.2.1 Introduction of the general form of Performance Indices

The Performance Index (PI) typically has an integral quadratic form

$$J = \int_{t_0}^{t_f} \left(c_1 \left[\text{Errors} \right]^2 + c_2 \left[\text{Energy Consumption} \right]^2 \right) dt \tag{3.4}$$

Possible "errors"-terms in the integrand of equation (3.4) include:

(i) the distance to the wall w.r.t. a reference:
$(d_{ref}(t) - d(t))$

(ii) the orientation of the robot in regards to the angle θ:
$(\theta_{ref}(t) - \theta(t))$

(iii) the magnitude of the WMR's forward velocity:
$(v_{ref}(t) - v_x(t))$

(iv) the distance to a final stopping point:

$$\left\| \begin{bmatrix} x_F(T) \\ y_F(T) \end{bmatrix} - \begin{bmatrix} x(t) \\ y(t) \end{bmatrix} \right\|_2$$

Of course there are many other types of errors not discussed here.

3.2.2 Wall following with a final point

Specific to the wall following scenario with a final point the first squared error of the PI is the distance to the final goal $\overline{x}_F(T) = [x_F(T), y_F(T)]^T$, given by the equation:

$$c_{xf}(\overline{x}_F(T) - \overline{x}(t))^T(\overline{x}_F(T) - \overline{x}(t)) \tag{3.5}$$

This part of the integrand is normalized on the quadratic distance between the starting point $\overline{x}(t_0)$ and the final point $\overline{x}_F(T)$.

$$c_{xf}\frac{(\overline{x}_F(T) - \overline{x}(t))^T(\overline{x}_F(T) - \overline{x}(t))}{(\overline{x}_F(T) - \overline{x}(t_0))^T(\overline{x}_F(T) - \overline{x}(t_0))} \tag{3.6}$$

A second error used in this PI integrand is:

$$c_d\left(d_{ref} - d(t)\right)^2 \tag{3.7}$$

This part of the PI is normalized on the quadratic reference distance to the wall.

$$c_d\left(\frac{d_{ref} - d(t)}{d_{ref}}\right)^2 \tag{3.8}$$

In this chapter we assume that $d(t)$ is known exactly computed through formulas set forth in appendix A3.1. In particular from equation (3.26) we note that the exact distance of the center of the WMR to the wall is:

$$d(x_c, y_c, \gamma) = \cos(\beta) \cdot \sqrt{x_c^2 + y_c^2} + R \tag{3.9}$$

With Fig. 3.23 and equation (3.26) the angle β is given by:

$$\beta = 180^\circ - \gamma - \arctan\left(\frac{y_c}{x_c}\right) \tag{3.10}$$

The same result for $d(t)$ can be achieved by taking the equation of the wall as a line and calculate the distance to a arbitrary point, here the center of rotation $\overline{x}(t) = [x_c(t), y_c(t)]^T$ is used as well as the slope m and the y-intercept value b of the wall as seen in equation (3.11).

$$y_{wall} = mx_{wall} + b \tag{3.11}$$

The formula has the following form and for the presented wall following scenario $m = 1$ and $b = -\sqrt{(2)}$ are used:

$$d(x_c(t), y_c(t), m, b) = \frac{\|y_c(t) - mx_c(t) - b\|}{\sqrt{(m^2 + 1)}} \tag{3.12}$$

A removal of the absolutes in the nominator would give to possibility to have a positive distance to the wall as a normal case and a negative distance to the wall, when the robot is located physically in the wall.

With attached wheel encoders every movement in the cartesian coordinate system is known as well as the starting point of the WMR. The control problem is to find $u_1(t)$, $u_2(t)$, $v_1(t)$, $v_2(t)$, $v_3(t)$ and $v_4(t)$ so that J_{Wall} in equation (3.14) is minimized over the interval $[0, T]$:

$$\min_{u_i, v_i} J_{Wall} \tag{3.13}$$

Subject to:

(i) model equations of chapter 2

(ii) constraint equations of section 3.1

(iii) $T = 10$ s

(iv) $\overline{x}(t_0) = [x(t_0), y(t_0)]^T = [1, 0.5]^T$

(v) $\overline{x}_F(T) = [x_F(T), y_F(T)]^T = [10, 10]^T$

(vi) $\sum_{i=1}^{4} v_i(t) = 1$

For the wall following mode with a chosen final point the PI can be taken as:

$$J_{Wall} = \int_0^T c_{xf} \frac{(\overline{x}_F(T) - \overline{x}(t))^T (\overline{x}_F(T) - \overline{x}(t))}{(\overline{x}_F(T) - \overline{x}(t_0))^T (\overline{x}_F(T) - \overline{x}(t_0))} + c_d \left(\frac{d_{ref} - d(t)}{d_{ref}} \right)^2 dt \tag{3.14}$$

$$d(t) = \sqrt{(x(t) - x_{minwall}(t))^2 + (y(t) - y_{minwall}(t))^2} \tag{3.15}$$

Where the point $(x_{minwall}(t), y_{minwall}(t))$ is the point on the wall with the minimum distance to the center of rotation of the WMR. The vector $\overline{x}_F(T)$ is the already introduced final goal to reach for the WMR in the Interval from 0 to T. In our example it

is a point in a hallway with the wanted distance $d_{ref} = 1$ to the wall, $\overline{x}_F(T) = (10, 10)$.

The constants c_{xf} and c_d are the weight parameters for the performance index. They indicate tradeoffs in penalizing deviations from d_{ref} and the distance to the final point. This is interesting, because the presence of the final point penalty and its high impact on the PI drives the WMR automatically to the final goal. These constants influence the whole trajectory of the electric wheelchair. They should be chosen wisely, so that the ride for the user is comfortable and practicable.

3.2.3 Wall following with a final point and a velocity profile

In this subsection an addition to the introduced wall following PI is demonstrated. A velocity references is added to the PI to control the velocity on the way to the final goal. This should secure a smooth drive for the test user. The additional part for the PI is:

$$c_v \left(\frac{v_{ref}(t) - v_x(t)}{v_{ref,max}} \right)^2 \tag{3.16}$$

The constant c_v is the weight factor of the velocity profile and the velocity reference in shown in Fig. 3.2. The constant $v_{ref,max} = 1\frac{\mathrm{m}}{\mathrm{s}}$ is the maximum velocity in the velocity profile of Fig. 3.2.

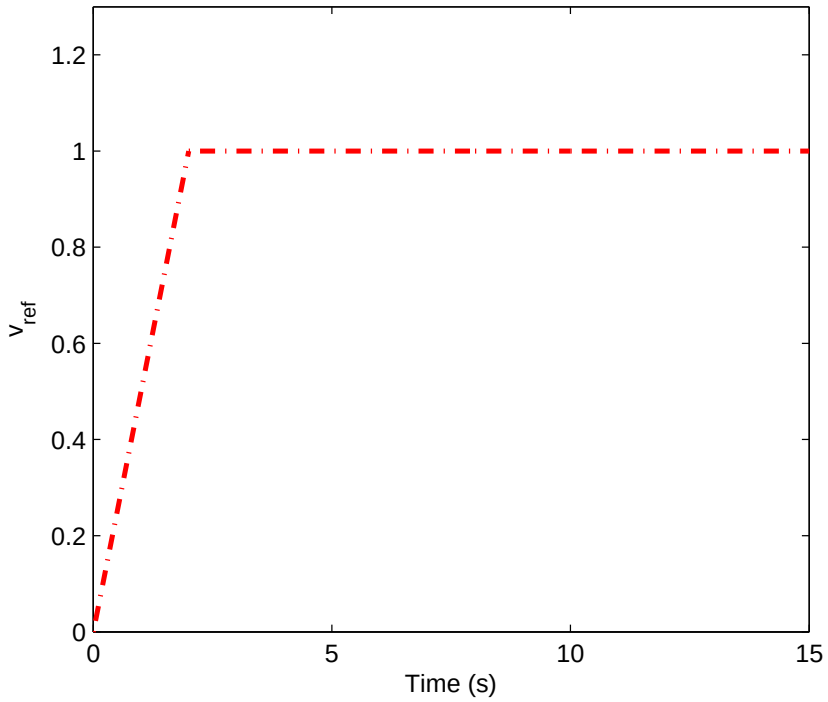

Fig. 3.2. Velocity profile for the finite PI

This means for the total PI:

$$J_{FinWall} = \int_0^T \left[c_{xf} \frac{(\overline{x}_F(T) - \overline{x}(t))^T (\overline{x}_F(T) - \overline{x}(t))}{(\overline{x}_F(T) - \overline{x}(t_0))^T (\overline{x}_F(T) - \overline{x}(t_0))} + c_d \left(\frac{d_{ref} - d(t)}{d_{ref}} \right)^2 + c_v \left(\frac{v_{ref}(t) - v_x(t)}{v_{ref,max}} \right)^2 \right] dt \tag{3.17}$$

3.2.4 Infinite wall following

Again the distance to the wall is a very important part of the PI. The earlier used normalized squared error to d_{ref}:

$$c_d \left(\frac{d_{ref} - d(t)}{d_{ref}} \right)^2 \tag{3.18}$$

The PI for the infinite wall following mode doesn't has a final point penalty as part of the integrand. Rather we use a reference angle and a reference velocity. The reference angle squared error:

$$c_\theta \left(\theta_{ref} - \theta(t)\right)^2 \tag{3.19}$$

The angle θ_{ref} is the angle of the wall in the coordinate system with respect to the x-axis, because a parallel movement of the WMR is wanted. Thus the angle $\theta(t)$ is the actual angle of the robot with respect to the x-axis. Any deviations from the reference angle are penalized by the PI. It is not convenient to normalize this term, because the reference angle θ_{ref} could be zero. The second new part of the PI integrand is a magnitude velocity reference:

$$c_v \left(v_{ref}(t) - v(t)\right)^2 \tag{3.20}$$

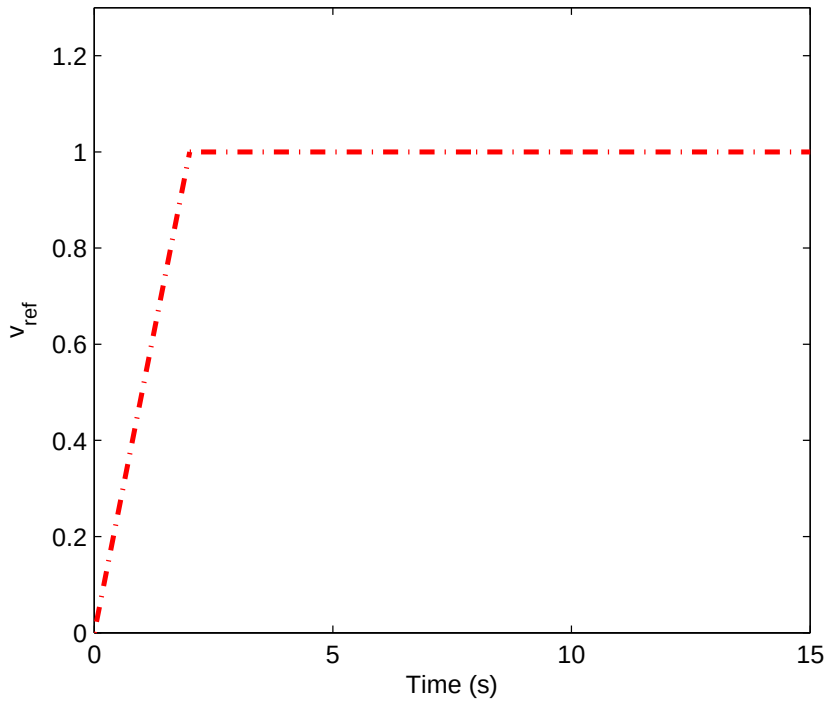

Fig. 3.3. Velocity profile for the infinite PI

The profile in Fig. 3.3 is the identical profile of the finite point scenario. This part of the PI is normalized with the maximum reference velocity $v_{ref,max} = 1\frac{\mathrm{m}}{\mathrm{s}}$ as seen in Fig. 3.3. A reference velocity is needed, because there is no specified final point. Thus after the WMR reaches its nominal speed of $1\frac{\mathrm{m}}{\mathrm{s}}$, it maintains its velocity. The velocity profile is chosen carefully, because additionally it shows a reference velocity. These references are defined within the bounds of velocity and derivative of velocity defined in equation (3.2).

$$c_v \left(\frac{v_{ref}(t) - v_x(t)}{v_{ref,max}} \right)^2 \tag{3.21}$$

In total the PI of the infinite wall following scenario is:

$$J_{InfWall} = \int_0^T \left[c_d \left(\frac{d_{ref} - d(t)}{d_{ref}} \right)^2 + c_\theta \left(\theta_{ref} - \theta(t) \right)^2 + c_v \left(\frac{v_{ref}(t) - v_x(t)}{v_{ref,max}} \right)^2 \right] dt \tag{3.22}$$

For the following simulations it is possible to combine the two different PI's to one and it is only necessary to add the values of the constants to make clear, what the scenario is all about.

$$\begin{aligned} J_{Total} = \int_0^T \Bigg[& c_{xf} \frac{(\overline{x}_F(T) - \overline{x}(t))^T (\overline{x}_F(T) - \overline{x}(t))}{(\overline{x}_F(T) - \overline{x}(t_0))^T (\overline{x}_F(T) - \overline{x}(t_0))} + c_d \left(\frac{d_{ref} - d(t)}{d_{ref}} \right)^2 \\ & + c_\theta \left(\theta_{ref} - \theta(t) \right)^2 + c_v \left(\frac{v_{ref}(t) - v_x(t)}{v_{ref,max}} \right)^2 \Bigg] dt \end{aligned} \tag{3.23}$$

To obtain the infinite wall following PI only the constant c_{xf} has to be set to zero. For the scenario with a final point c_θ and c_v should be equal to zero. For the finite wall following scenario with a final point only c_θ should be zero.

3.3 Simulation results with introduced PI

3.3.1 Wall following with a final point

The trajectory of the wall following scenario with a final point with the parameters $c_{xf} = 10$, $c_d = 1.5$ and $c_\theta = c_v = 0$ are shown below. The continuous blue line

represents the wall, the doted red line represents the wanted distance to the wall and the black continuous curve shows the trajectory of the WMR.

This scenario using the PI opf equation (3.14) is optimized over the whole interval of 10 s.The numerical solution uses a discretization based on collocation over 100 partitions of a 10 s interval. That means each partition is 0.1 s in length. The behavior of the WMR shows that it wants to reduce the distance to the wall to the smallest possible and simultaneously drive to the final goal at $x_F(T) = (10, 10)$ as fast as possible. With the assumed safety bounds on the WMR this result mimics also the behavior of a human in a driving task.

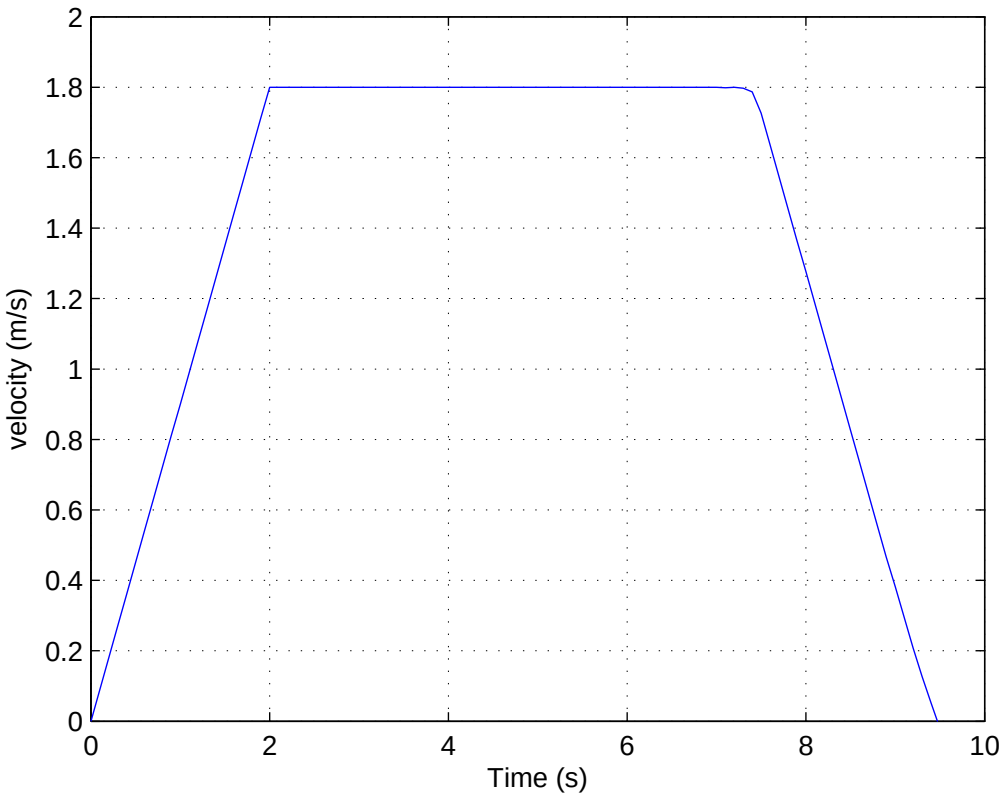

Fig. 3.4. WMR embedded solution forward velocity in the optimal solution scenario

The forward velocity plot in Fig. 3.4 shows that the robot wants to reach the maximum speed of 1.8 $\frac{\text{m}}{\text{s}}$ as fast as possible with the maximum allowed acceleration of 0.9 $\frac{\text{m}}{\text{s}^2}$. It reaches 1.8 $\frac{\text{m}}{\text{s}}$ in 2 s. The velocity stays at the maximum value until the WMR nears the final point.

After 8 s the WMR slows down to stop at the final point $x_F(T) = (10, 10)$. It slows down, because the scenario is slowed over a fixed time interval and a overshoot of the final point would raise the total cost of the PI. As a result out of this process we obtain the minimum cost of the PI. The cost in this simulation is $J = 34.243$.

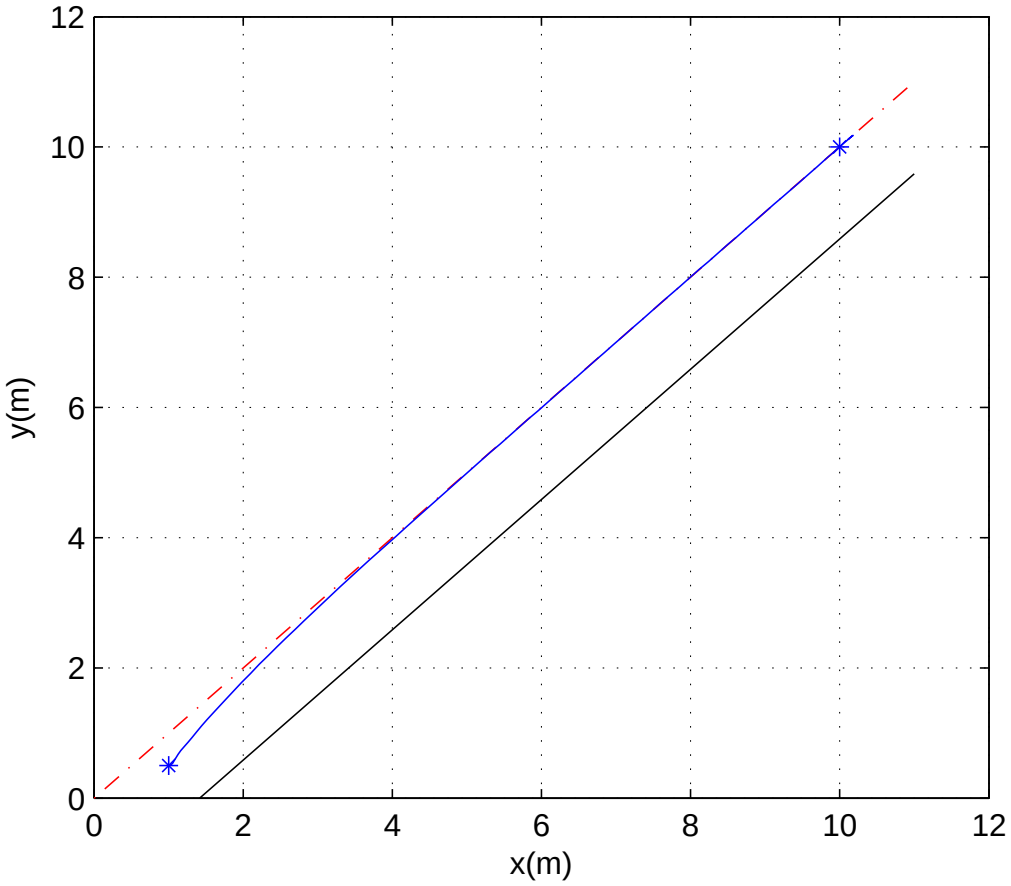

Fig. 3.5. WMR trajectory in the optimal solution scenario

The trajectory in Fig. 3.5 nears the optimal line asymptotic close and performs a smooth driving scenario.

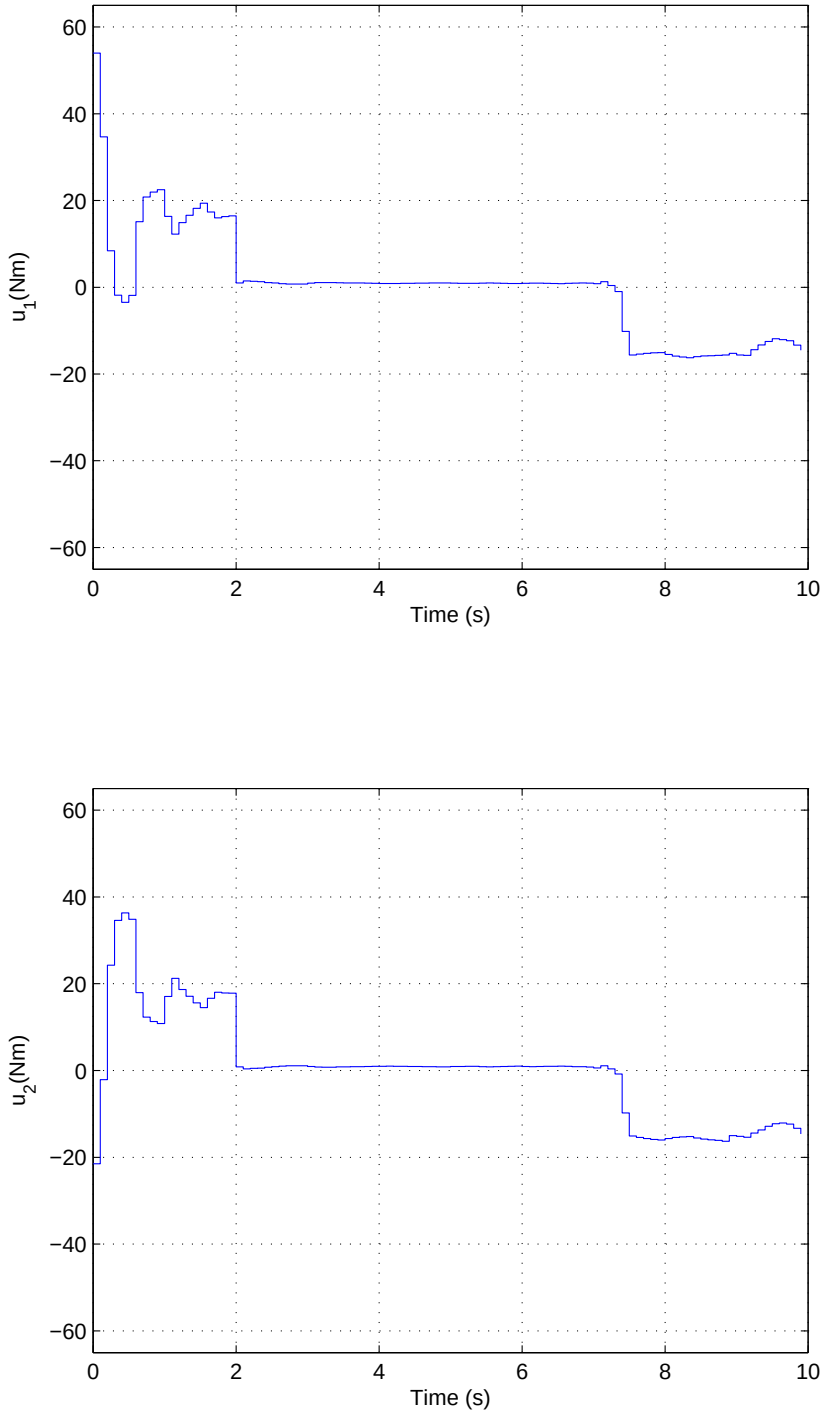

Fig. 3.6. WMR control inputs in the optimal solution scenario

In the diagram of the input torques, Fig. 3.6, it is easy to see that in the first 2 s high torques are used to push the WMR to its maximum allowable speed. Also differences between u_1 and u_2 are easy to see. This difference is because of the turning behavior to move the WMR to the reference distance d_{ref}. Between 2 s and 8 s a steady state behavior can be seen, because the WMR is driving towards the final goal with the same speed. After 8 s a lot of negative torques can be seen to decelerate the WMR as fast as possible to obtain a standstill directly on the final point. For this graph as well as for all other input torque graphs the projection method as introduced in equation (2.26) is used.

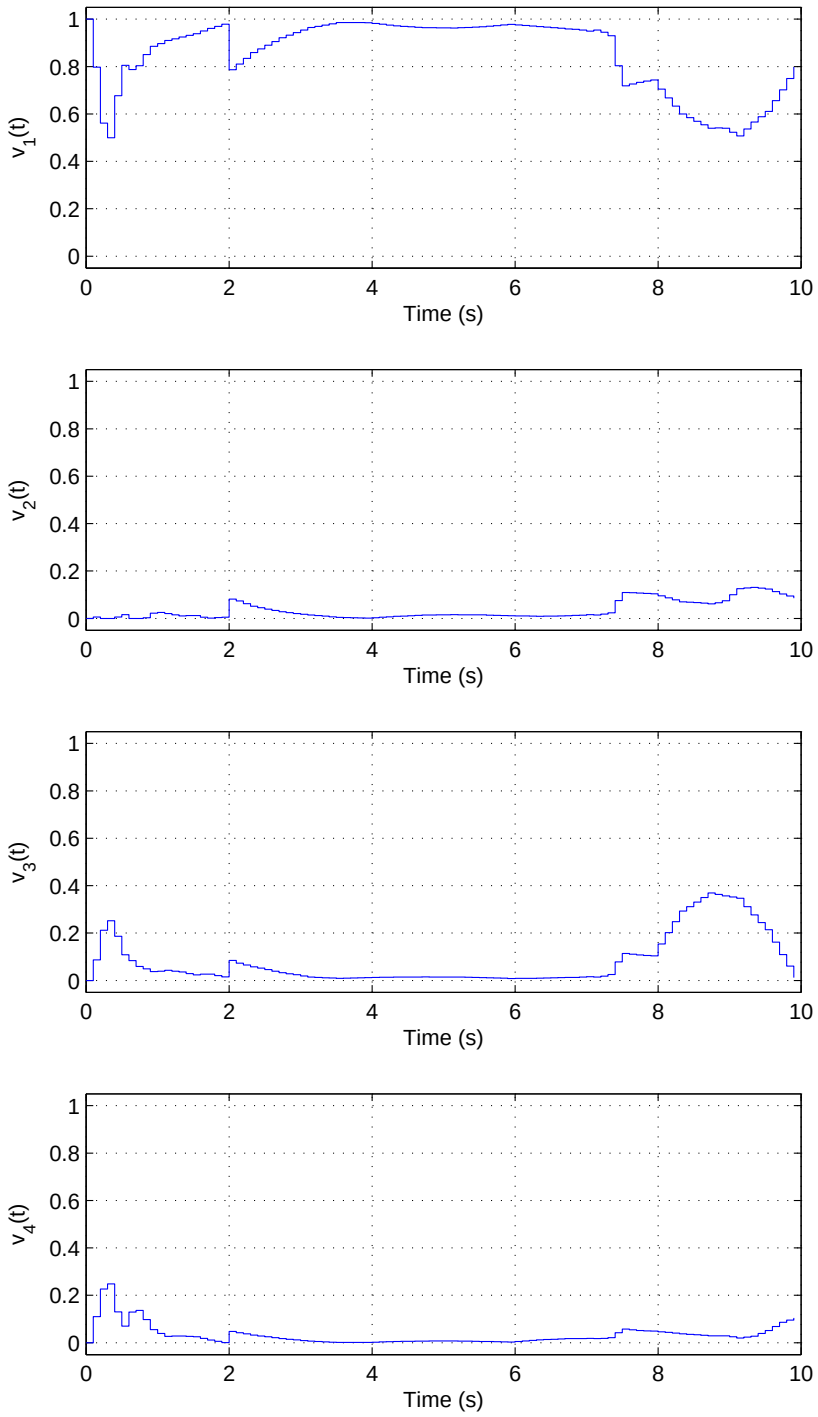

Fig. 3.7. WMR mode values in the optimal solution scenario

The modes as already introduced in Chapter 2 with equation (2.25) are used in Fig. 3.7. The modes values reflect the situations the WMR is in. Mode 1 is for the whole interval from 0 s to 8 s active, because the WMR accelerates and keeps the maximum speed all the time. Both wheels have to propel. In the process of acceleration the mode value of v_1 is equal to 1, because in this situation it is impossible that the WMR could be in one of the other modes and use regenerative breaking, which is not wanted in acceleration processes.

In the interval from 2 s to 8 s the mode value for v_1 is about 0.9. In this interval it is only needed to keep the maximum speed and not to accelerate. The mode value for v_1 is nevertheless high enough, which fits to the whole scenario properties. As already seen in Fig. 3.4 a high deceleration process with a partial negative forward velocity starts after 8 s. The mode value of v_1 sinks immediately down and the mode values of v_2, v_3 and v_4 rise up. The WMR has to use regenerative breaking to reduce the forward velocity and to keep close to the final point. This part is also consistent with the scenario properties.

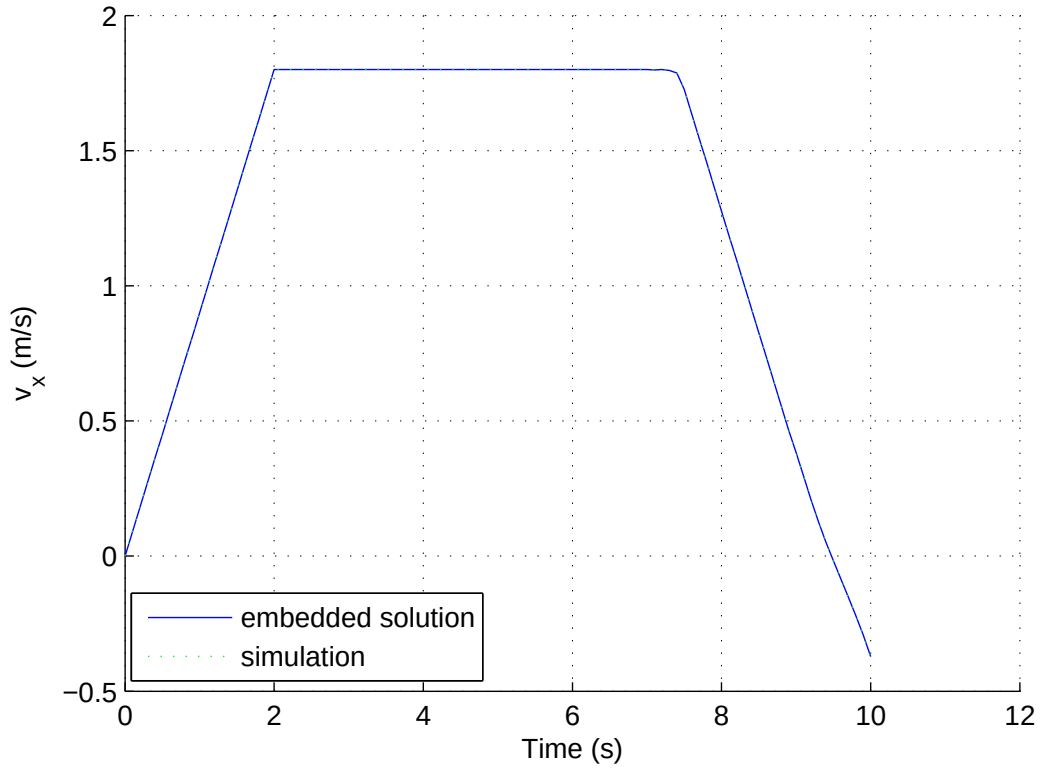

Fig. 3.8. Comparison between the forward velocity $v_x(t)$ of the WMR of a high fidelity simulation with the embedded solution of Fig. 3.4

In Fig. 3.9 and Fig. 3.8 the input torques and mode values of the embedded solution are used for the input of a high fidelity simulation. In Fig. 3.8 the high fidelity simulation, here called simulation, is again done by the ode solver 23 of MATLAB, which is a nonstiff differential equations solver. The velocities of the high fidelity simulation and the embedded solution are similar.

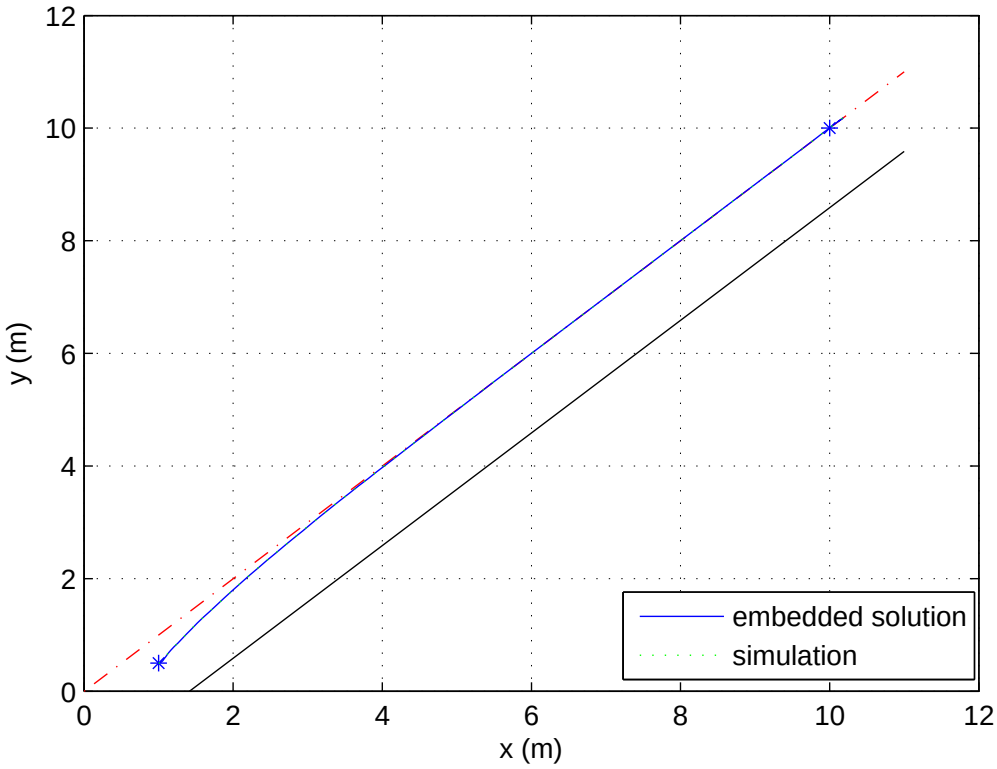

Fig. 3.9. Comparison between the trajectories of the WMR of a high fidelity simulation with the embedded solution

The trajectories in Fig. 3.9 are identical as well as the forward velocities $v_x(t)$ in Fig. 3.8. That means that a embedded solution with a interval length of $t_s = 0.1$ has a similar performance as the high fidelity simulation. It shows that the discrete low fidelity simulation of the optimization process is nearly identical to the high fidelity simulation in a 10 s simulation with 100 partitions ahead. This demonstrates the accurateness of the discrete low fidelity model and underlines the high quality of the further work with these tools in the next chapters.

3.4 Model predictive control

In this section model predictive control (MPC) is introduced and used on the presented wall following scenario with a final point as well as on the infinite wall following scenario.

3.4.1 Introduction of MPC

MPC is a optimization method with the possibility to look into the future behavior of a system with a finite and iterative prediction horizon. Every future partition obtains constant inputs u_1 and u_2, which can change every partition to fulfill the goals of a PI. The prediction horizon gives the possibility to plan ahead with the control input, but still the short term actions of reducing costs are steering the behavior of the model.

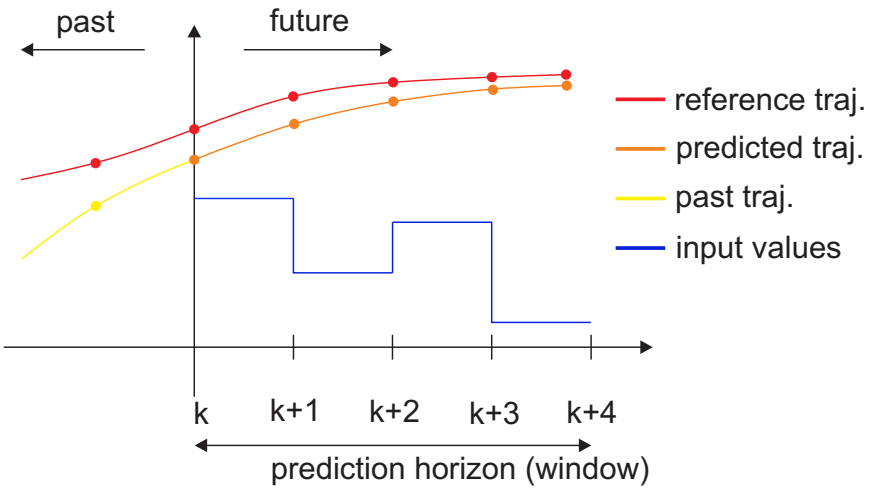

Fig. 3.10. Introduction of MPC theory

Fig. 3.10 gives an overview over the theoretical system of model predictive control. There we see a finite prediction horizon of four partitions and the chosen input values for the system. The past trajectory of the observed variable as shown, as well as the predicted trajectory for the future. The reference trajectory is the goal to reach. This is implemented with a penalty on the difference to the reference, the introduced errors.

Every dot represents a data packet, because the system is evaluated discrete every window size, which is here $t_s = 0.1$. The window size and the prediction horizon have an important influence on the dynamics of the system, because they are responsible for the range of the prediction horizon. More distance between each measurements provides more freedom to the system, but for real time application it should be reasonable small.

The MPC solution is the minimum energy solution that minimizes the errors of the actual system. Although only a limited knowledge about the future is known with this technique, the good performance achieved in simulations is incontestably. MPC receives feedback from the virtual environment every $t_s = 0.1$, this is why errors can never accumulate. This is why MPC is robust and achieves good simulation results in this and the following chapters. One major question in this thesis is the robustness of the model with MPC control strategy to Gaussian and Parkinsonian noise, which causes uncertainty in the optimization process.

3.4.2 MPC on wall following with a final point

The WMR has to drive again to a final point and keep a reference distance to the wall but using MPC. That means the overall performance of the driving task is not only to immediately reduce cost, which would maybe drive a WMR in a situation, where the future cost is very high. For the MPC a reference distance of 1 m to the wall with a penalty of $c_d = 1.5$ is chosen. The penalty on the final goal is $c_{xf} = 10$ and $c_\theta = c_v = 0$ again. The used partition length is $t_s = 0.1$ with a prediction horizon of 4 partitions.

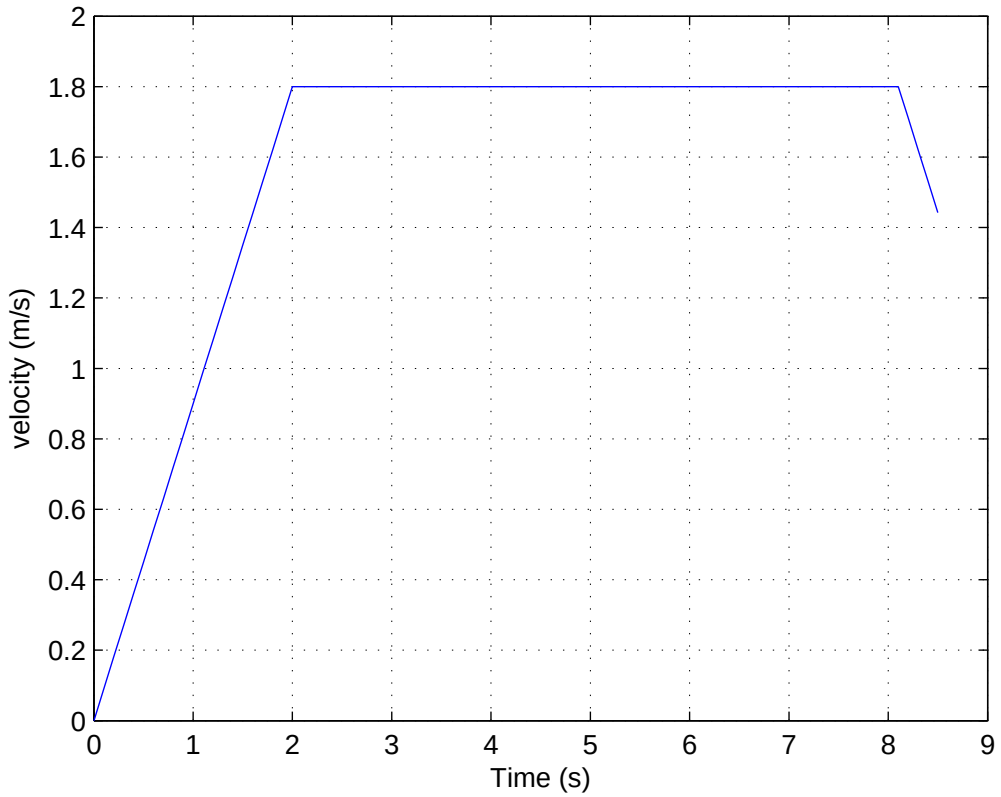

Fig. 3.11. WMR velocity of the wall following scenario with a final point

The velocity profile shows that for the turn movement the velocity increases to the maximum possible in the acceleration bounds. The maximum velocity of $1.8\frac{\mathrm{m}}{\mathrm{s}}$ is reached in minimum time of 2 s. The behavior of the optimal method and the MPC is equal in this point. Coming closer to the final point the WMR decelerates and reaches the final goal after 84 partitions.

The used partition length is again 0.1 s, so that the WMR arrives at the final goal after 8.4 s. The main difference between MPC and the optimal method is, that the last method has a fixed time to reach the final goal. That is why the WMR decelerates to zero. In the MPC solution a prediction horizon of 0.4 seconds is known that means that the WMR will only slow down a short period of time before the final goal.

It is travelling with 1.8 $\frac{\mathrm{m}}{\mathrm{s}}$ that means in 0.1 seconds a distance of 0.18 m is covered. Because of the size of the prediction horizon the WMR will slow down only in the last partitions of the whole scenario with maximum deceleration of $0.9\frac{\mathrm{m}}{\mathrm{s}^2}$ to achieve minimum cost.

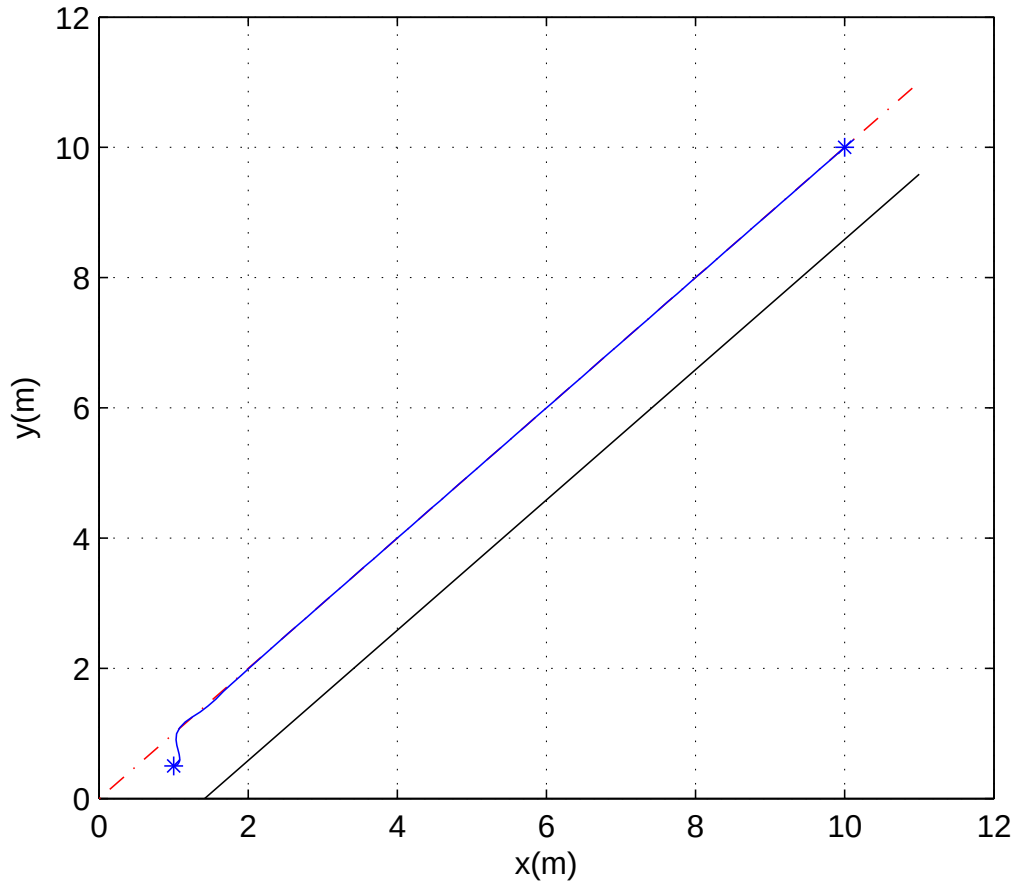

Fig. 3.12. WMR trajectory of the wall following scenario with a final point

The trajectory shows a turn to the line of the reference distance to the wall and then a consequent follow of the wall in the right distance just as expected. After 1 m of driving the WMR has already finished the full turn is on the reference line. MPC has a finite prediction horizon. This is why the trajectory is not similar to the result of the full interval solution in Fig. 3.5 and there are differences in the process of getting close to the optimal line. The MPC solution has a smaller radius to perform the turn as the optimal solution. The maximum acceleration is used in the turn movements of the MPC solution as well as in the optimal solving method.

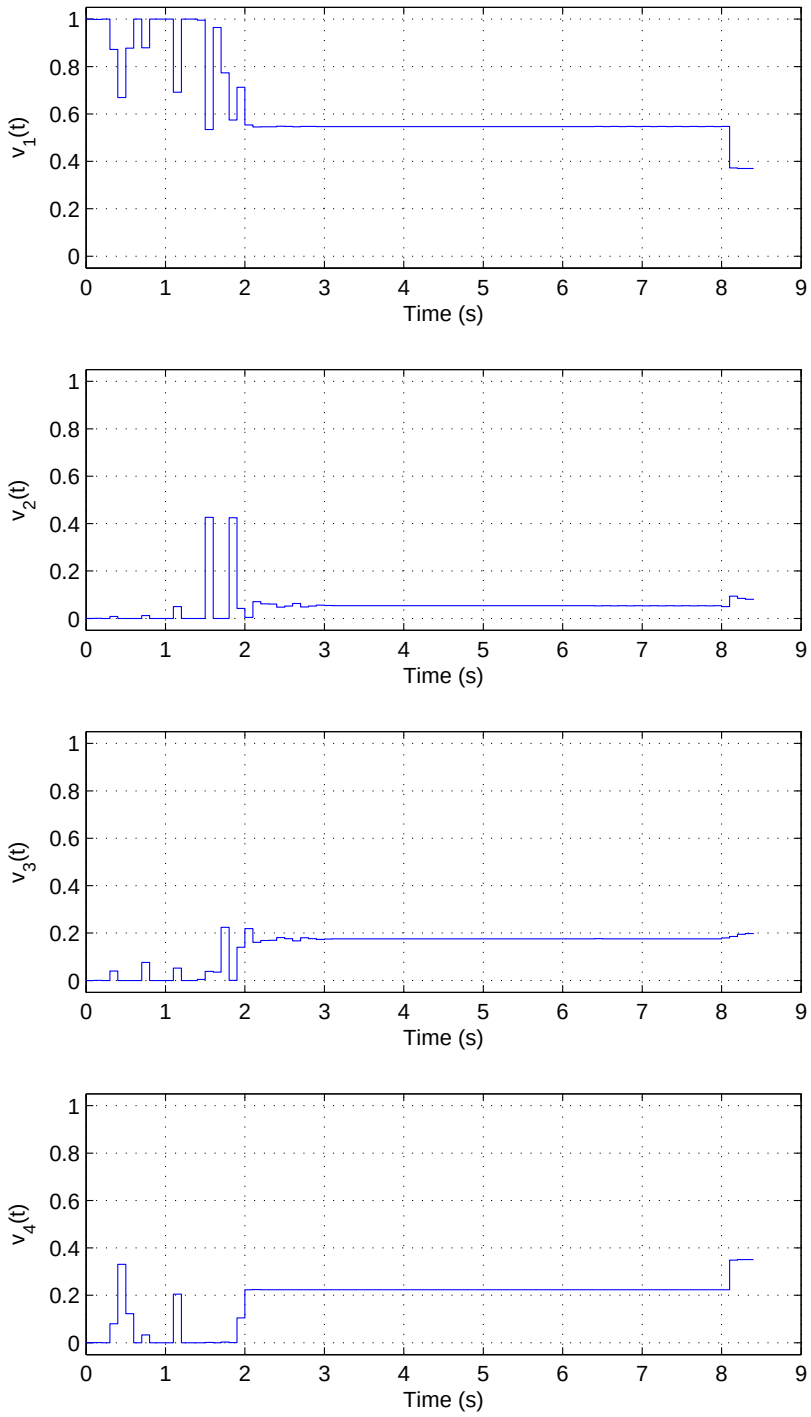

Fig. 3.13. WMR mode switches of the wall following scenario with a final point

Similar to the solution with optimal knowledge, mode 1 is dominant in the first part of the scenario from 0 s to 3 s with high mode values. In the constant velocity phase, mode 1 is still dominant with mode values of about 0.44. After 8 s the mode value of mode 1 sinks, because the final goal is nearly reached and maximum deceleration is used. The mode values of mode 4 for regenerative braking on both wheels are significant higher than mode 1 values. That means that for every braking in the MPC the regenerative braking is used to charge the battery.

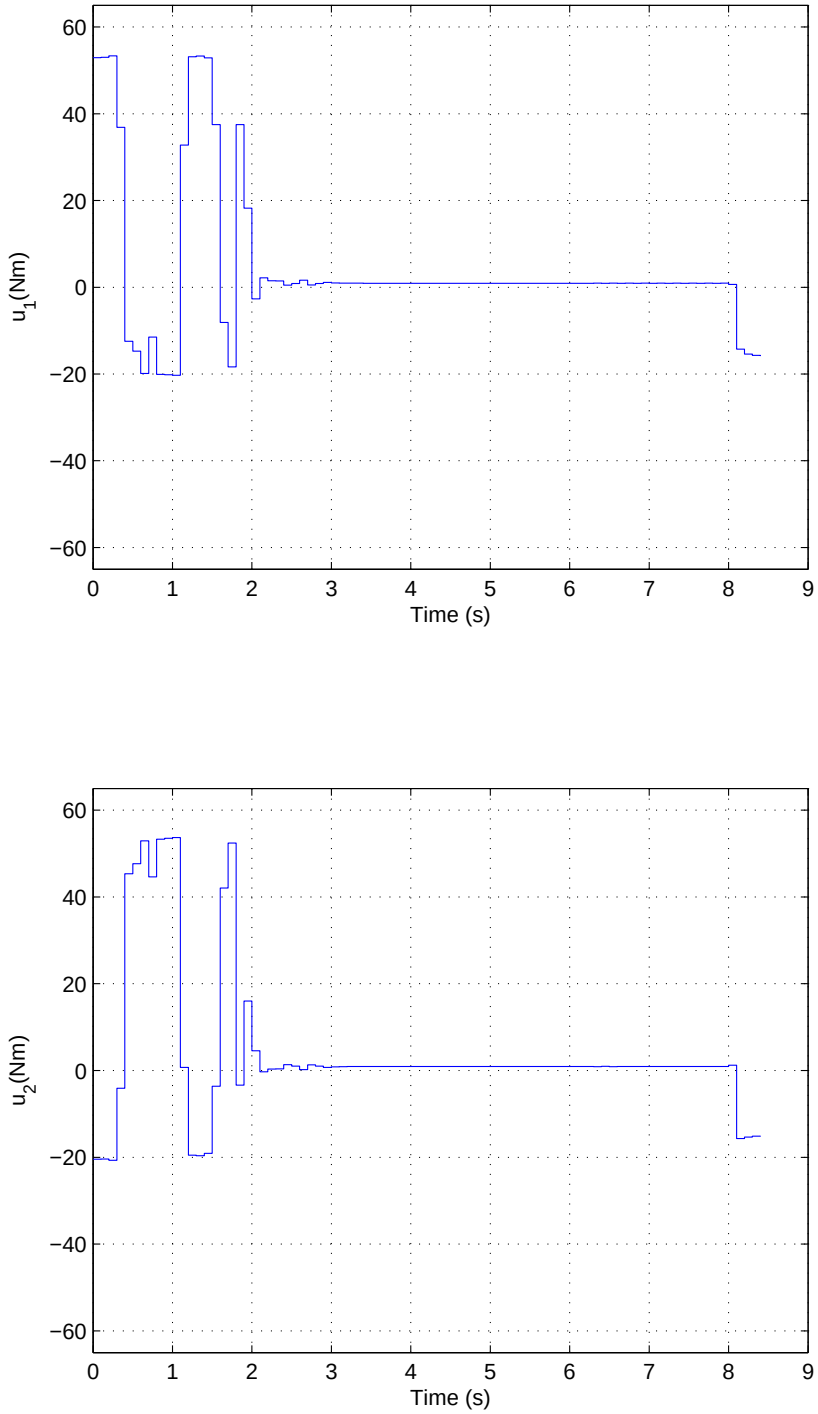

Fig. 3.14. WMR control inputs of the wall following scenario with a final point

In Fig. 3.14 the differences of both input torques u_1 and u_2 are easy to see when the WMR processes a turn movement and when it brakes with the regenerative brake. In turn movements and deceleration the input torques differ, but in the movement with constant velocity and constant moving direction between 3 seconds and 8 seconds both input torques are constant and nearly on the same level. The regenerative braking is used in the last partitions to force a slowdown of the WMR to the final goal. The cost of the scenario has the following value:

Table 3.1
Comparison of the total costs of the optimal solution and MPC

optimal	MPC
J = 34.243	J = 34.948

The table shows only a 2% cost increase of the MPC method, which fits to other comparism of optimal methods and MPC methods in research.

3.4.3 MPC on wall following with a final point and velocity profile

In this section the WMR has to drive to a final point and to keep a reference distance to the wall using MPC. The only difference to the last scenario is an additional velocity profile as introduced in Fig. 3.2. For this scenario we maintain a reference distance of 1 m to the wall but with a penalty of $c_d = 1.5$. The penalty on the final goal is $c_{xf} = 10$. The penalty on the velocity profile $c_v = 20$. The partition length is $t_s = 0.1$ with a prediction horizon of 4 partitions.

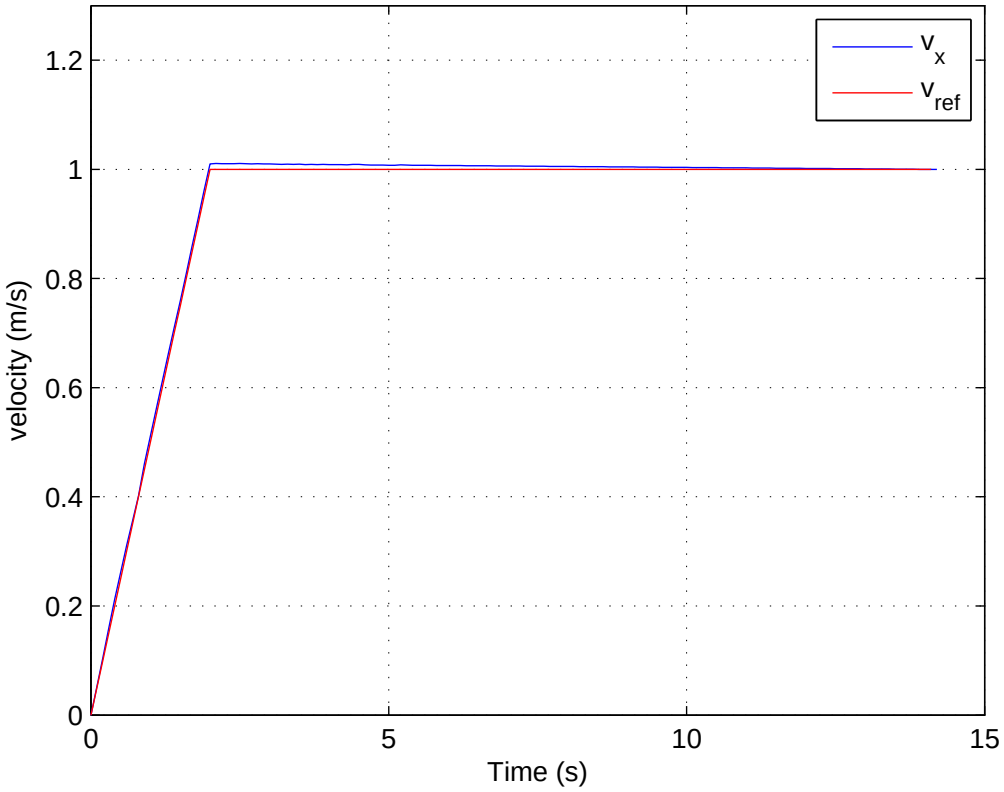

Fig. 3.15. WMR velocity of the wall following scenario with a final point and a velocity profile

According to the velocity profile of Fig. 3.3 the WMR is restricted to a maximum forward driving velocity of $1\frac{\mathrm{m}}{\mathrm{s}}$. The forward velocity sticks to the profile and only small deviations, when the maximum reference velocity is reached, can be seen. The acceleration and deceleration have a maximum value of $0.5\frac{\mathrm{m}}{\mathrm{s}^2}$ because of safety issues. With these restrictions it is possible for a human to drive a WMR safely.

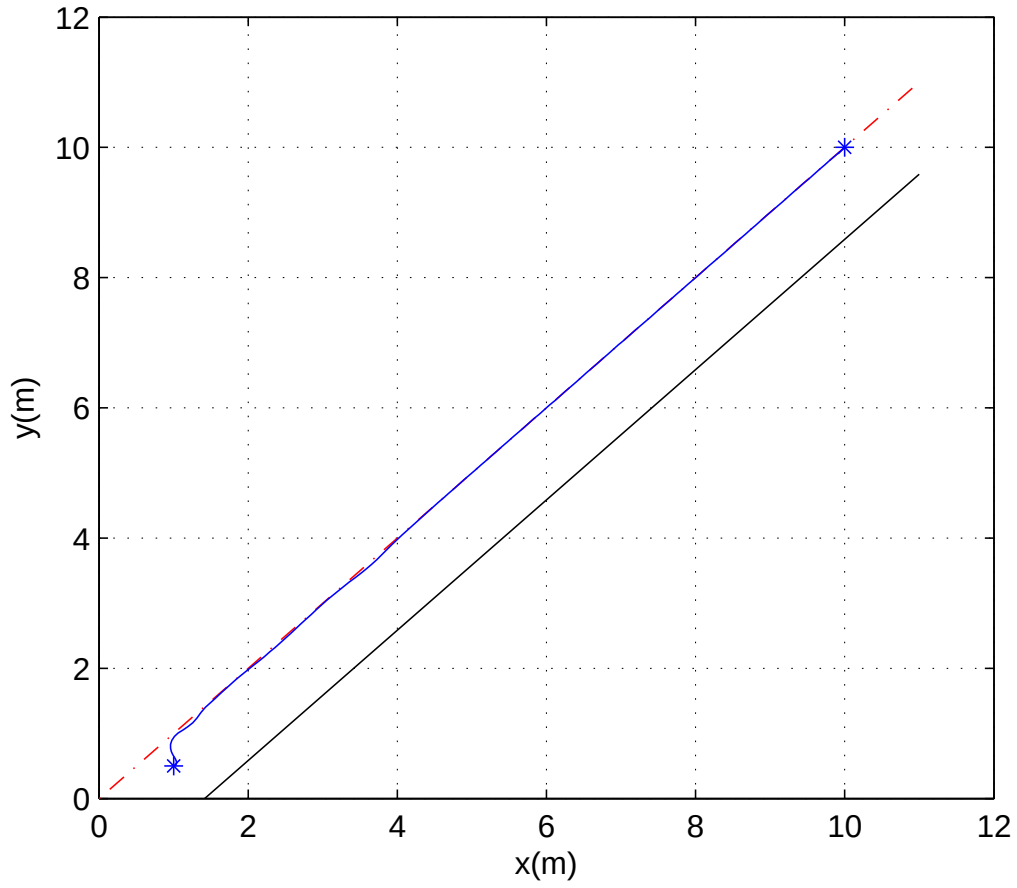

Fig. 3.16. WMR trajectory of the wall following scenario with a final point and a velocity profile

The trajectory looks similar to the trajectory without a velocity profile. A small difference are near the starting point. Here the WMR is restricted to the velocity profile with a maximum of $1\frac{\mathrm{m}}{\mathrm{s}}$, which means that it can never reach the maximum possible velocity of $v_{x,max} = 1.8\frac{\mathrm{m}}{\mathrm{s}}$ that the unrestricted method can achieve.

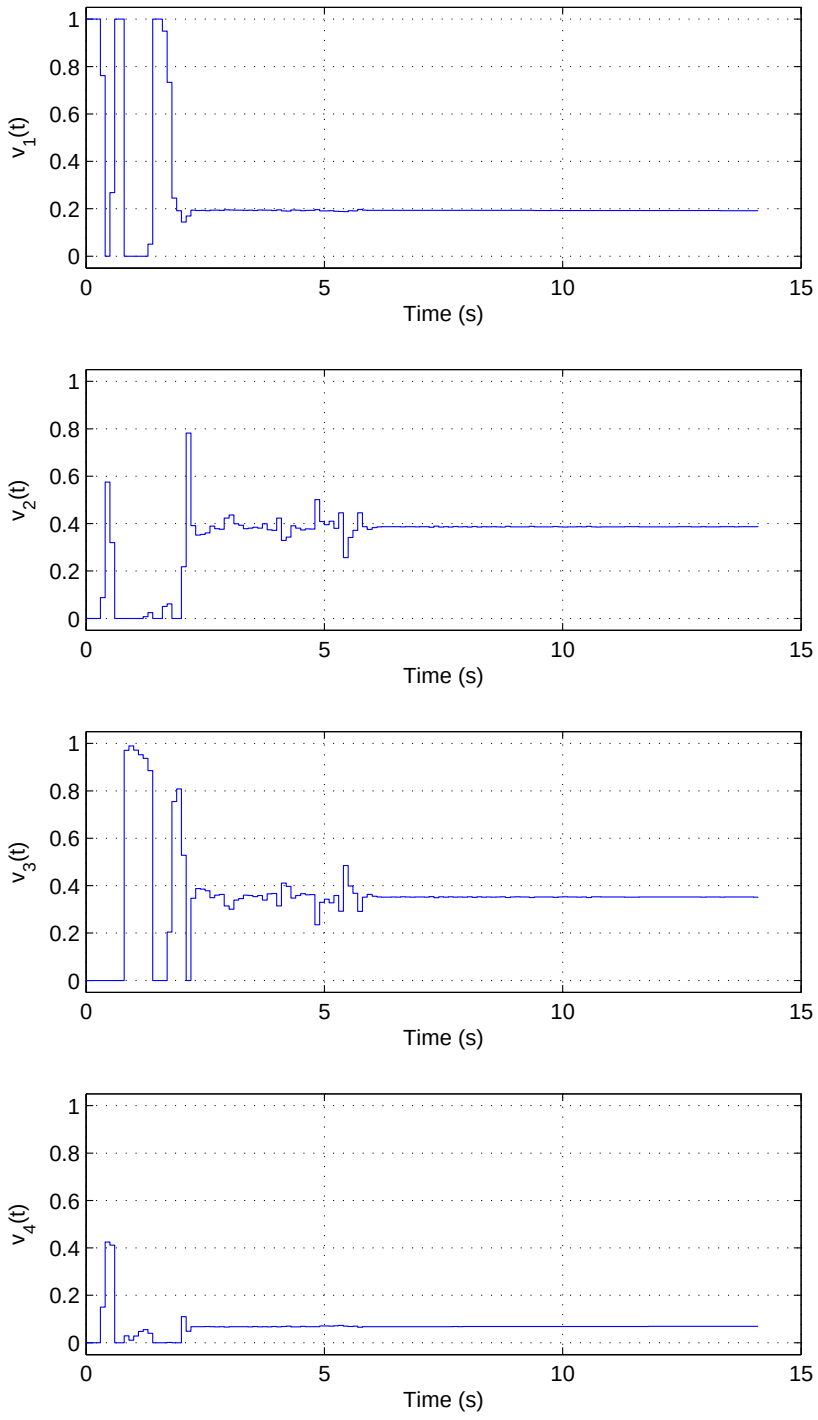

Fig. 3.17. WMR mode switches of the wall following scenario with a final point and a velocity profile

Similar to the optimal solution, mode 1 is dominant in the turning movement from 0 s to 2 s with mode values of $v_1(t)$ nearly 1 everywhere. In the constant velocity phase, $v_1(t)$ is still dominant with mode values of about 0.8. After 13 s the mode value of mode 1 sinks to about 0.6, because the final goal is nearly reached and regenerative braking is needed to slow the vehicle down with the given deceleration rate. Differences to the MPC solution without a velocity profile can be seen. because of the still dominant value of mode 1 in this scenario. Through the constant deceleration regenerative braking is only partially needed.

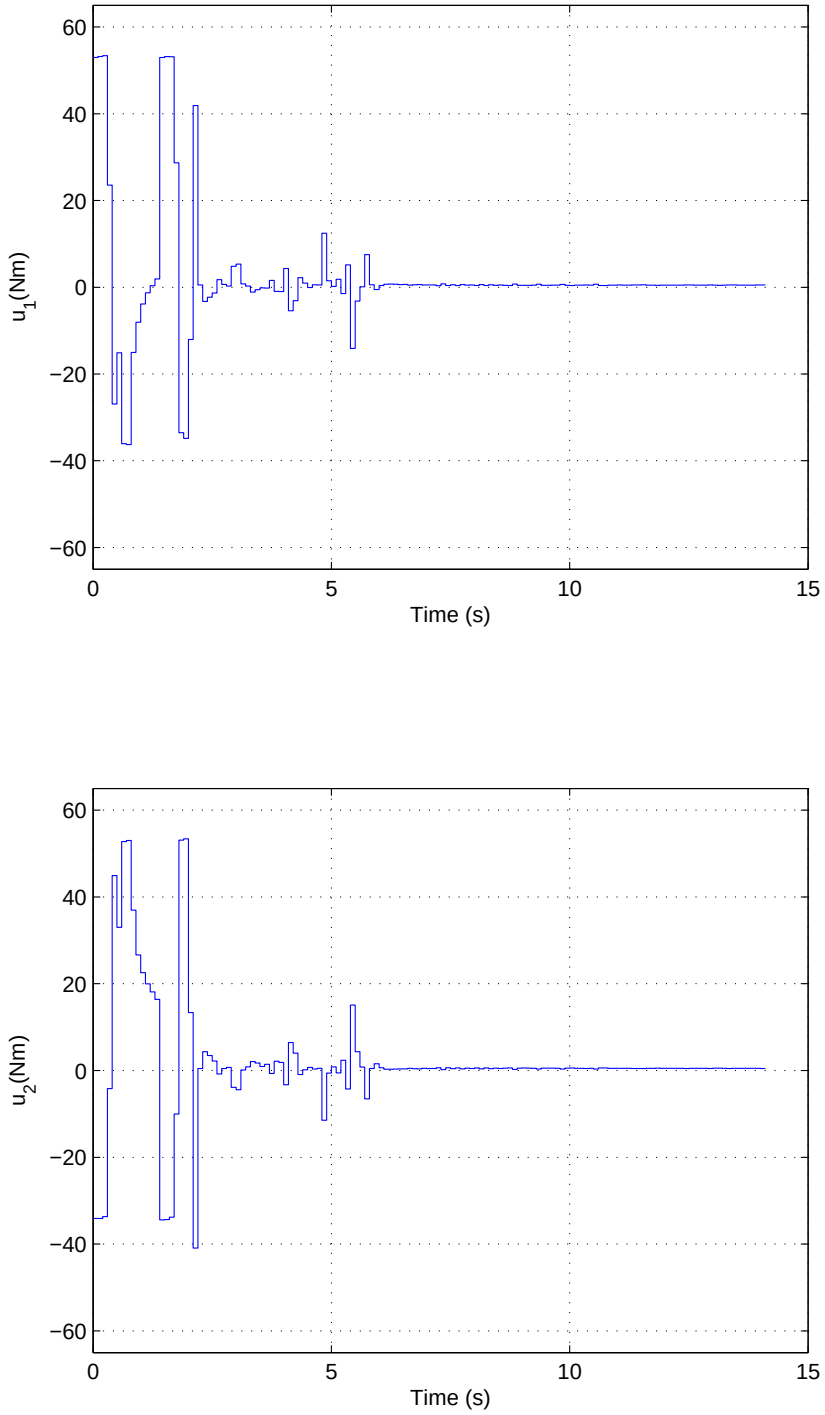

Fig. 3.18. WMR control inputs of the wall following scenario with a final point and a velocity profile

In Fig. 3.18 the difference in the both input torques u_1 and u_2 are easy to see when the WMR processes a turn movement. In turn movements and deceleration the input torques differ, but in the movement with constant velocity and constant moving direction between 2 s and 13 s both input torques are on the same level. The cost of this MPC solution with velocity profile has the following value:

Table 3.2
Comparison of the total costs of the optimal solution, MPC, MPC with velocity profile and infinite MPC with given cost coefficients of the PI

	optimal solution	MPC	MPC with velocity profile
J	34.243	34.948	54.905
c_{xf}	10	10	10
c_d	1.5	1.5	1.5
c_v	0	0	20
c_θ	0	0	0

3.4.4 MPC on infinite wall following

The WMR has to drive at a reference angle, keep a reference distance to the wall and should follow a velocity profile . The velocity is exactly designed for the infinite wall following scenario as possible to see in Fig. 3.19. For the MPC a reference distance of 1m to the wall with a penalty of $c_d = 10$ is chosen. The penalty on the final goal is $c_{xf} = 0$, but a final point is taken as a stopping criterion for the simulation. The penalty on the velocity profile $c_v = 5$. The reference angle term used a penalty constant of $c_v = 1$. The used partition length is $t_s = 0.1$ with a prediction horizon of 4 partitions.

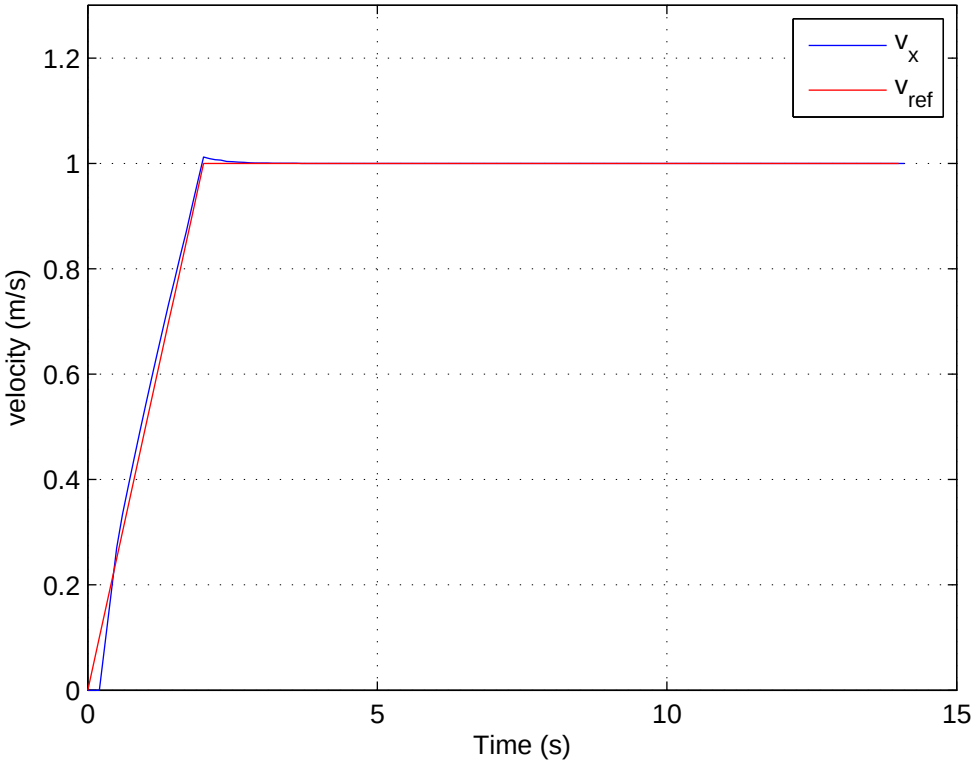

Fig. 3.19. WMR velocity of the infinite wall following scenario with a velocity profile

In the graph of the forward velocity v_x in Fig. 3.19 the velocity trajectory follows the reference velocity. In the acceleration phase in the beginning are small deviations, which are due to the more complex turning movement towards a parallel movement to the reference wall. In the acceleration process the velocity is a small amount higher, because the approximation of the optimal angle and penalty on the distance to the wall is forcing the WMR further. After the acceleration process no deviations are present.

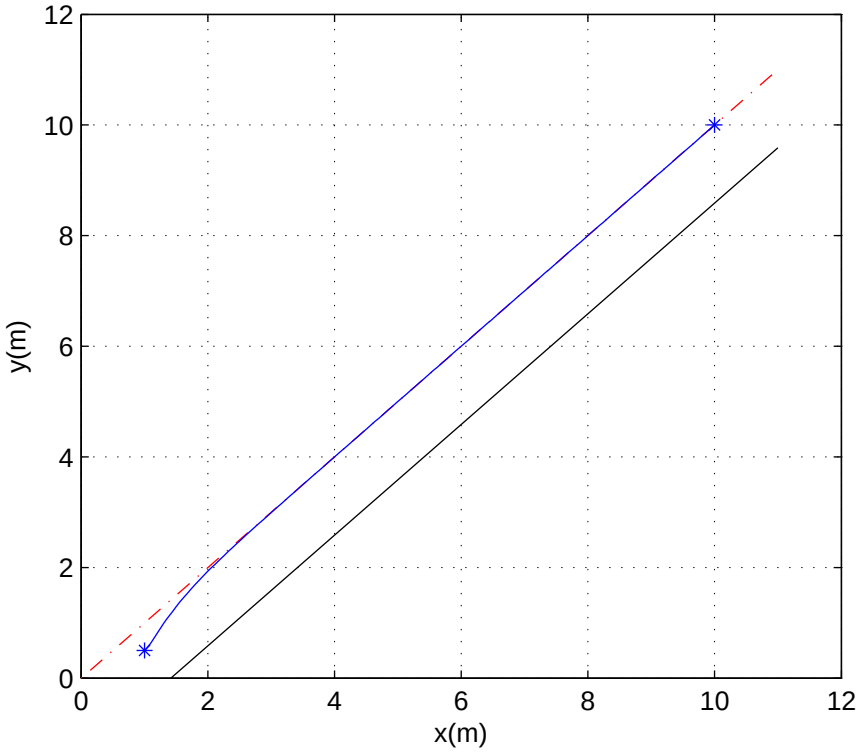

Fig. 3.20. WMR trajectory of the infinite wall following scenario with a velocity profile

In Fig. 3.20 the trajectory of the WMR in the coordinate system is shown. The turning radius is as small as in the optimal solution and both trajectories are similar. A smooth approximation of the optimal line is possible to see and a lot of similarities to the optimal solution can be seen.

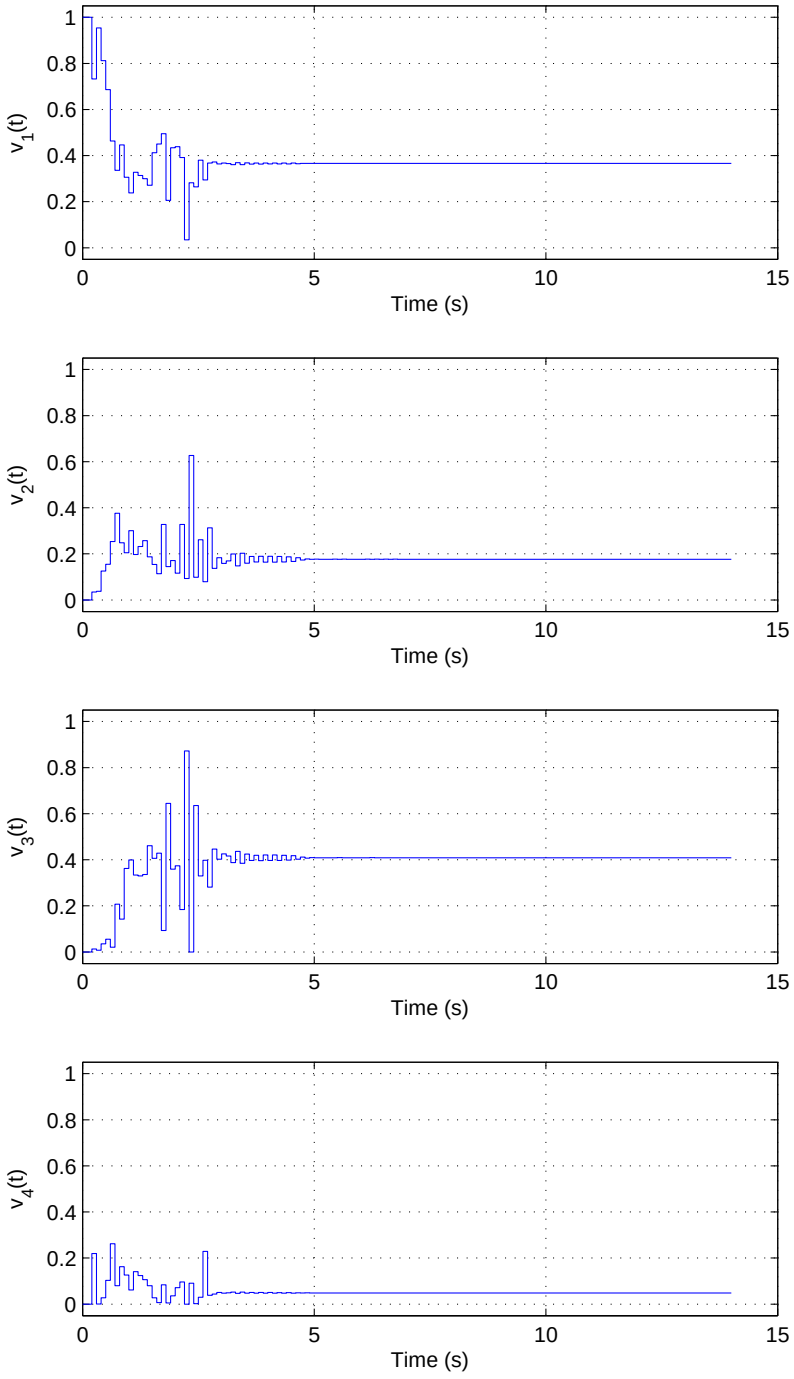

Fig. 3.21. WMR mode switches of the infinite wall following scenario with a velocity profile

Mode 1 is dominant in the turning movement until 3 s. After this all mode values are constant which fits to the trajectory and velocity profile.

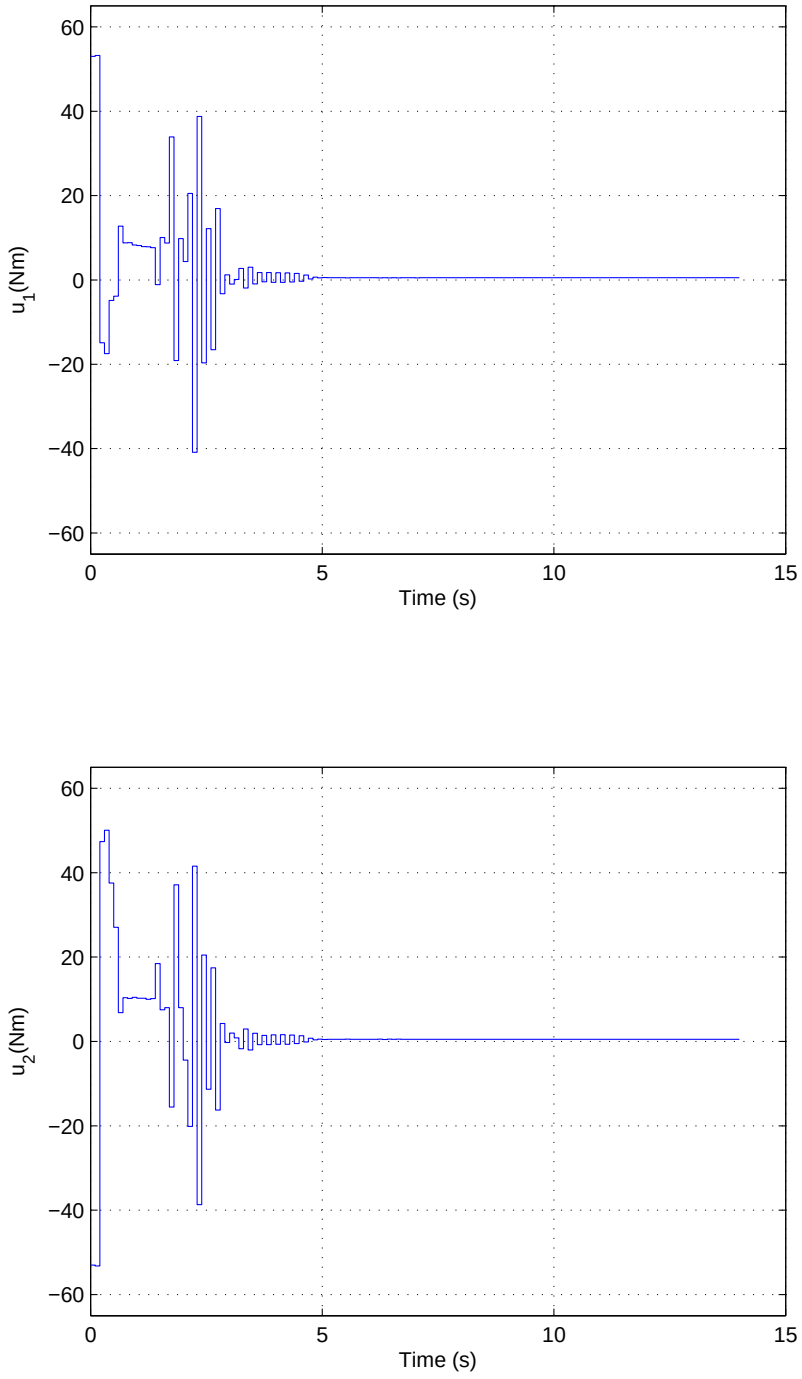

Fig. 3.22. WMR control inputs of the infinite wall following scenario with a velocity profile

Typical for the turning movement, in Fig. 3.22, the input torque values differ a lot. After the constant driving phase is reached both torques are constant on about 2 Nm. Only energy is used to compensate the energy losses through drag.

Table 3.3
Comparison of the total costs of the optimal solution, MPC, MPC with velocity profile and infinite MPC with given cost coefficients of the PI

	optimal solution	MPC	MPC with velocity profile	infinite MPC
J	34.243	34.948	54.905	2.1033
c_{xf}	10	10	10	0
c_d	1.5	1.5	1.5	10
c_v	0	0	20	5
c_θ	0	0	0	1

3.5 Appendix: Derivation of the distance to the wall formula

In every situation and angle the distance to the wall it is the most important fact for the control algorithms. Therefore a formula got developed, which derivation can be reproduced by the following graph:

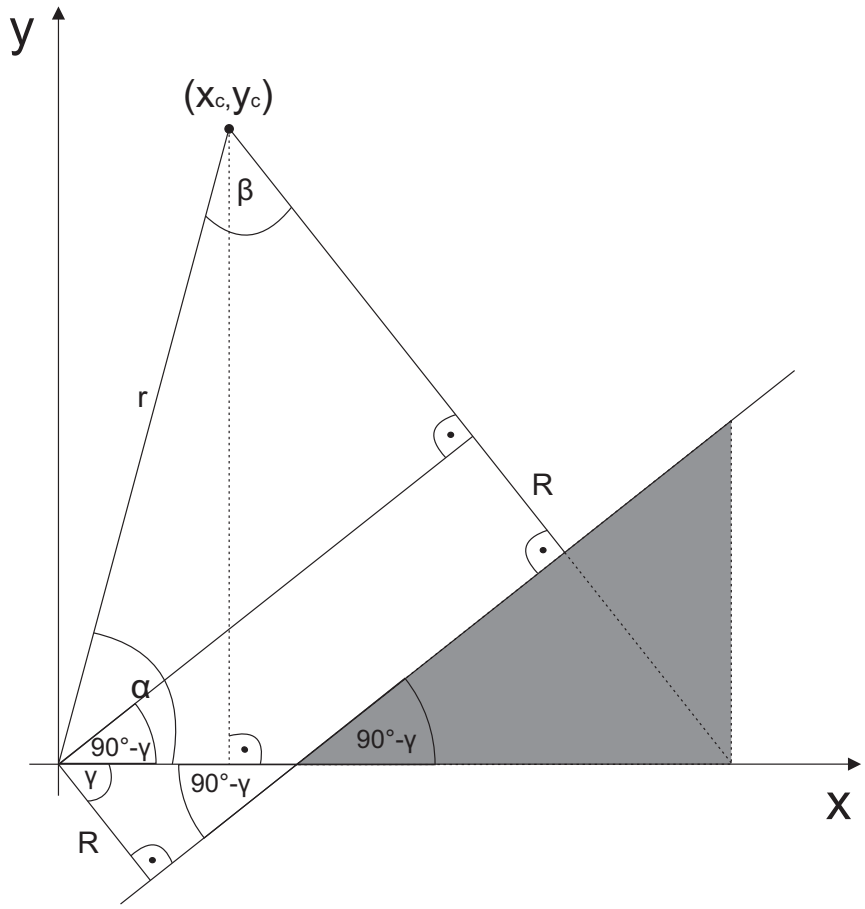

Fig. 3.23. Derivation of minimum distance formula

Again the center of rotation (x_c, y_c) of the electric wheelchair is used as the reference point for the distances and the wall is shaded in gray for clarity reasons. The constant R denotes the shifting distance from the wall to the origin. The angle α is arctan $\left(\frac{y_c}{x_c}\right)$. The distance $d_{center}\,(x_c, y_c, \gamma)$ is the minimum distance from the center of rotation of the wheelchair to the wall. The angle γ sets the orientation of the wall in the cartesian coordinate system. The angle β for the computation of the minimum distance to the wall follows out of the trapezoid angle relations:

$$\alpha = \arctan\left(\frac{y1_c}{x_c}\right) \tag{3.24}$$

$$\beta = 360° - 90° - 90° - \gamma - \arctan\left(\frac{y_c}{x_c}\right) = 180° - \gamma - \arctan\left(\frac{y_c}{x_c}\right) \tag{3.25}$$

With triangle angle relations it follows the equation for the minimum distance to the wall:

$$d(x_c, y_c, \gamma) = \cos(\beta) \cdot \sqrt{x_c^2 + y_c^2} + R \tag{3.26}$$

4. THE CORNERING SCENARIO AND COMBINED SCENARIOS WITH AND WITHOUT GAUSSIAN NOISE

This chapter provides an overview of the cornering scenario. As a next step a combined scenario with two wall following parts and one cornering part are introduced and simulated. As the final result of this chapter the combined scenario is simulated with random Gaussian white noise on the distance to the wall measurements, which mimics the behavior of sonar sensor measurements in a real scenario.

4.1 The cornering scenario

In this section the corning scenario is introduced and the derived PI is shown. Simulation results are presented, evaluated and classified.

4.1.1 Introduction of the cornering scenario

In this scenario we consider a polar coordinate system as a basis for the distance to the corner calculation and convert our cartesian information into polar coordinates. The objective in this scenario is that the WMR performs a turn with constant velocity and a constant radius to the corner.

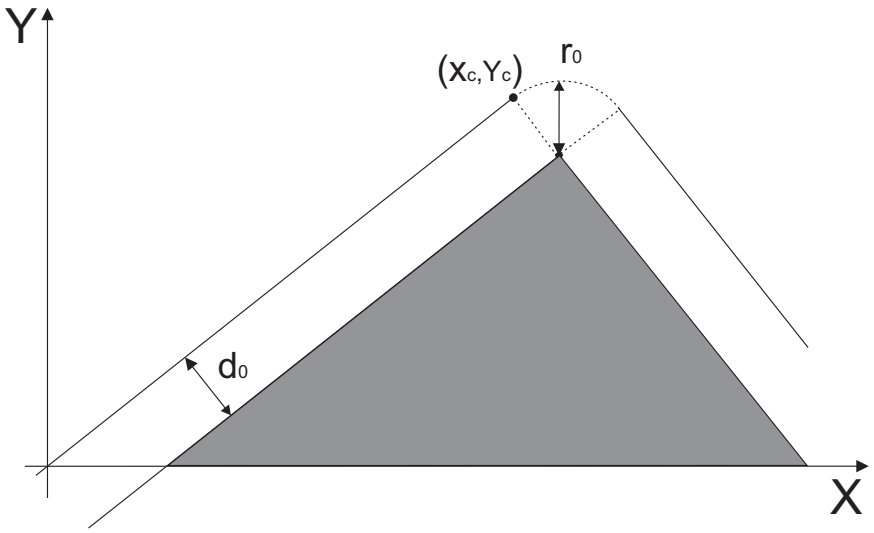

Fig. 4.1. Overview of the cornering scenario

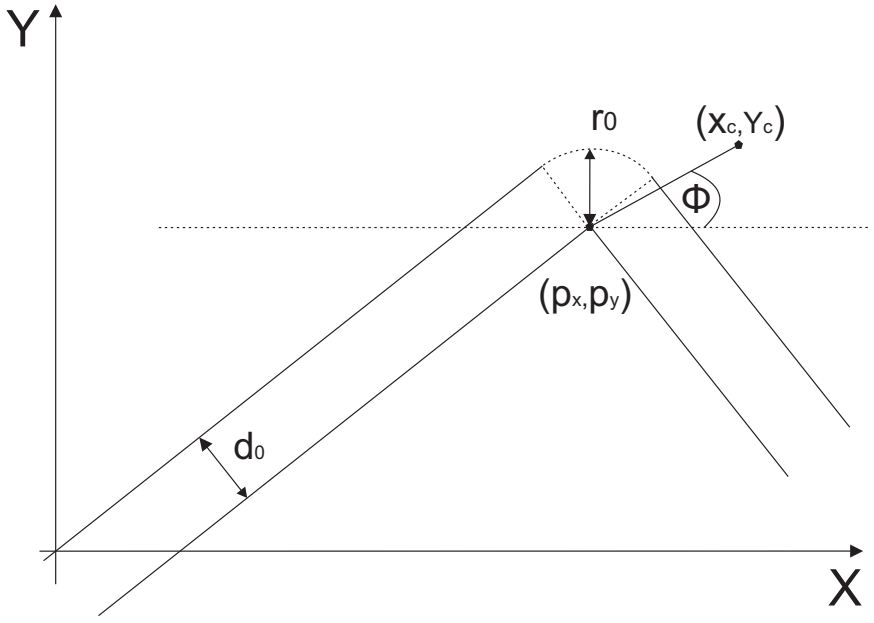

Fig. 4.2. Angle relations of the cornering scenario

At the start of the cornering scenario, the center of rotation (x_c, y_c) of the wheelchair has the distance $d_0 = r_0$ to the shown shaded wall as seen in Fig 4.1. This distance is

also the distance we want to retain during the turn. The needed velocities are generated by constant input torques u_1 and u_2. These are given on the electric wheelchair in each time interval via the already introduced projection in equation (2.26). A starting velocity of $v_x = 0.5\ \frac{\mathrm{m}}{\mathrm{s}}$ is used in this scenario, because the WMR should reach the turn at this velocity. In the calculations it is important to consider the corner point (p_x, p_y) as the origin of the new polar coordinate system. The angle ϕ and the distance r to the corner point in Fig. 4.2 are determined by the following formulas:

$$d(t) = \sqrt{(x_c(t) - p_x(t))^2 + (y_c(t) - p_y(t))^2} \tag{4.1}$$

$$\phi = \arctan\left(\frac{y_c - p_y}{x_c - p_x}\right) \tag{4.2}$$

With this transformation it is easy to maintain a constant radius $r = d_{ref}$ and a constant turning velocity $\dot{\phi} = \omega$. The radius is just the 2-norm of the distance between the corner point and the center of rotation of the WMR. For the actual implementation a constant turning velocity is realized with a time dependent change of the reference angle θ of the WMR. A time dependent system is more realistic and θ is a state in the model, which makes it easy to control. In addition the turning velocity ω has to be constant, which is also a state in the WMR model.

$$\theta_{ref}(t) = \frac{\pi}{4} - \frac{1}{2}t \tag{4.3}$$

Here t represents the time elapsed after the cornering scenario starts. A similar approach with the same effect would specify a constant rotational velocity:

$$\omega_{ref}(t) = \dot{\theta}_{ref}(t) = -\frac{1}{2} \tag{4.4}$$

4.1.2 Heuristic Development of the Performance Index

Different to the wall following scenario a penalty for not reaching the final point is absent. As already specified the PI errors in the distance to the corner point:

$$c_d \left(\frac{d_{ref} - d(t)}{d_{ref}}\right)^2 \tag{4.5}$$

This penalty enforces a constant radius of $r = d_{ref} = 1$ m around the corner point. Again we assume that $d(t)$ is known through equation 4.1.

The next part of the PI is a penalty on deviations from the time dependent angle $\theta(t)$ from $\theta_{ref}(t)$ presented in equation 4.3.

$$c_\theta \left(\theta_{ref}(t) - \theta(t)\right)^2 \tag{4.6}$$

The error in the velocity profile from a constant velocity of $v_{ref} = 0.5 \ \frac{\text{m}}{\text{s}}$ is another part of the PI:

$$c_v \left(\frac{v_{ref} - v_x(t)}{v_{ref}}\right)^2 \tag{4.7}$$

The last part of the PI is a term that penalizes the use of input torque related to the mode value for the embedded solution. By mildly penalizing energy this usage promotes regenerative braking. Only the input torques in the propelling mode are chosen here, because regenerative braking absorbs kinetic energy.

$$c_e \left[v_1(t) \left(u_{m11}(t)^2 + u_{m21}(t)^2\right) + v_2(t) \left(u_{m22}(t)^2\right) + v_3(t) \left(u_{m13}(t)^2\right)\right] \tag{4.8}$$

The input torques are related to the wheel $i \ \epsilon \ \{1,2\}$ and mode $j \ \epsilon \ \{1,2,3,4\}$:

$$u_{mij}(t) = 2u_{ij}(t) - 1 \tag{4.9}$$

The input torques are not directly penalized. Rather the modulation, $u_{mij}(t)$, with values between -1 and 1, are penalized.
The full PI then has the following form:

$$J_{Corner} = \int_0^T \Bigg[c_d \left(\frac{d_{ref} - d(t)}{d_{ref}}\right)^2 + c_\theta \left(\theta_{ref}(t) - \theta(t)\right)^2 \\ c_v \left(\frac{v_{ref} - v_x(t)}{v_{ref}}\right)^2 + c_e \left[v_1(t) \left(u_{11}(t)^2 + u_{21}(t)^2\right) + v_2(t) \left(u_{22}(t)^2\right) + v_3(t) \left(u_{13}(t)^2\right)\right] \Bigg] dt \tag{4.10}$$

4.1.3 Simulation of the cornering scenario

A MPC control strategy with a four partition window is used. The size of each windows is $t_s = 0.1$ s and the size of the prediction horizon is 0.4 s. The introduced PI of equation (4.10) is used for MPC. Fig. 4.3 shows a corner turn with a distance to the corner point, angle, velocity and energy penalty on the behavior of the WMR. The cost coefficients were chosen to achieve good overall performance. The results are achieved with the chosen parameters $c_d = 1.5$, $c_\theta = 10$, $c_v = 10$ and $c_e = 0.01$. The energy coefficient $c_e = 0.01$ supports regenerative braking in deceleration situations immense. If this weight coefficient is chosen to be higher, then the WMR would not move, because every use of energy and therefore every propelling is penalized.

A high emphasis with a weight of 10 on velocity and angle reference is important in the cornering scenario. A powered wheelchair user wants a constant turning velocity and constant forward velocity. The distance to the corner weight coefficient is in the ratio $6.\overline{6} : 1$ smaller. That means that small deviations from the reference should not be corrected in a immense way, because this would affect the velocity references negatively. In simulation this ratio was considered to be good for an overall good performance.

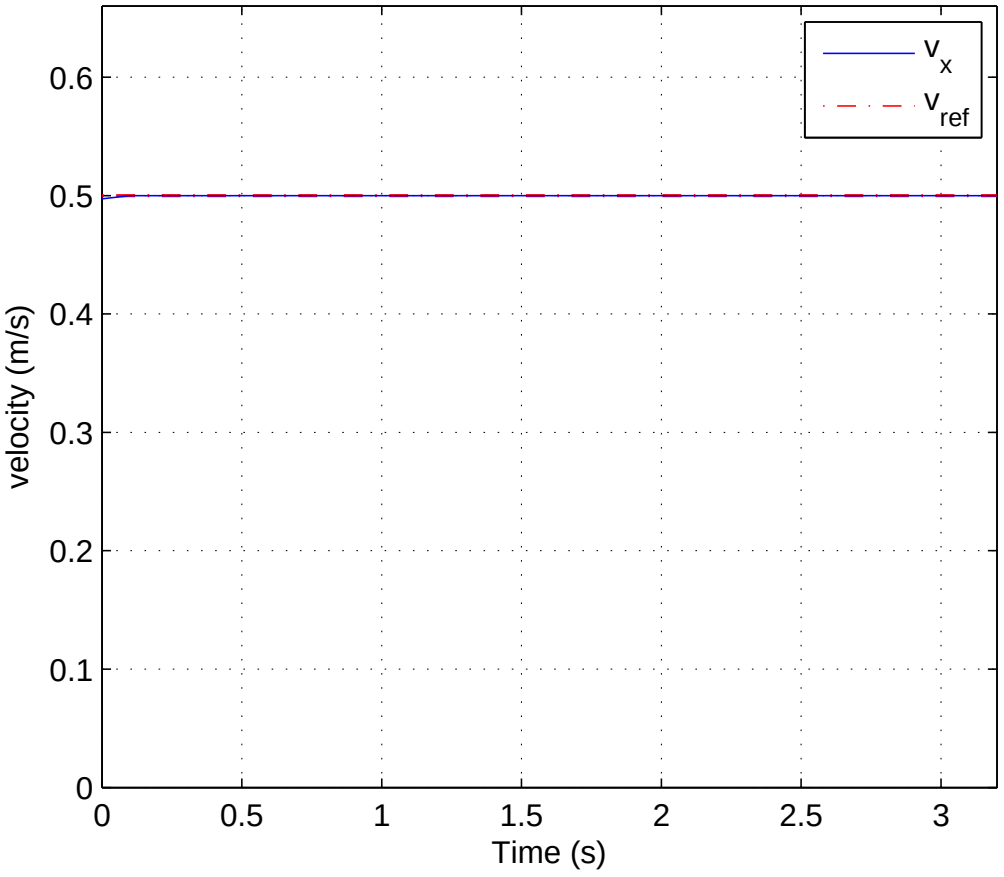

Fig. 4.3. WMR velocity of the wall following scenario with a final point

Because of the already mention starting velocity $v_x = 0.5\ \frac{\mathrm{m}}{\mathrm{s}}$ and the constant reference velocity $v_{ref} = 0.5\ \frac{\mathrm{m}}{\mathrm{s}}$, an overall constant velocity as shown in Fig.4.3 minimizes the velocity error.

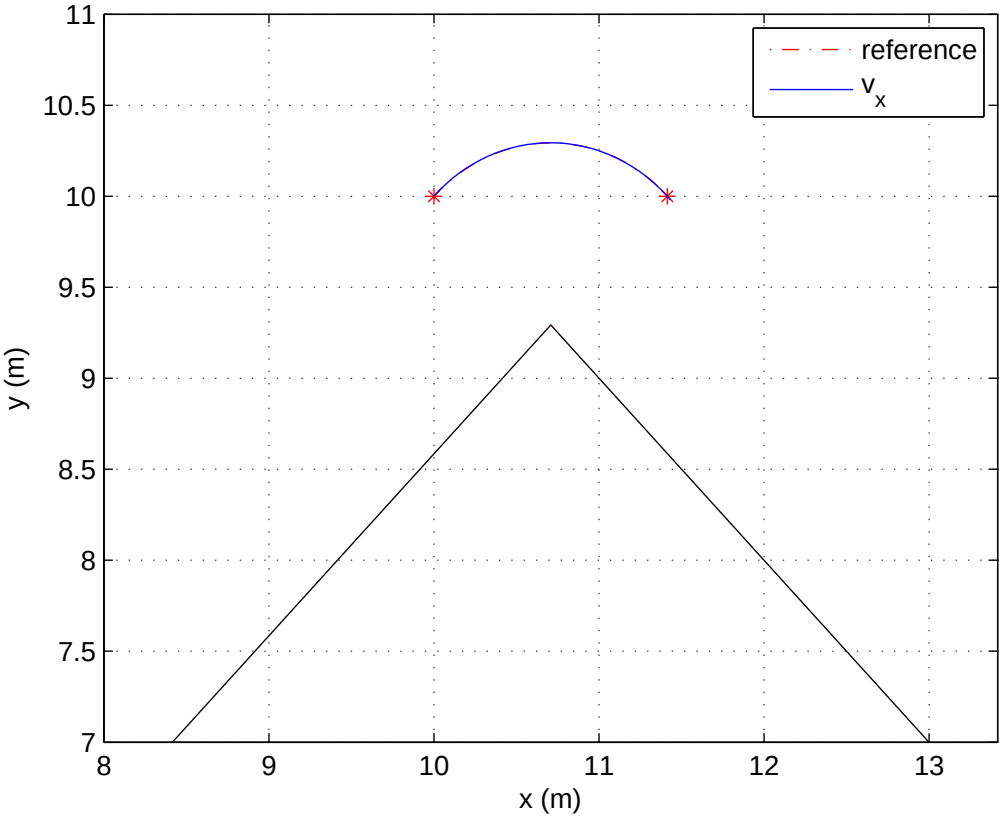

Fig. 4.4. WMR trajectory of the wall following scenario with a final point

From Fig. 4.4, we observe that the trajectory is very close to the reference trajectory and performs a nearly perfect quarter circle.

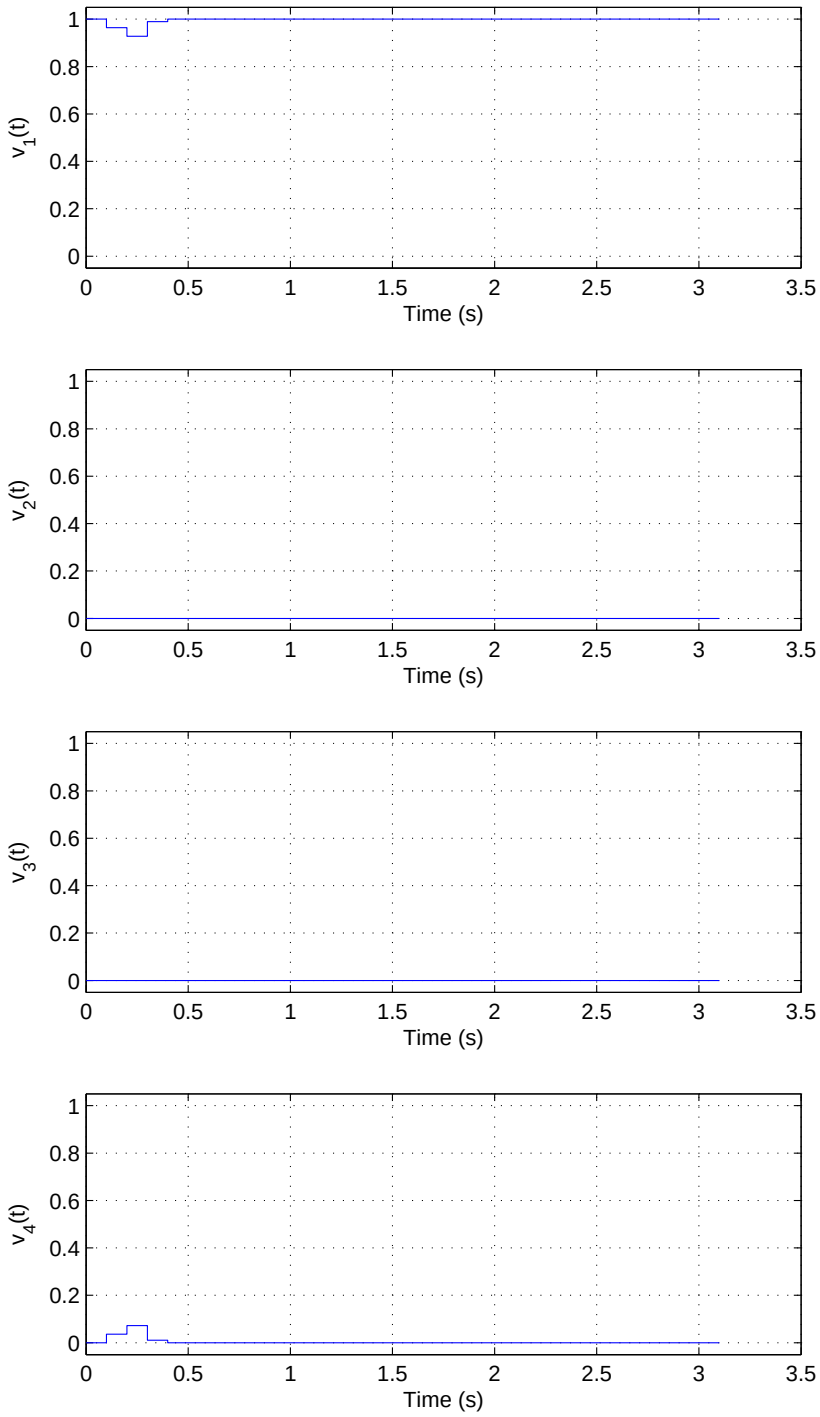

Fig. 4.5. WMR mode switches of the wall following scenario with a final point

Because of an existing small transient effect in the beginning of the turn, the mode value of v_1 is not 1 in the second partition in Fig. 4.5. Elsewhere the mode value is 1, because no regenerative braking is needed in a task, where a turn with a constant velocity should be managed. Modes 2, 3 and 4 contain regenerative braking components, that means that mode 1 is the only option for the chosen scenario with an overall impact on the system of nearly 100% everywhere.

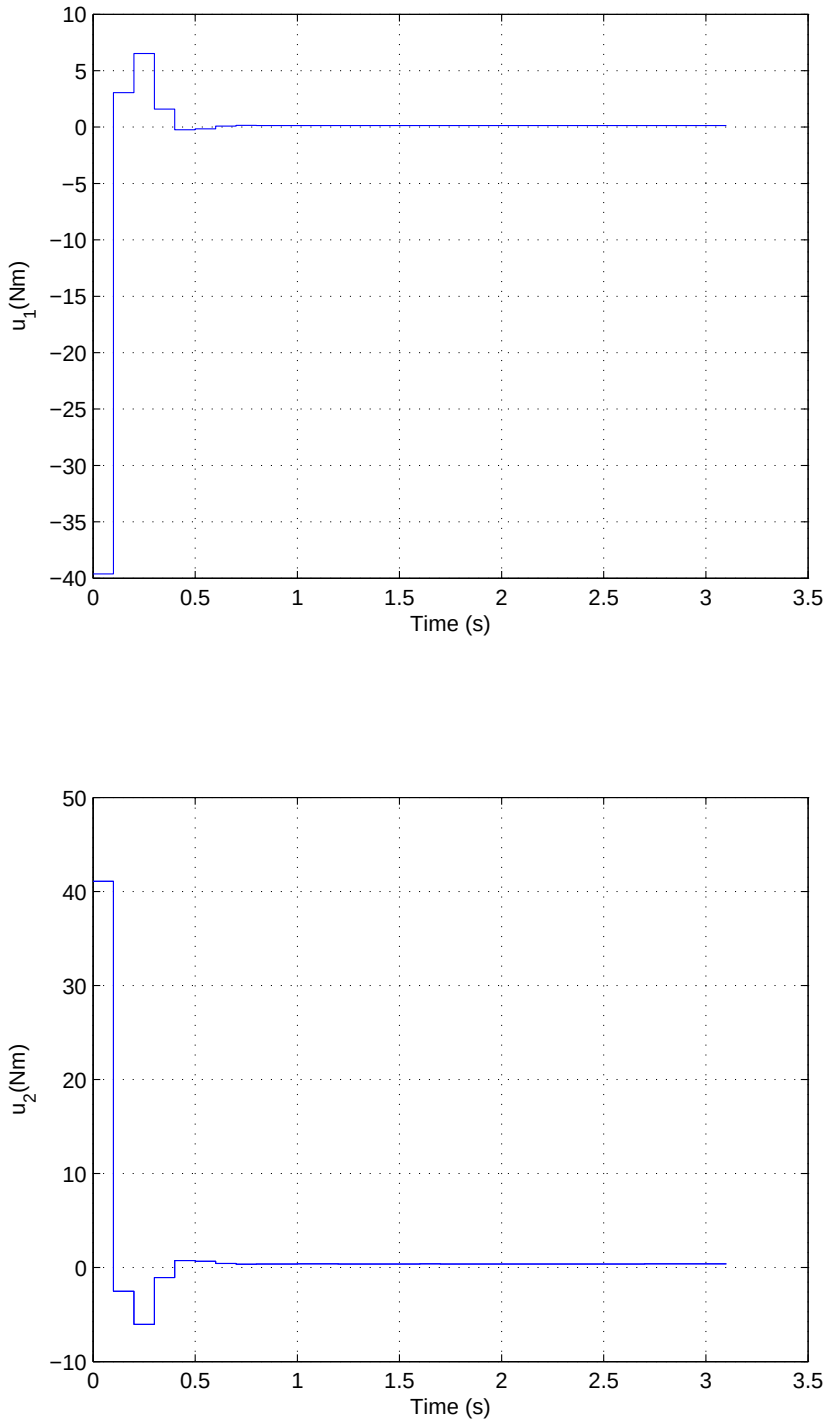

Fig. 4.6. WMR control inputs of the wall following scenario with a final point

In Fig. 4.6 the mentioned transient effect is easy to recognize in the first 0.5 s, due to the torque fluctuations. After the model is stable in the turning scenario the ground reaction force is still reducing the speed of the WMR. Constant positive torques, depending on the rotational velocity of each wheel, need to be applied to the wheels for the rest of the scenario.

4.2 Sonar sensors for distance to the wall measurements

The use of sensors in a real scenario is necessary to achieve a wanted distance to the wall and proper orientation in the coordinate system. The WMR sensors need to detect and locate corners to force a change between the different possible performance metrics. In this example the sonar sensors have a cone of more than 30° and are mounted with 30° angle different on top of the WMR as in Fig 4.7. As usual v_x points in the forward direction of the WMR and all sensors are mounted on the center of rotation $\overline{x}(t) = [x_c(t), y_c(t)]^T$ of the WMR. The distances d_1 and d_2 are the measured distances to the wall of sonar sensor 1 and 2.

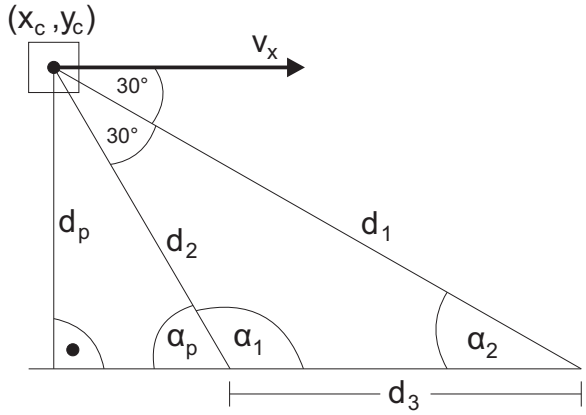

Fig. 4.7. Distance to the wall measurements through sonar sensors

With the law of cosines in Fig. 4.7, d_3 can be calculated as:

$$d_3 = \sqrt{d_1^2 + d_2^2 + 2d_1 d_2 \cos(30°)} \tag{4.11}$$

Using the law of sines:

$$\alpha_1 = \sin\left(\frac{d_2 \sin(30°)}{d_3}\right)^{-1} \tag{4.12}$$

In Fig. 4.7, it is easy to see that $\alpha_p = 180° - \alpha_1$. That means that the perpendicular and minimum distance to the wall can be calculated in every situation with measurements of two sonar sensors and from the equation:

$$d_p = d_2 \sin(\pi - \alpha_1) \tag{4.13}$$

In a real sensor scenario, one would expect a 5% Gaussian error on the measurements of d_1 and d_2. Technically one would then compute the combined influence on the actual measurements:

$$d_p = \frac{d_{p1} + d_{p2}}{2} \tag{4.14}$$

However for the simulations it was convenient without any loss of generality to simply set the measured distance to the wall according to:

$$d(t) = d_{exact}(t) + 0.05\mathcal{N}\left(\mu, \sigma^2\right) \tag{4.15}$$

The mean $\mu = 0$, $\sigma^2 = (0.5)^2$ and $\mathcal{N}(\mu, \sigma^2)$ denotes a Gaussian distribution.

4.3 The combined scenario

This scenario is a combination of the wall following scenario and the cornering scenario. Again a four parition MPC control strategy with a prediction horizon of 0.4 s is used to solve the control problem. For the two wall following scenarios the following PI constants are used: The distance to the wall penalty is $c_d = 1.5$, the penalty on the final point of the wall following task is $c_{xf} = 10$. An additional velocity penalty of $c_v = 10$ secures the safety of the driving maneuver with a velocity profile. In the cornering scenario the distance to the wall penalty has the same value $c_d = 1.5$. The error in angle θ penalty is $c_\theta = 10$. The velocity has to be controlled due to the time dependent angle references. The user should receive the minimum amount of centripetal force and though the velocity should be constant with a used weight coefficient of $c_v = 10$. A energy cost coefficient of $c_e = 0.01$ support again regenerative braking.

Table 4.1
Weight coefficients in the wall following and corning part of the combined scenario

	c_{xf}	c_d	c_v	c_e	c_θ
wall following	10	1.5	10	0.01	0
cornering	0	1.5	10	0.01	10

From now on plots of combined scenarios with several PI parts will be divided in the plot with dashed black lines. The first part is the first wall following part. Between the dashed lines the cornering part is executed. After the second and last black dashed line the second wall following part is simulated.

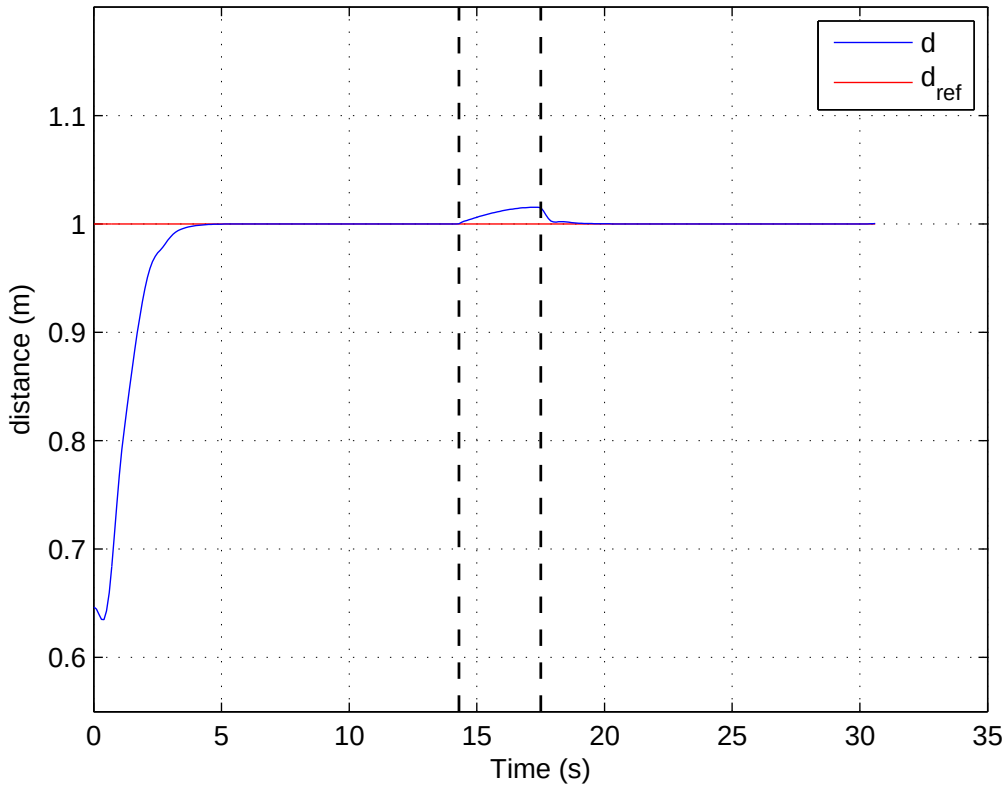

Fig. 4.8. WMR distance to the wall of the combined scenario

The distance to the wall of the WMR in Fig. 4.8 directly comes close to the references d_{ref}. In the cornering part a accumulated error can be seen, which is corrected in the beginning of the second wall following simulation. The system used is based on a partition length of $t_s = 0.1$ s. That means it is possible to change the PI every 0.1 s. In chapter 4 a time based angle profile is used, which assumes the starting point of the cornering part at $(10, 10)$. Because of the way the model is designed the cornering start at a point slightly over the ideal value, because it has to recognize first, that the cornering part is reached.

Additional the weight factor of the angle profile is about the factor 7 higher than the distance to the corner point weight factor, which would correct the accumulation.

This is why we have a small constant accumulated error of the distance to the corner point in the cornering part. This effect occurs in every simulation with an angle profile in the PI.

In chapter 6 the scenario is simulated without the time based angle profile with significant good results, which shows that both approaches are possible. In chapter 4 and chapter 5 the angle profile provides safety to the cornering part of the scenario.

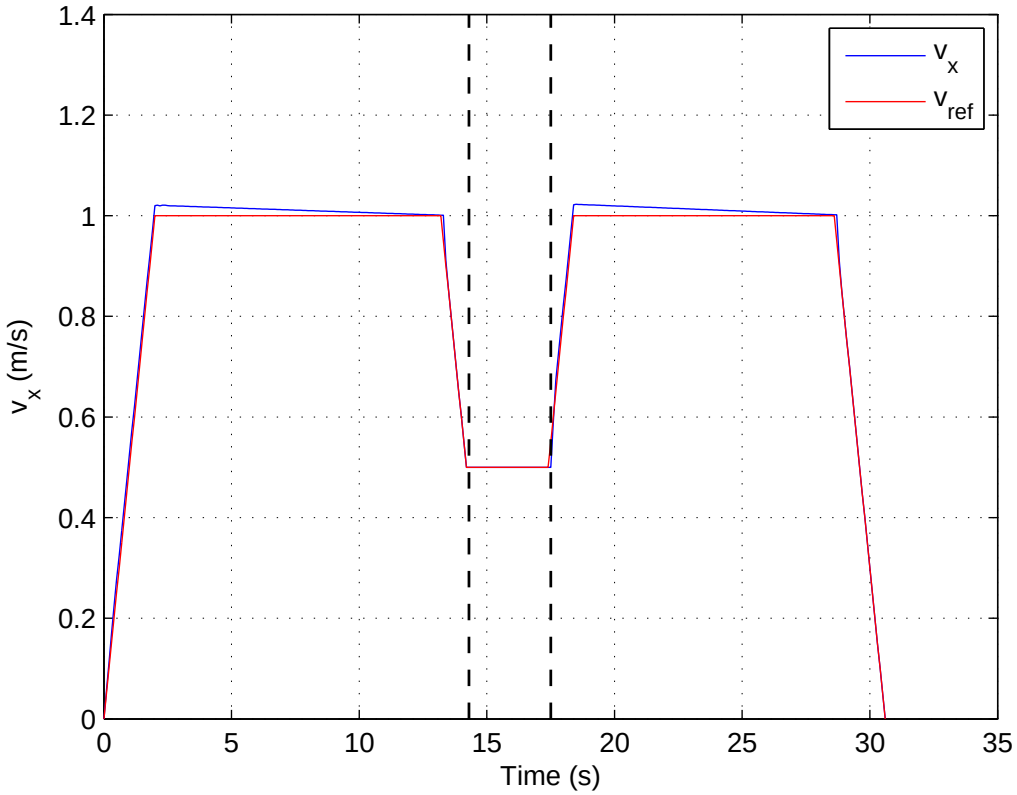

Fig. 4.9. WMR velocity of the combined scenario

The velocity of the WMR sticks very closely to the reference velocity. Small deviations can be seen in the beginning of each wall following mode, because there the penalty of the final goal has priority. Overall the performance is very close to the reference.

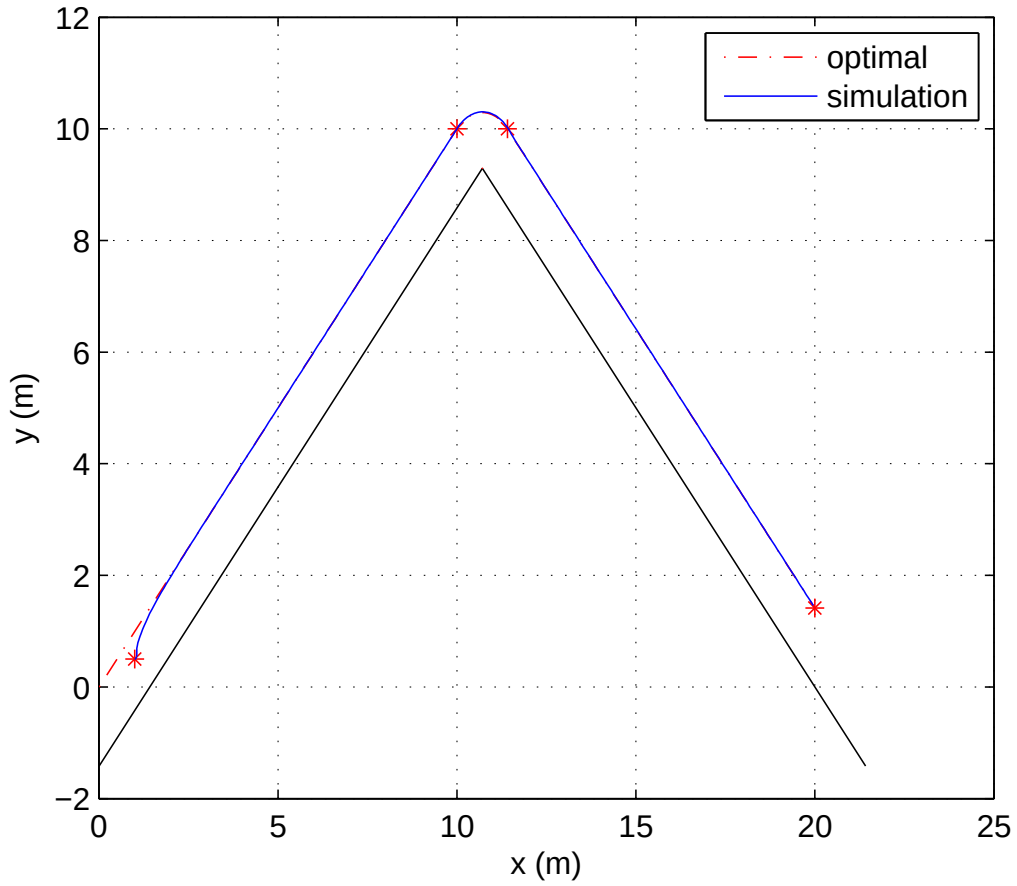

Fig. 4.10. WMR trajectory of the combined scenario

For example, the trajectory is perfectly on the reference trajectory as seen in Fig. 4.10. The offset in the beginning of the scenario is compensated very fast.

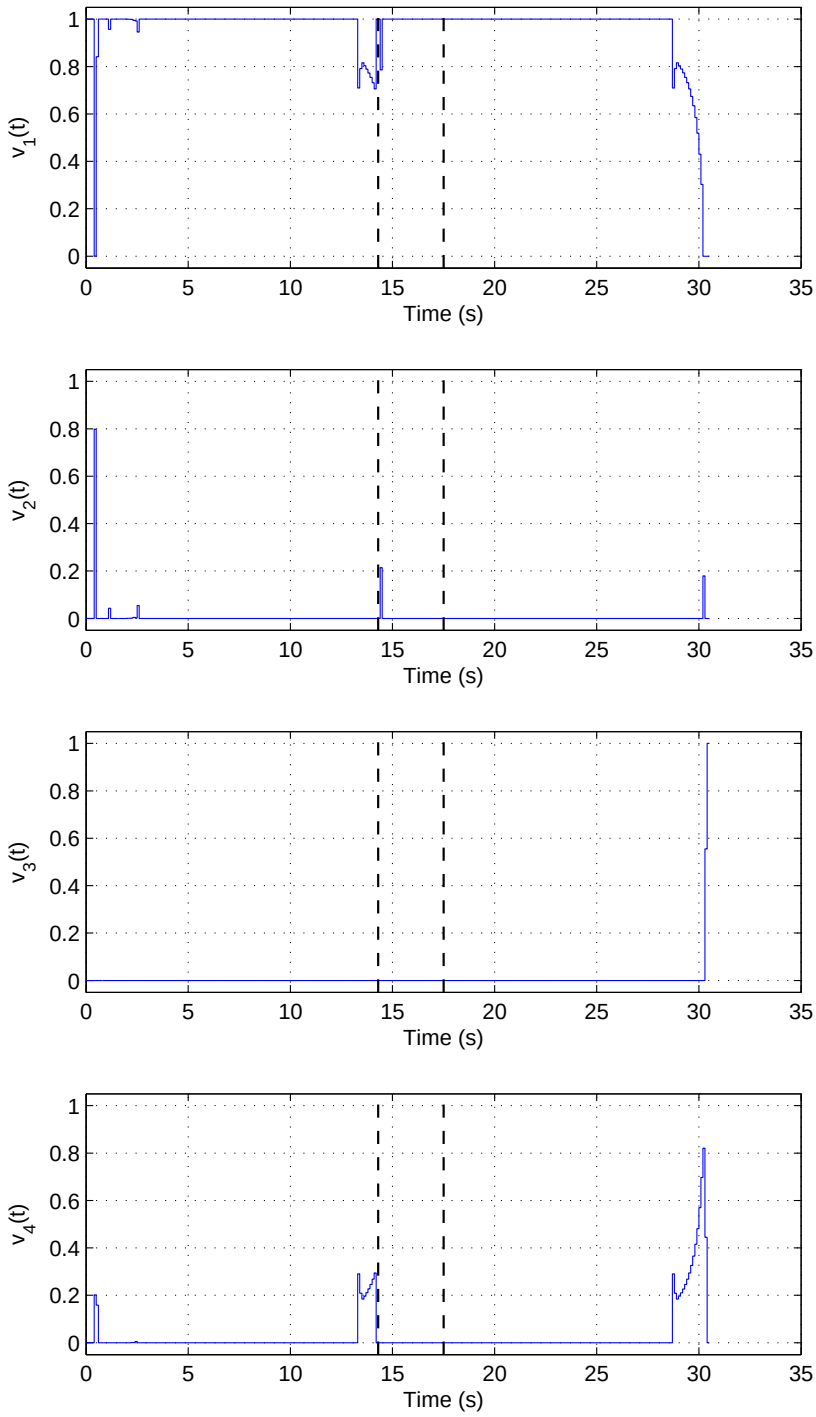

Fig. 4.11. WMR mode values of the combined scenario

In Fig. 4.11 the mode values of the scenario show a 100% use of mode 1 in acceleration and constant driving parts. This mode represents that both wheels propel. In the deceleration parts it is possible to see a high value in mode 4, which represents both wheels are braking regenerative. As discussed in the model equations, regenerative braking torque is a value based on the rotational velocity of the related wheel. That means a wanted deceleration can only be achieved as a compromise between the propelling and braking mode. This is why the value and also the importance of the regenerative braking mode 4 is changing in the deceleration process in order to achieve the same deceleration rate.

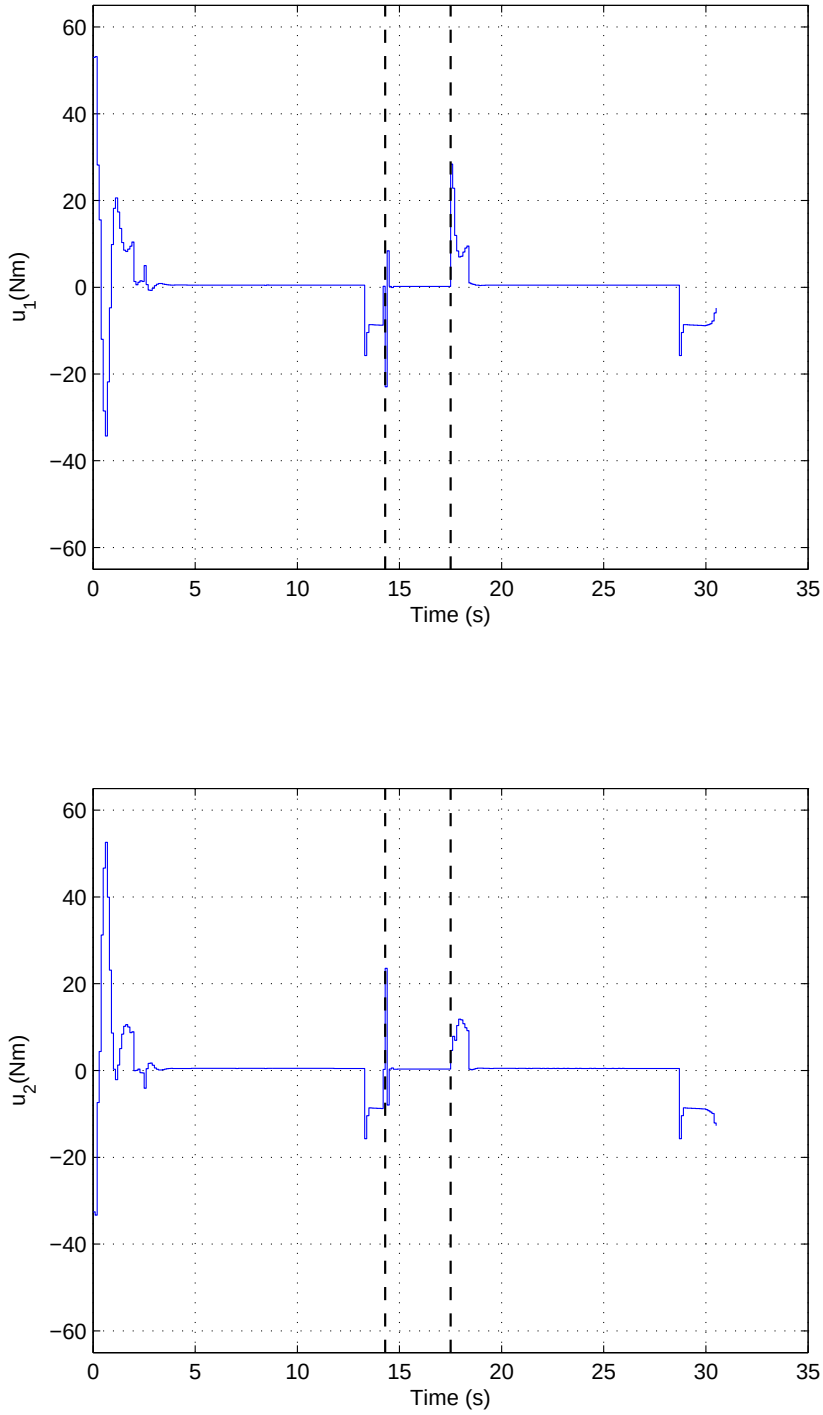

Fig. 4.12. WMR control inputs of the combined scenario

The input torques reflect the behavior of the WMR. Overall no torques higher than 40 Nm and lower than -15 Nm are used. In the scenario parts the changes in input torque are not high, that means that the acceleration and deceleration forces on the user are minimal, which provides a smooth ride for the powered wheelchair user.

4.4 The combined scenario with Gaussian noise on distance to the wall measurements

4.4.1 Development of the used PI

In the combined scenario with Gaussian noise on the distance to the wall measurements all past parts of the combined scenario PI are used again with the same cost coefficients. Only the distance to the wall part changes with a additional included Gaussian noise vector $\mathcal{N}(t)$ with zero mean and a standard deviation of 0.5. The 5% Gaussian error is caused by the MAXBOTIX sonar sensors used for measuring the distance to the wall in a real scenario. [12]

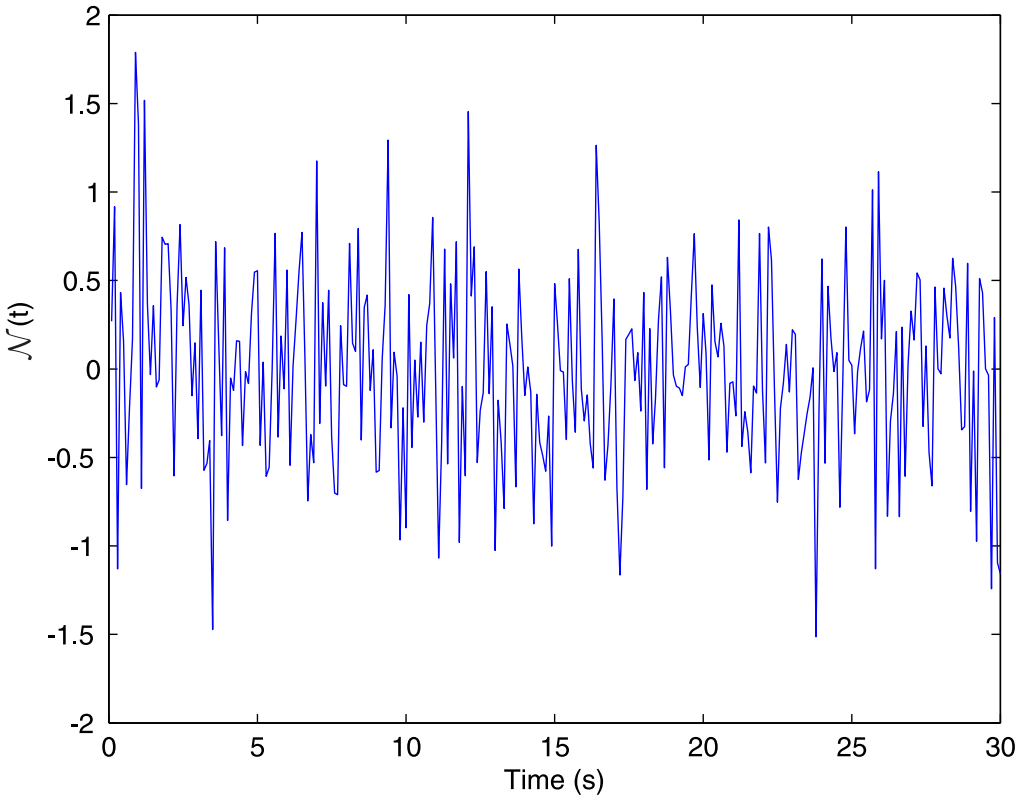

Fig. 4.13. Sample of used Gaussian noise $\mathcal{N}(t)$ over 30 s

Because of the Gaussian noise being the result of measurement problems, the noise affects the system at every new measurement, which is the partition size of the control $t_s = 0.1$, so the plot has a underlying frequency of 10 Hz. The next formula shows the implementation of the presented noise in the PI.

$$c_d \left(\frac{d_{ref} - [d(t) + c_n \mathcal{N}(t)]}{d_{ref}} \right)^2 \tag{4.16}$$

The constant $c_n = 0.05$ produces an approximate 5% error on the distance to the wall measurement. This error is included to mimic the measurements of sonar sensors in real implementations. For every following simulation the same noise vector was used in the optimization process to make drawing comparisons possible and allow transparency of the whole optimization process. The simulations with noise should

additionally show the stability of the MPC control solution. The used full PI has the following form:

$$J_{gaussian} = \int_0^T \Bigg[c_{xf} \frac{(\overline{x}_F(T) - \overline{x}(t))^T (\overline{x}_F(T) - \overline{x}(t))}{(\overline{x}_F(T) - \overline{x}(t_0))^T (\overline{x}_F(T) - \overline{x}(t_0))} + c_d \left(\frac{d_{ref} - [d(t) + c_n \mathcal{N}(t)]}{d_{ref}} \right)^2 + c_\theta \left(\theta_{ref}(t) - \theta(t) \right)^2 + c_v \left(\frac{v_{ref} - v_x(t)}{v_{ref}} \right)^2 + c_e \left[v_1(t) \left(u_{11}(t)^2 + u_{21}(t)^2 \right) + v_2(t) \left(u_{22}(t)^2 \right) + v_3(t) \left(u_{13}(t)^2 \right) \right] \Bigg] dt \tag{4.17}$$

Again depending on the different scenario, the PI is changed by setting the not appropriate coefficients to zero. The weight coefficients are chosen as the best performing combination for the driving tasks and are given in Table 4.2.

Table 4.2
Weight coefficients in the wall following and corning part of the combined Gaussian scenario

	c_{xf}	c_d	c_v	c_e	c_θ	c_n
wall following	10	1.5	10	0.01	0	0.05
cornering	0	1.5	10	0.01	10	0.05

The simulation results give an impression of the robustness of MPC to uncertainty caused by Gaussian noise.

4.4.2 simulation of the presented scenario

Following a simulation is needed to show the stability and reaction of the model due to noise and therefore wrong assumptions in the optimization process.

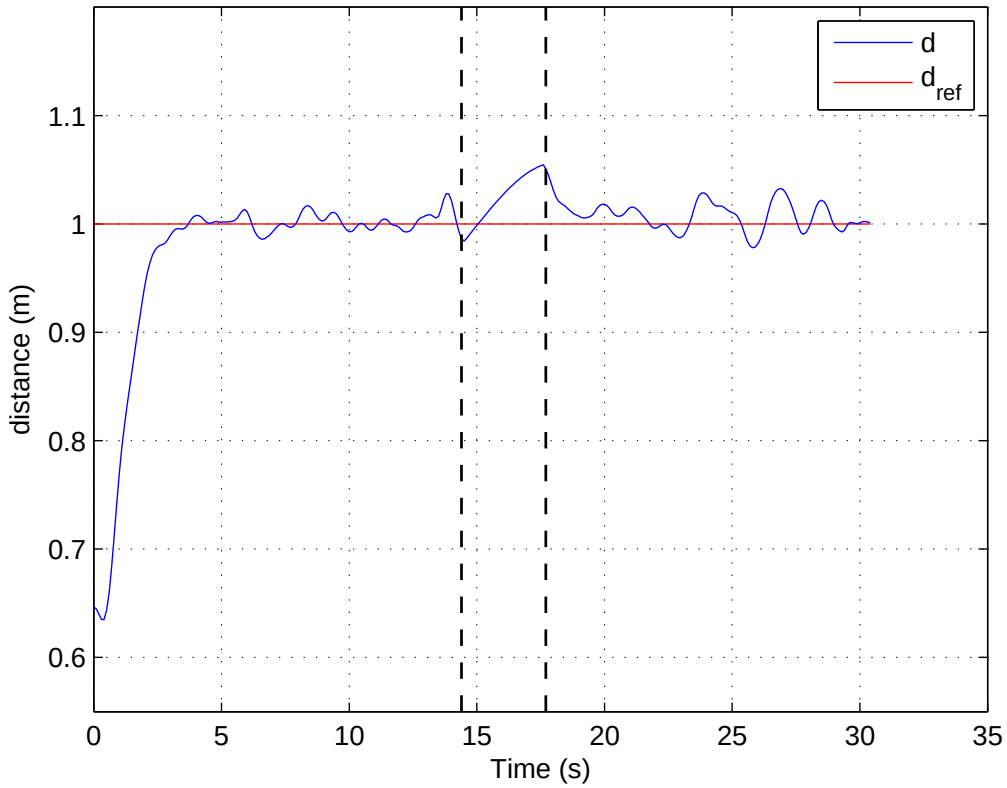

Fig. 4.14. WMR distance to the wall of the combined scenario with Gaussian noise

The behavior of the distance to the wall function of the WMR in Fig. 4.14 is similar to the behavior in Fig. 4.8. The only difference is the Gaussian noise on with zero mean, which forces the WMR to smaller correction on the way to the final goal. In the cornering part again an accumulated error can be seen, which is similar to Fig. 4.8 corrected in the beginning of the second wall following simulation. In the second wall following part of the simulation in Fig. 4.14 the noise with zero mean is influencing the trajectory and the actual distance to the wall.

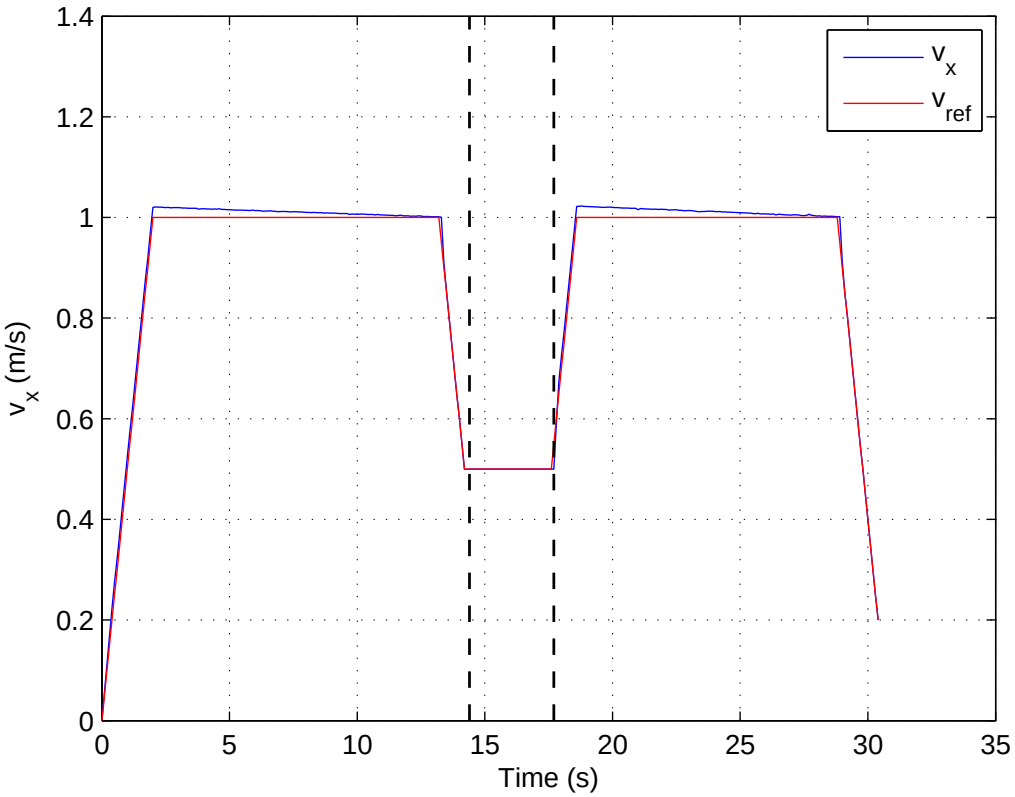

Fig. 4.15. WMR velocity of the combined scenario with 5% Gaussian noise

It is possible to recognize small oscillations in the velocity due to the noise, but still everything is close to the reference. These oscillations are so small and have nearly no impact on the velocity tracking. Nevertheless this shows an enormous stability of the model with noise on the distance to the wall measurements. The black doted lines as boundaries of the cornering scenario tell us that the transition of the PI is still working and the normal cornering speed is reached.

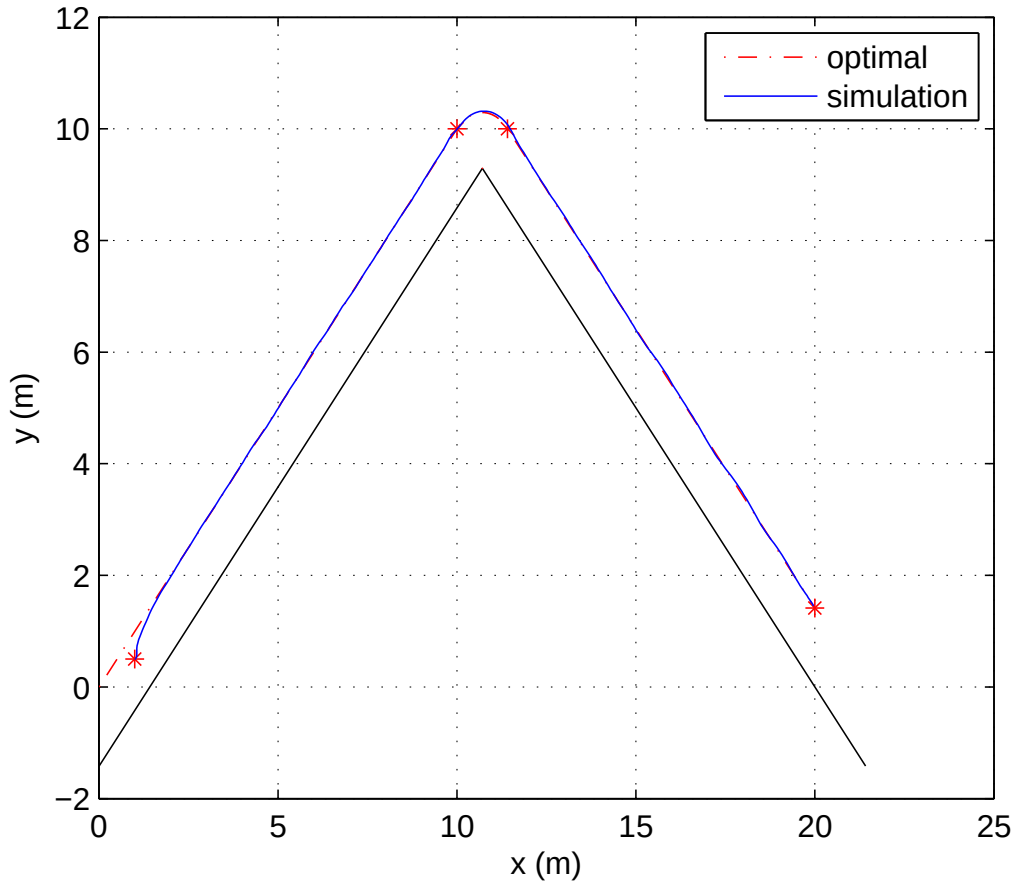

Fig. 4.16. WMR trajectory of the combined scenario with 5% Gaussian noise

In the trajectory plot small deviations from the reference line can be seen. It is easy to recognize that the noise has zero mean, because the WMR spends an equal amount of time under and above the optimal line. Because of the small noise factor of $c_n = 0.05$ it is not a problem for the control to reasonably optimize the trajectory to the reference path. The error is causing oscillations in the trajectory, but the overall performance of the MPC solution is still extraordinary good. This supports the specific robustness of MPC in this driving scenario.

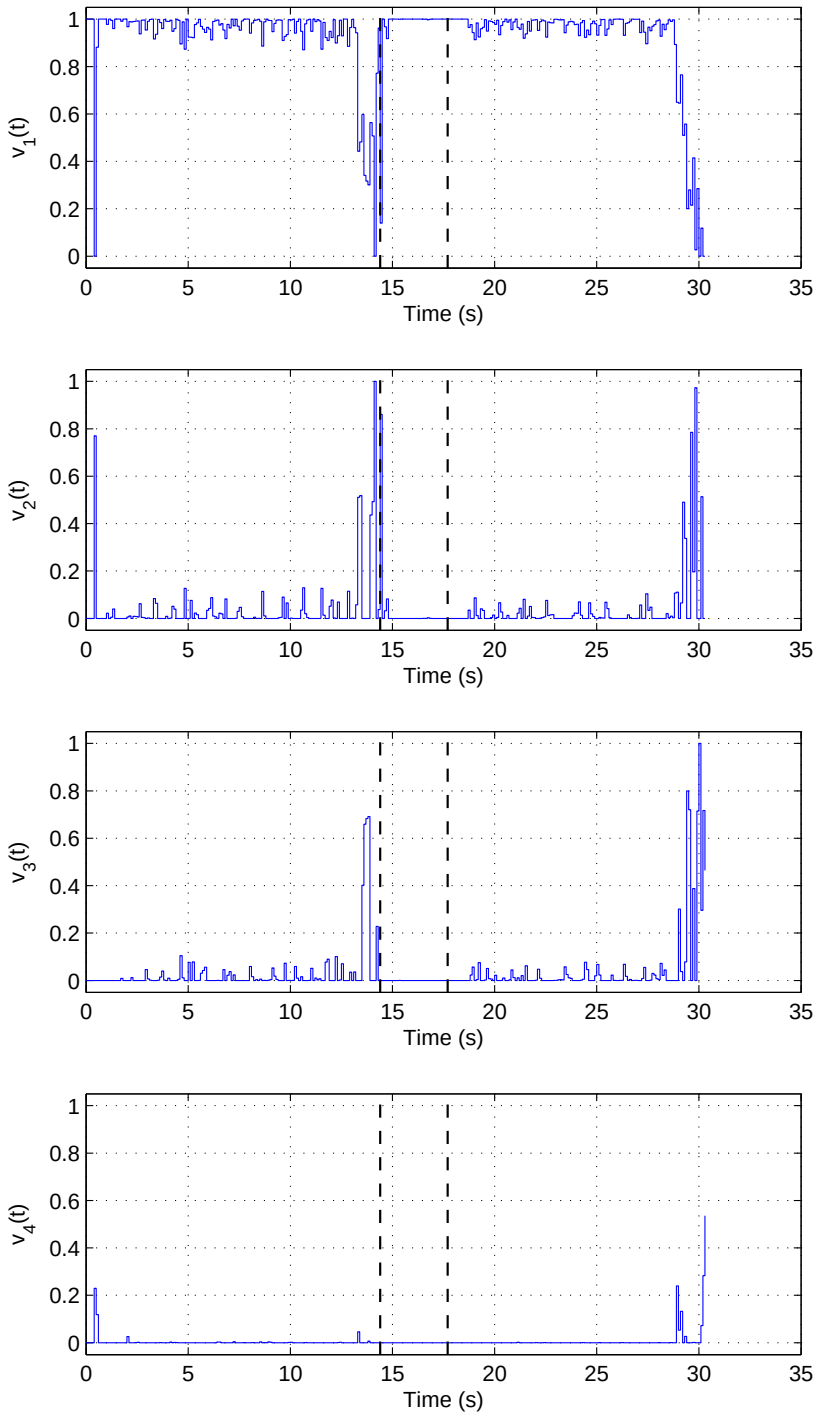

Fig. 4.17. WMR mode values of the combined scenario with 5% Gaussian noise

In the mode diagram it is possible to see the impact of the noise clearly. Mode 1 has for most of the parts of the wall following scenario about $v_1 = 0.95$, which fits to the noise factor of $c_n = 0.05$, which is given on the system. In comparison with the mode diagram of the combined scenario without noise the mode value in Fig. 4.17 is not mostly on a mode value of 1. The use of regenerative braking in the deceleration parts of the scenario is similar to the results without noise used. This supports the statement that although noise is imposed on the system the energy penalty still fulfills the goal to regain energy with regenerative braking in deceleration parts of the scenario.

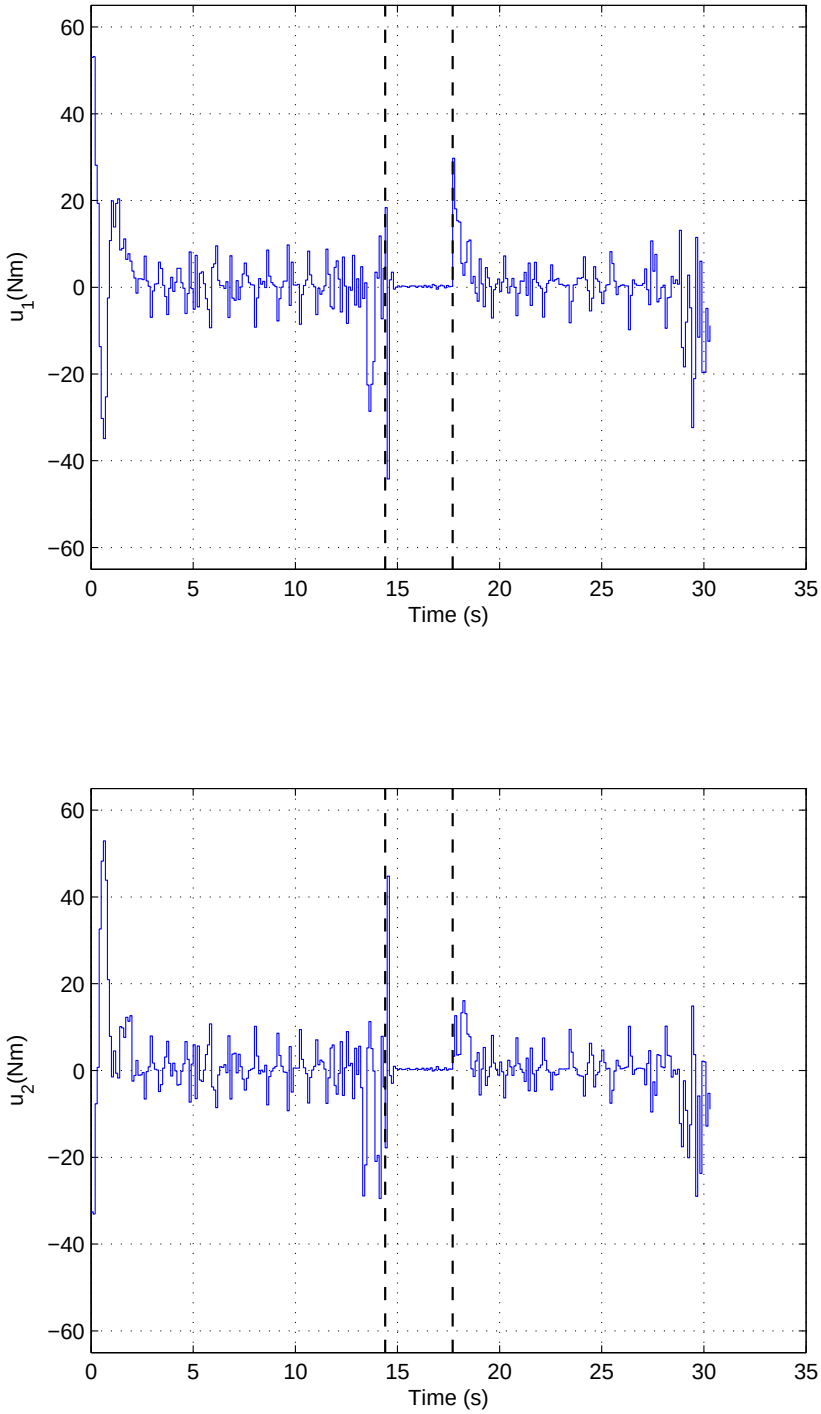

Fig. 4.18. WMR control inputs of the combined scenario with 5% Gaussian noise

In Fig. 4.18 the input torques in comparison with the noiseless simulation of Fig. 4.11 are higher. That means the scenario is more difficult to control in terms of input torque than the simulation without noise and corrections in direction and velocity have to be taken. This result fits to the other plots, because even small turning movements every $t_s = 0.1$ s can only be covered with raised input torques.

5. THE EFFECT OF PARKINSON'S NOISE ON THE COMBINED SCENARIO WITH AND WITHOUT COMPENSATION STRATEGIES USED

In this chapter Parkinsonian noise is imposed on the driving scenario. A filter strategy is derived and used to lower the impact of the noise on the system. Both results are compared and the positive impact of the strategies is evaluated.

5.1 Parkinsonian noise on the combined scenario

In this section the used MPC control strategy will be described and important facts about the simulation will be stated. The PI will be developed and presented.

5.1.1 Overview control system and input conversion

Important for the system is the 100 Hz input for velocity and distance to the wall references.

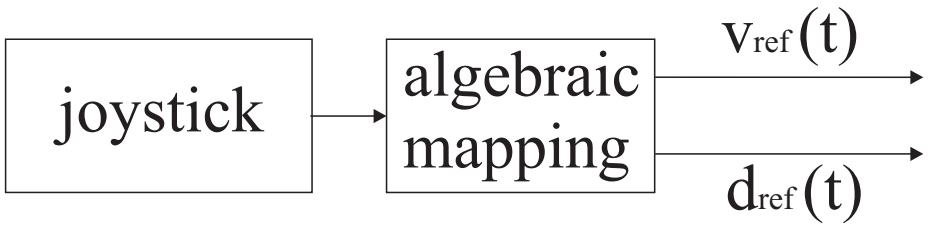

Fig. 5.1. Origin and interpretation of joystick data

A joystick conveys information about position and acceleration. In Fig. 5.1 we see that out of the joystick we have to use these datasets. This is done with an algebraic 1 to 1 mapping on the velocity and distance to the wall references. After the mapping

is defined, the Parkinsonian noise enters the same way in a 1 to 1 mapping on the used references.

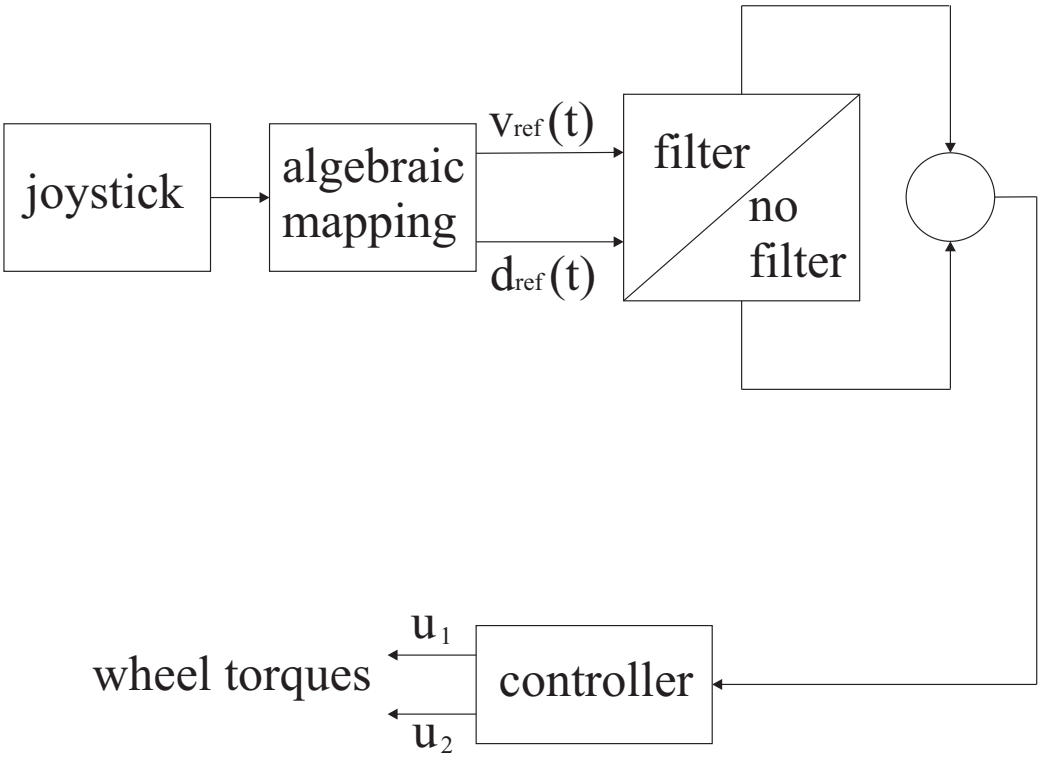

Fig. 5.2. Block diagram of system

Fig. 5.2 shows the whole system. The references influenced by Parkinsonian noise then can be used for further simulations in two possible ways. The first way is to take the negative bias out of the signal and filter the system afterwards to remove a main frequency part of the noise. The other way is to no signal manipulations. After this the 100 Hz references need to fit to the 10 Hz MPC control problem. We are using a special averaging algorithm to calculate the 10 Hz data. For each point kt_s in time, where $k\epsilon\mathcal{N}_0$, this value is the sum out of the actual value and the 9 past values of the 100 Hz signals.

$$v_{ref}(k) = 0.7v_{ref}(k) + \frac{1}{30}\left(\sum_{j=1}^{9} v_{ref}(k-j)\right) \tag{5.1}$$

$$d_{ref}(k) = 0.7 d_{ref}(k) + \frac{1}{30}\left(\sum_{j=1}^{9} d_{ref}(k-j)\right) \tag{5.2}$$

As a result we receive the velocity and distance to the wall reference, which will be given on the controller in Fig. 5.2. The unfiltered and filtered scenario will be simulated in the next sections. First of all it is important to describe the used controller in Fig. 5.2, which is a MPC controller.

5.1.2 MPC controller

For the following simulations the same MPC control strategy as in chapter 4 will be used. That means a performance based control strategy with a 4 partition window will be used. The size of each window is $t_s = 0.1$ s. This means the size of the prediction horizon is 0.4 s. As seen in Fig. 5.2 out of the MPC optimization process the torques u_1 and u_2 for the first calculated partition will be applied to the high fidelity continuous simulation of the WMR.

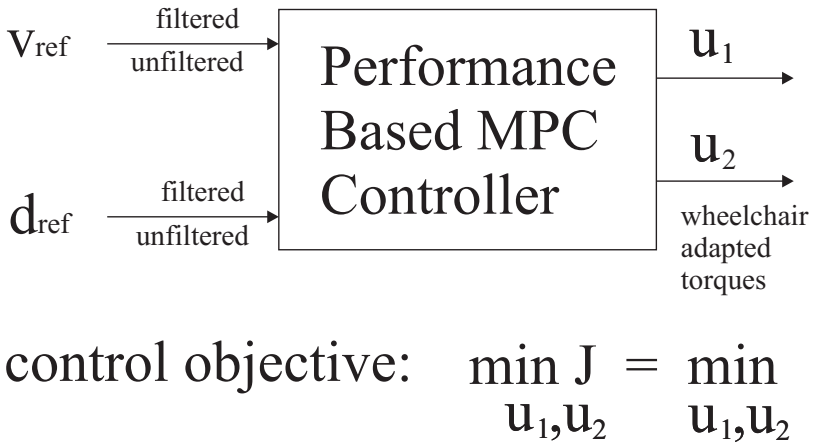

Fig. 5.3. Block diagram of the MPC controller

Fig. 5.3 indicates that the filtered or the unfiltered 10 Hz references will be used in the performance based MPC controller as a basis for the optimization process. The goal of this process is the minimization of a cost J, which is defined by a PI with

penalty values if the robot is not moving the wanted way. In the MATLAB simulation the tolerances for the MPC controller in the optimization toolbox are all set to 10^{-7}. That means that TolCon = 10^{-7}, TolX = 10^{-7} and TolFun = 10^{-7}. The exact PI will be discussed in the next subsection.

5.1.3 Heuristic Development of the Performance Index

The PI of the Parkinsonian noise scenario differs from the used PI in the combined scenario with Gaussian noise in chapter 4 in the velocity and distance parts. Velocity and distance references now have an underlying Parkinsonian noise influence, which is changing the reference trajectory, which the control attempts to track. The Gaussian noise due to the noisy distance to the wall measurements of the two sonar sensors is still included as done in chapter 4. The Gaussian noise coefficient is still $c_n = 0.05$.

The used Parkinsonian noise in this chapter is mimicked real Parkinsonian power spectrum data. The postural and not the rest tremor is used, because a handling of a joystick needs movement in the wrist and arm. [13] For our purposes we considered the side lobes at ± 1 Hz with 40% and ± 2 Hz with 20% of the center frequency maximum power to be the most significant characteristics. Although in the paper a frequency of 5 Hz was considered the Parkinsonian frequency is depending on multiple factors. In this research a center frequency of 3.8 Hz is considered, because it is a common Parkinsonian wrist tremor and is close to the frequencies of other research that determined a steady state frequency behavior of the Parkinsonian wrist tremor. [4] To develop the Parkinsonian noise function, an amplitude modulated cosine wave with magnitudes as peak values is given:

$$(K_0 + K_1 \cos(2\pi t \text{ Hz}) + K_2 \cos(2\pi t 2 \text{ Hz})) \cos(2\pi t 3.8 \text{ Hz}) \tag{5.3}$$

The effective value of a cosine wave $K\cos(\omega t)$ is $K_{eff} = \frac{K}{\sqrt{2}}$, but this is not relevant because the $\sqrt{2}$ terms are cancelling out of the formula. With the trig identity used it is possible to present the function in another form:

$$\begin{aligned} K_0\cos(2\pi t 3.8\text{ Hz}) + 0.5K_1\cos(2\pi t 2.8\text{ Hz}) + 0.5K_1\cos(2\pi t 4.8\text{ Hz}) + \\ 0.5K_2\cos(2\pi t 1.8\text{ Hz}) + 0.5K_2\cos(2\pi t 5.8\text{ Hz}) \end{aligned} \tag{5.4}$$

Cosines of different frequencies are orthogonal functions. Therefore the power in each cosine of a different frequency is proportional to the square of the magnitude. Thus to achieve a 40% and 20% relationship in the side lobe powers:

$$\begin{aligned} 0.4K_0^2 = 0.25K_1^2 \Rightarrow K_1 = \sqrt{1.6}K_0 \approx 1.265K_0 \\ 0.2K_0^2 = 0.25K_2^2 \Rightarrow K_2 = \sqrt{0.8}K_0 \approx 0.9844K_0 \end{aligned} \tag{5.5}$$

Another characteristics of Parkinsonian noise is a negative bias, which is responsible for a 2 to 1 ratio of the negative amplitude in comparison with the positive amplitude of the total signal. [13] With a $K_0 = 1$ the bias adjustment of the function has a value of 1 too. The total formula then has the following form

$$n_p(t) = -1 + \left(1 + \sqrt{1.6}\cos(2\pi t\text{ Hz}) + \sqrt{0.8}\cos(2\pi t 2\text{ Hz})\right)\cos(2\pi t 3.8\text{ Hz}) \tag{5.6}$$

This amplitude modulation with a center Parkinsonian frequency of $f_0 = 3.8$ Hz derived from real frequency power spectrum data of persons suffering under Parkinson's disease is used for the simulations.

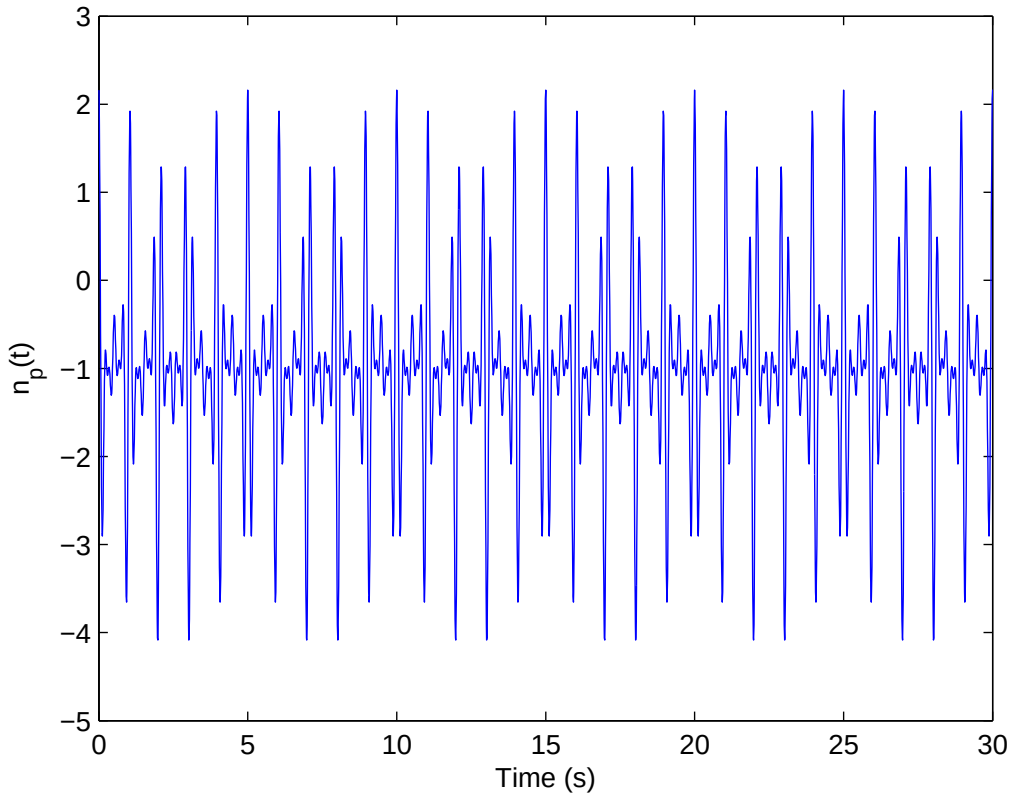

Fig. 5.4. Sample of used Parkinsonian noise $n_p(t)$ over 30 s.

For the implementation a Parkinsonian error of 10% and 20% caused by the disease was considered as reasonable. For the 10% error a $c_p = \frac{1}{30}$ and for the 20% error a $c_p = \frac{2}{30}$ is needed. The velocity term is one of the affected parts of the PI:

$$c_v \left(\frac{[v_{ref}(t) + c_p n_p(t)] - v_x(t)}{v_{ref,max}} \right)^2 \tag{5.7}$$

The last affected term is the reference distance to the wall, which part of the PI has already the Gaussian noise included:

$$c_d \left(\frac{[d_{ref} + c_p n_p(t)] - [d(t) + c_n \mathcal{N}(t)]}{d_{ref}} \right)^2 \tag{5.8}$$

All together a cost function J_{Park} follows:

$$
\begin{aligned}
J_p = \int_0^T \Bigg[& c_{xf} \frac{(\overline{x}_F(T) - \overline{x}(t))^T (\overline{x}_F(T) - \overline{x}(t))}{(\overline{x}_F(T) - \overline{x}(t_0))^T (\overline{x}_F(T) - \overline{x}(t_0))} \\
& + c_d \left(\frac{[d_{ref} + c_p n_p(t)] - [d(t) + c_n \mathcal{N}(t)]}{d_{ref}} \right)^2 + c_\theta \left(\theta_{ref}(t) - \theta(t) \right)^2 \\
& + c_v \left(\frac{[v_{ref}(t) + c_p n_p(t)] - v_x(t)}{v_{ref,max}} \right)^2 \\
& + c_e \left[v_1(t) \left(u_{11}(t)^2 + u_{21}(t)^2 \right) + v_2(t) \left(u_{22}(t)^2 \right) + v_3(t) \left(u_{13}(t)^2 \right) \right] \Bigg] \, dt
\end{aligned}
\tag{5.9}
$$

The actual weight coefficients used are the best coefficients after a quantitative and qualitative search with the goal of achieving the best performance for the driving scenarios.

Table 5.1
Overview of the cost coefficients used in the Parkinsonian noise on distance and velocity references scenario

	c_{xf}	c_d	c_v	c_e	c_θ	c_n	c_p
wall following	10	1.5	10	0.01	0	0.05	$\frac{1}{30}$ or $\frac{2}{30}$
cornering	0	1.5	10	0.01	10	0.05	$\frac{1}{30}$ or $\frac{2}{30}$

5.2 Notch filtering of the Parkinsonian noise on the combined scenario

5.2.1 Introduction of noise filtering

It is known that the maximum intended joystick frequency oscillations are between 4 Hz and 10 Hz. [14] Parkinson's disease center frequency tremor in the wrist is between 3.5 Hz and 7.5 Hz. [15] That means that it is not possible to use a high pass filter, because then other important wanted actions are filtered out too. Other researchers just lowered the sensitivity of the device, but this is a not comparable inefficient and performance losing strategy. [16] It is necessary to filter out the main

lobe of the Parkinsonian noise effectively with a narrow frequency range. This way the WMR drives extraordinary good not only under safety aspects but with high real time performance.

5.2.2 Derivation of the notch filter

To build a notch filter it is possible to take a Butterworth low-pass filter of first order with the transfer function in the Laplace coordinate system:

$$H_{LP}(s) = \frac{1}{s+1} \tag{5.10}$$

This Butterworth filter has a ideal response for frequencies between 0Hz and 1 Hz and at 1 Hz it is 3dB down and decreases with 20dB/decade. Using a low-pass filter to band-reject transformation:

$$s \sim \frac{Bs}{s^2 + w_0^2} \tag{5.11}$$

We obtain the transfer function of a band-reject filter. In this thesis a notch frequency of $f_0 = \frac{w_0}{2\pi} = 3.8$ Hz and bandwidth of $B = 1\frac{\text{rad}}{\text{s}}$ is used for the filter:

$$H_{BR}(s) = \frac{s^2 + w_0^2}{s^2 + Bs + w_0^2} \tag{5.12}$$

As a next step a bilinear transformation is needed to transform from the Laplace world to the Z world, because we're considering a discrete system implementation. The bilinear transformation follows using the following substitution:

$$s = \frac{2}{T_s}\frac{z-1}{z+1} \tag{5.13}$$

$T_s = \frac{1}{f_s}$ is the sampling interval. We are assuming that f_s is sufficiently high to avoid frequency warping. The transfer function of a second order notch filter in the Z-domain is:

$$H_{BR}(z) = \frac{\text{Output(z)}}{\text{Input(z)}} = \frac{y(z)}{u(z)} = \frac{\alpha_0 + \alpha_1 z^{-1} + \alpha_2 z^{-2}}{1 + \beta_1 z^{-1} + \beta_2 z^{-2}} \tag{5.14}$$

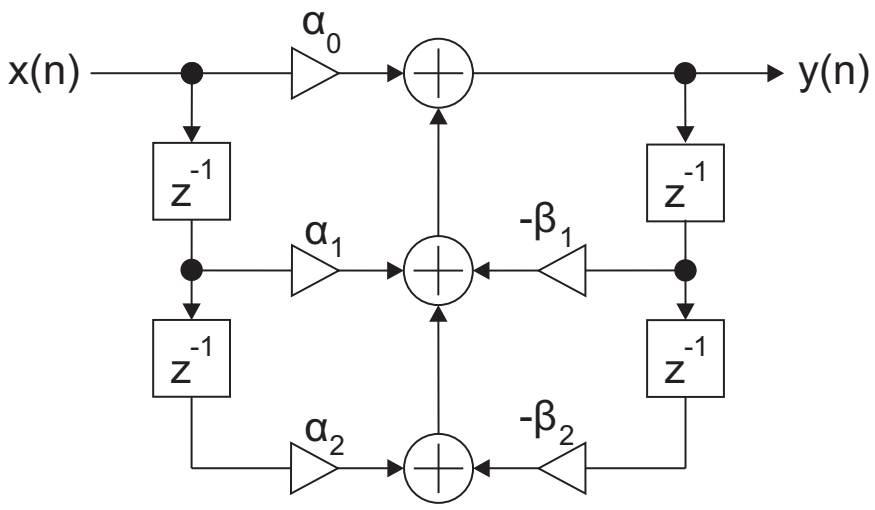

Fig. 5.5. Block diagram of the transfer function

It is possible to implement this structure to the known canonical form shown in Fig. 5.6.

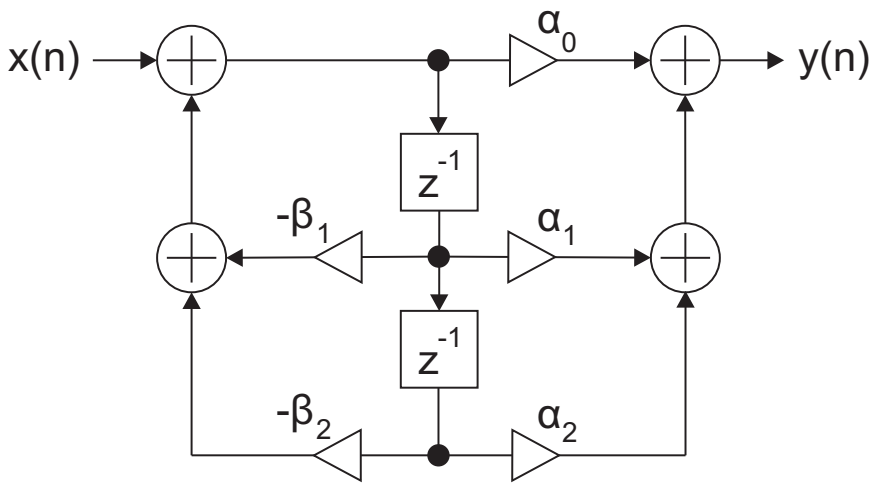

Fig. 5.6. Canonical form of the block diagram of the transfer function

For the used filter the transfer function is:

$$H_{BR}(z) = \frac{\left(w_0^2 + \frac{4}{T_s^2}\right) + z^{-1}\left(2w_0^2 - \frac{8}{T_s^2}\right) + z^{-2}\left(w_0^2 + \frac{4}{T_s^2}\right)}{\left(w_0^2 + B\frac{2}{T_s} + \frac{4}{T_s^2}\right) + z^{-1}\left(2w_0^2 - \frac{8}{T_s^2}\right) + z^{-2}\left(w_0^2 - B\frac{2}{T_s} + \frac{4}{T_s^2}\right)} \tag{5.15}$$

To get the exact form as described in equation (5.14) it is necessary to perform a last manipulation.

$$H_{BR}(z) = \frac{\left(\frac{w_0^2+\frac{4}{T_s^2}}{w_0^2+B\frac{2}{T_s}+\frac{4}{T_s^2}}\right) + z^{-1}\left(\frac{2w_0^2-\frac{8}{T_s^2}}{w_0^2+B\frac{2}{T_s}+\frac{4}{T_s^2}}\right) + z^{-2}\left(\frac{w_0^2+\frac{4}{T_s^2}}{w_0^2+B\frac{2}{T_s}+\frac{4}{T_s^2}}\right)}{1 + z^{-1}\left(\frac{2w_0^2-\frac{8}{T_s^2}}{w_0^2+B\frac{2}{T_s}+\frac{4}{T_s^2}}\right) + z^{-2}\left(\frac{w_0^2-B\frac{2}{T_s}+\frac{4}{T_s^2}}{w_0^2+B\frac{2}{T_s}+\frac{4}{T_s^2}}\right)} \tag{5.16}$$

The named $\alpha_i,\ i\epsilon\{0,1,2\}$ and $\beta_j,\ j\epsilon\{1,2\}$ of equation (5.14) will be used as a substitution of the calculated terms of equation (5.16). To connect equation (5.16) to a different equation consider that:

$$\left(1 + \beta_1 z^{-1} + \beta_2 z^{-2}\right) y(z) = \left(\alpha_0 + \alpha_1 z^{-1} + \alpha_2 z^{-2}\right) u(z) \tag{5.17}$$

The inverse Z-transformation is used to obtain the discrete output equation $y(k)$ of the filter:

$$y(k) + \beta_1 y(k-1) + \beta_2 y(k-2) = \alpha_0 u(k) + \alpha_1 u(k-1) + \alpha_2 u(k-2) \tag{5.18}$$

$$y(k) = \alpha_0 u(k) + \alpha_1 u(k-1) + \alpha_2 u(k-2) - \beta_1 y(k-1) - \beta_2 y(k-2) \tag{5.19}$$

This equation is simply a manipulation of the input-output data stream and can be implemented in the discrete model.

5.3 Presentation of used references and uncertainty influences for simulations

5.3.1 The 10 percent Parkinsonian noise scenarios

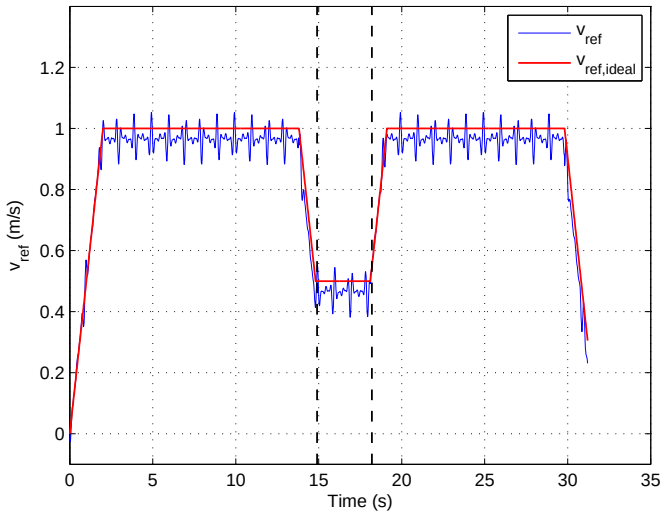

(a) unfiltered

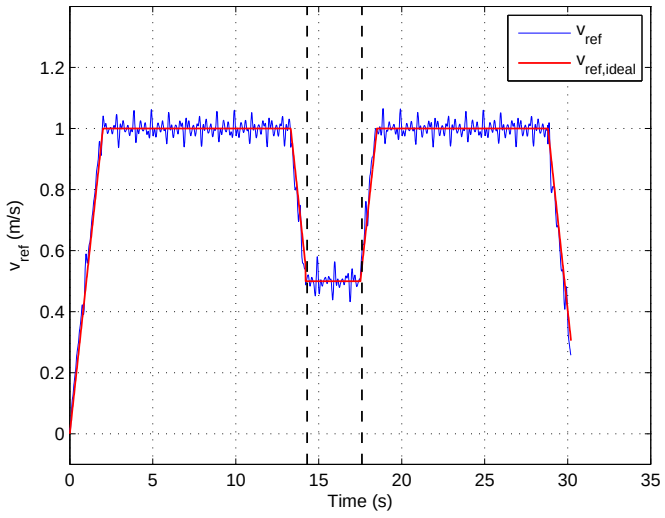

(b) filtered

Fig. 5.7. WMR velocity reference of the combined scenario with 10% Parkinsonian and 5% Gaussian noise

The velocity reference in Fig. 5.7(a) shows at 100 Hz the influence of the 10% Parkinsonian and 5% Gaussian noise on the ideal velocity reference. The negative bias and the high peak to peak noise of $0.3\frac{\mathrm{m}}{\mathrm{s}}$ is easy to recognize. Both plots are stopping at a specific nonzero point in the deceleration process, because the connected simulation reached the used specific stopping criterion. The velocity reference in Fig. 5.7(b) is smoother and a bias to the ideal reference is not possible to recognize. The peak to peak amplitude of the noise is only 50% of the unfiltered reference. The filtered forward velocity reference is one of the major differences why the trajectory looks significantly better than in the normal Parkinsonian scenarios without filter methods used.

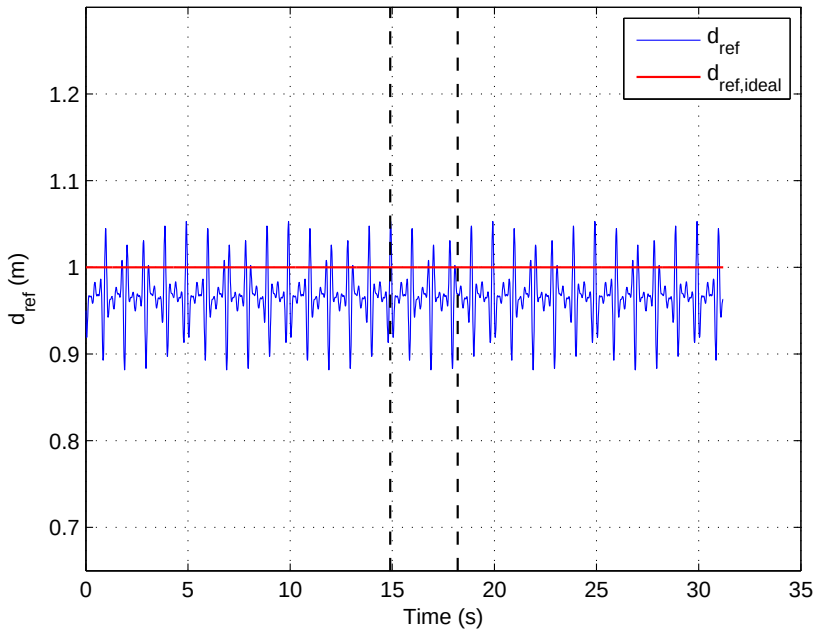

(a) unfiltered

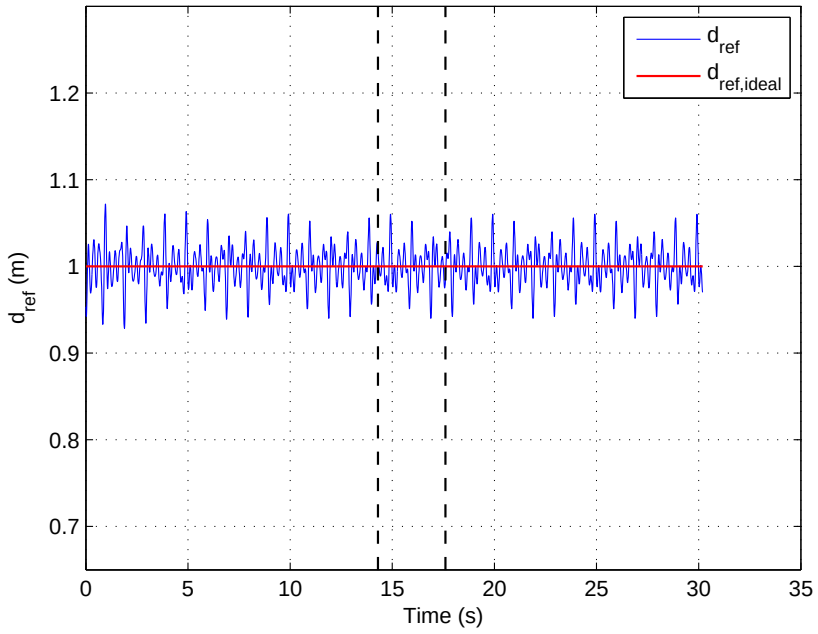

(b) filtered

Fig. 5.8. WMR distance to the wall reference of the combined scenario with 10% Parkinsonian and 5% Gaussian noise

In Fig 5.8 the filtered and biased distance to the wall reference is shown in comparison to the unfiltered distance reference. The peak to peak noise amplitude in Fig. 5.8(b) is only 40% of the unfiltered distance to the wall reference. This shows that the used notch filtering methods erased a main part of the Parkinsonian noise. The mean of the filtered signal is again 1 m, which improves the quality and safety of the driving scenario immense.

5.3.2 The 20 percent Parkinsonian noise scenarios

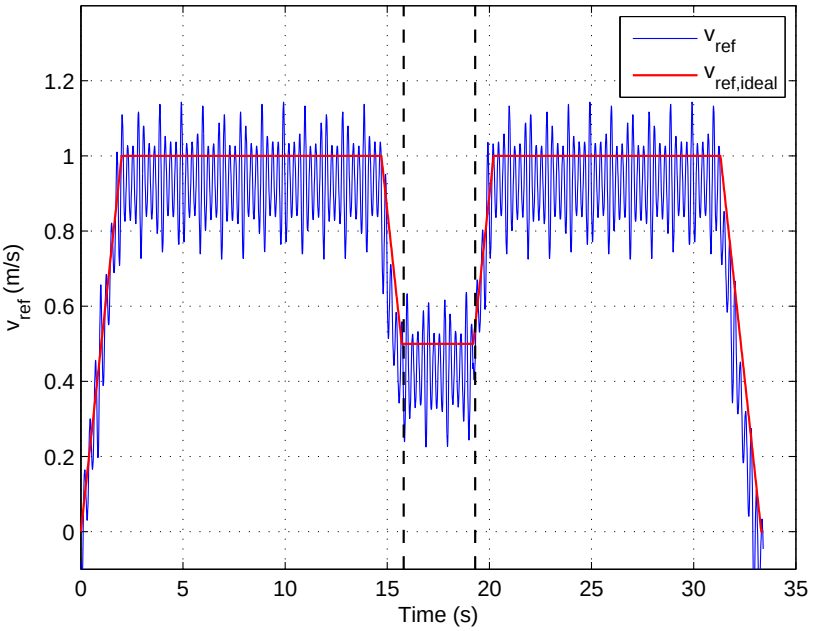

(a) unfiltered

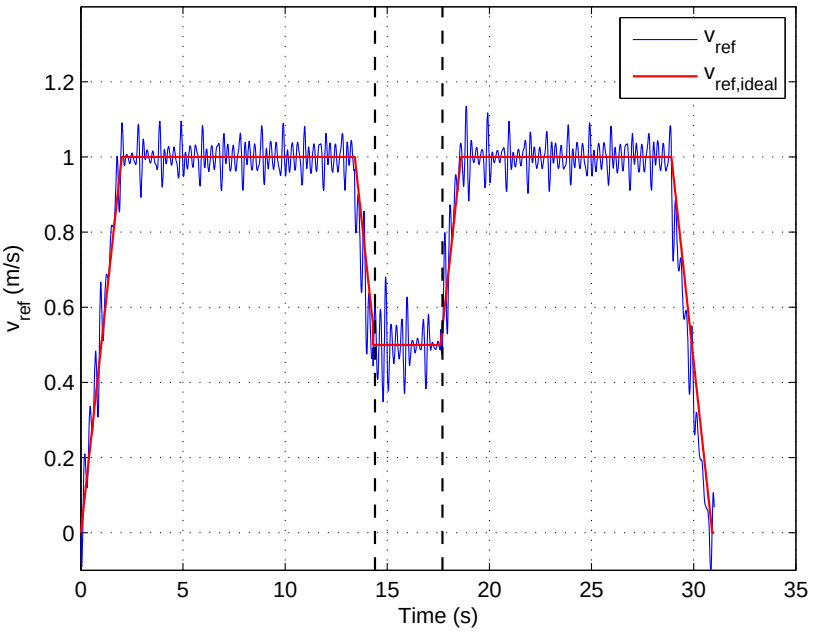

(b) filtered

Fig. 5.9. WMR velocity reference of the combined scenario with 20% Parkinsonian and 5% Gaussian noise

Fig. 5.9 presents the comparison between the unfiltered and filtered velocity references in the 20% Parkinsonian noise scenarios. Again the velocity reference in Fig. 5.9(b) is much smoother and the bias of the Parkinsonian scenario without notch filter is not possible to recognize. The peak to peak noise caused by the Parkinsonian tremor are shrinking through filtering to 50% of the old value. As mentioned already in the 10% scenario, the filtered velocity reference in Fig. 5.9(b) is one of the major points why the filtered simulation is significantly better than in the unfiltered scenarios. Already at this state without simulations, the filter strategies show there high potential in erasing Parkinsonian noise.

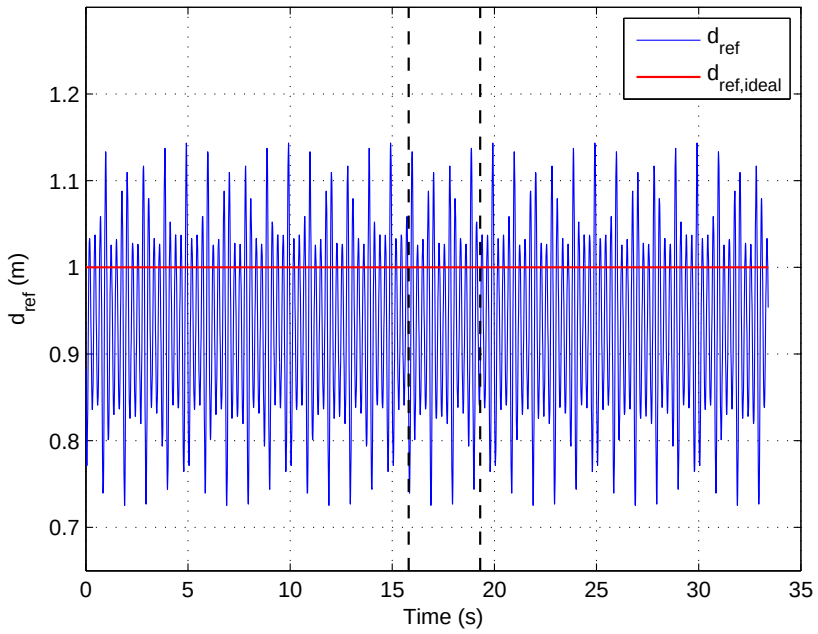

(a) unfiltered

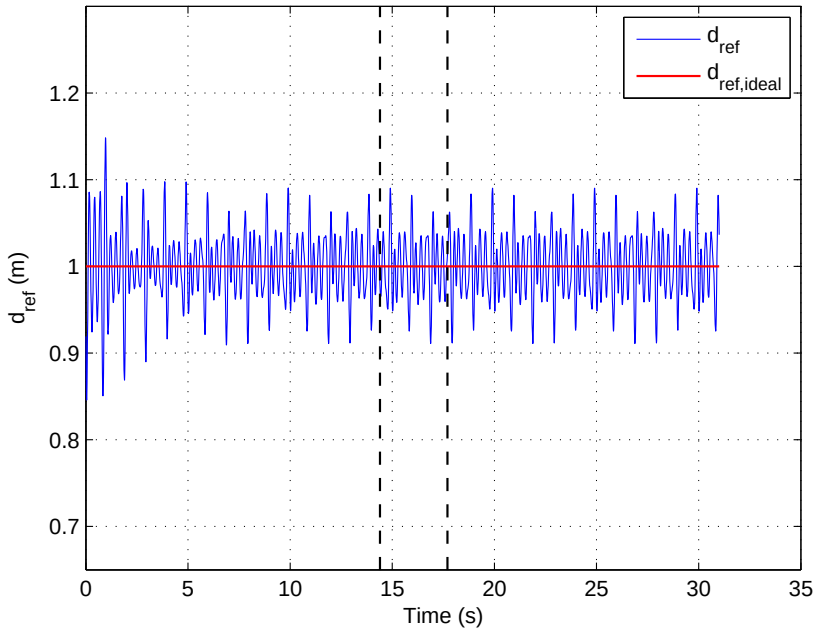

(b) filtered

Fig. 5.10. WMR distance to the wall reference of the combined scenario with 20% Parkinsonian and 5% Gaussian noise

Fig 5.10(b) shows the filtered and biased distance to the wall reference after a 20% influence of Parkinsonian noise. The overall peak to peak distance shrinked to about 0.2 m for the worst cases. The higher frequency content between the mentioned worst case amplitudes has a overall peak to peak distance of 0.1 m. This a significant better result than the 20% Parkinsonian noise scenario without the used control elements and proves again the success of the used filtering methods.

5.3.3 Uncertainty through sensor measurements

For all simulations similar to chapter 4, Gaussian noise enters the calculation of the distance to the wall. This is not a reference but a uncertainty for the whole MPC optimization process with impact on the behavior of the WMR. In Fig. 4.13 the noise $\mathcal{N}(t)$ was introduced. The scaled 5% Gaussian noise of $c_n\mathcal{N}(t)$, where $c_n = 0.05$, enters exactly into this optimization process. The Gaussian and Parkinsonian noise are causing a high uncertainty and the simulation result will show the performance and robustness of this specific MPC scenario.

5.4 Simulation results of the scenarios

5.4.1 The 10 percent Parkinsonian noise scenarios

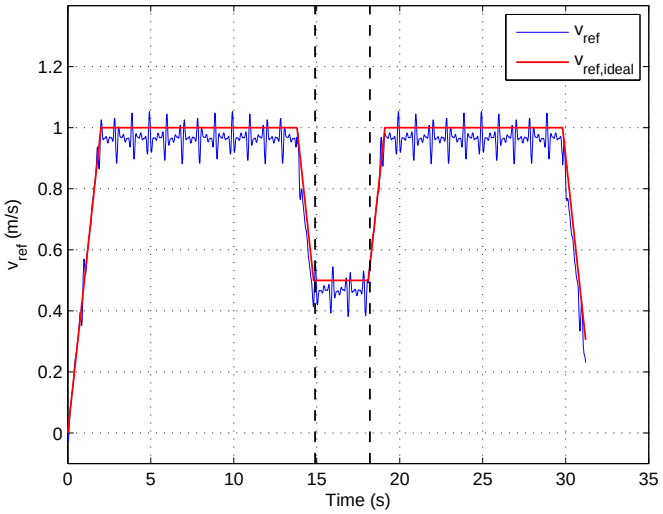

(a) velocity reference

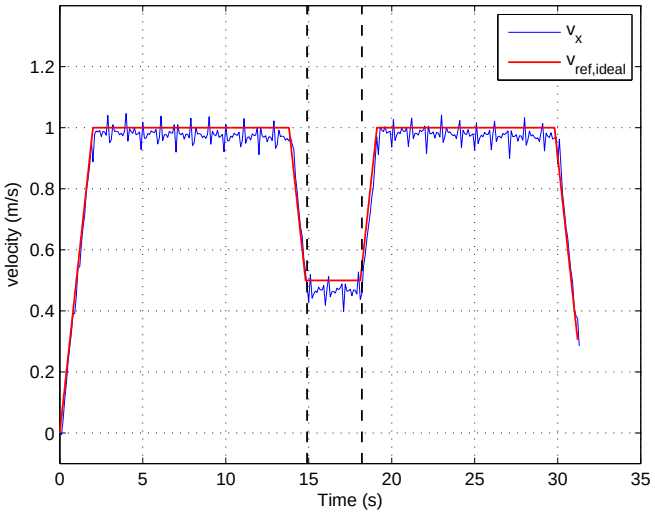

(b) simulated velocity

Fig. 5.11. WMR unfiltered velocity reference in connection with the related WMR forward velocity of the combined scenario with 10% Parkinsonian and 5% Gaussian noise

In Fig. 5.11(b) the simulated forward velocity v_x of the WMR is shown. The unfiltered 10% Parkinsonian scenario is presented. In comparison with the forward velocity in Fig. 5.11(b) the peak to peak noise is about 100% bigger in the reference velocity plot Fig. 5.11(a). This is because of the dynamics of the system and the safety restrictions on the acceleration and velocity as presented in chapter 3 with equation (3.1) and equation (3.2). It is not possible for the system to follow these extreme changes in the velocity reference, although the weight coefficient is relatively high. Additional a energy use penalty is on torque used to propel the wheels. This supports the goal to not to fulfill all of the occurring velocity reference changes.

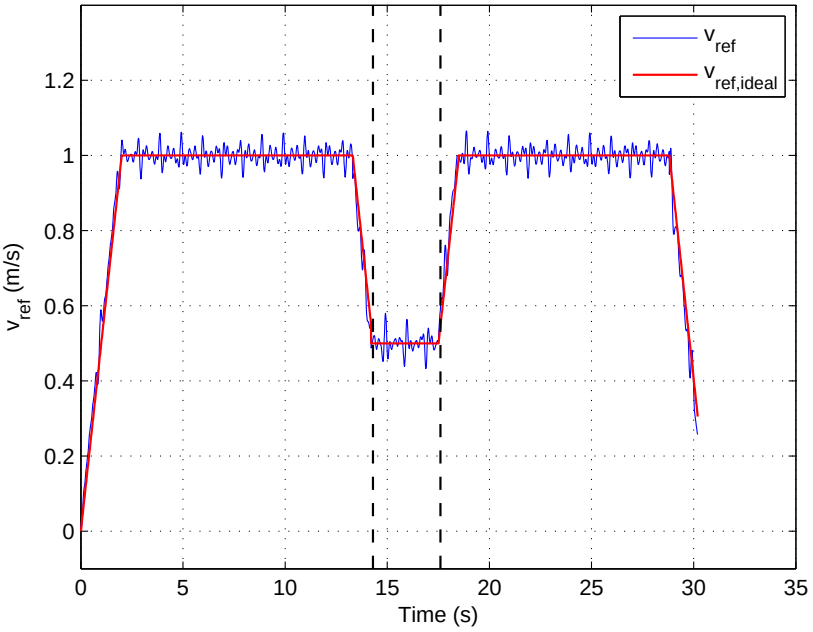

(a) velocity reference

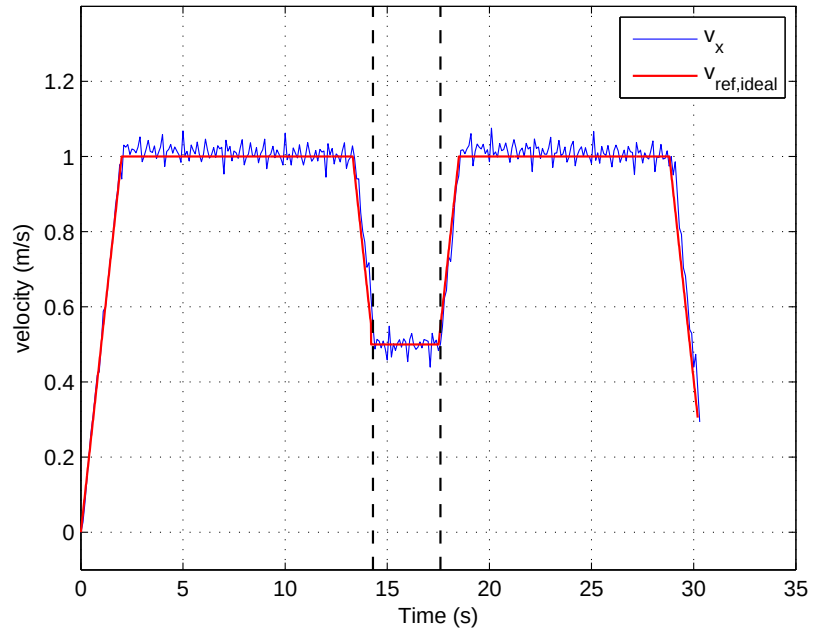

(b) simulated velocity

Fig. 5.12. WMR filtered velocity reference in connection with the related WMR forward velocity of the combined scenario with 10% Parkinsonian and 5% Gaussian noise

The filtered 10% Parkinsonian scenario is shown in Fig. 5.12. Similar to the unfiltered scenario the peak to peak noise amplitude shrinks massively in Fig. 5.12(b) because of the included safety bounds and energy use penalties. This happens, although the peak to peak noise amplitude of the reference in Fig. 5.12(a) was already reduced due to the filtering process. Overall the filtering strategies worked and no bias is possible to recognize in the reference and actual forward velocity v_x.

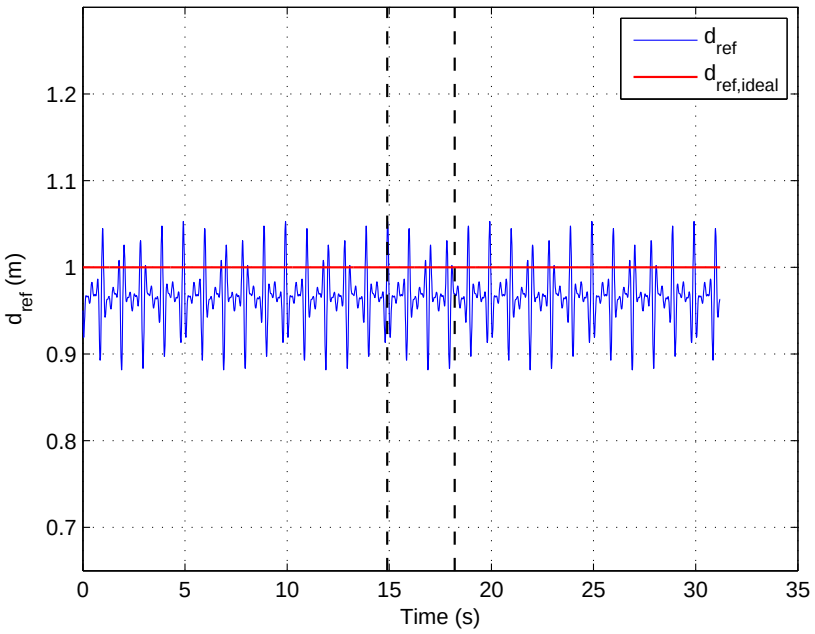

(a) distance to the wall reference

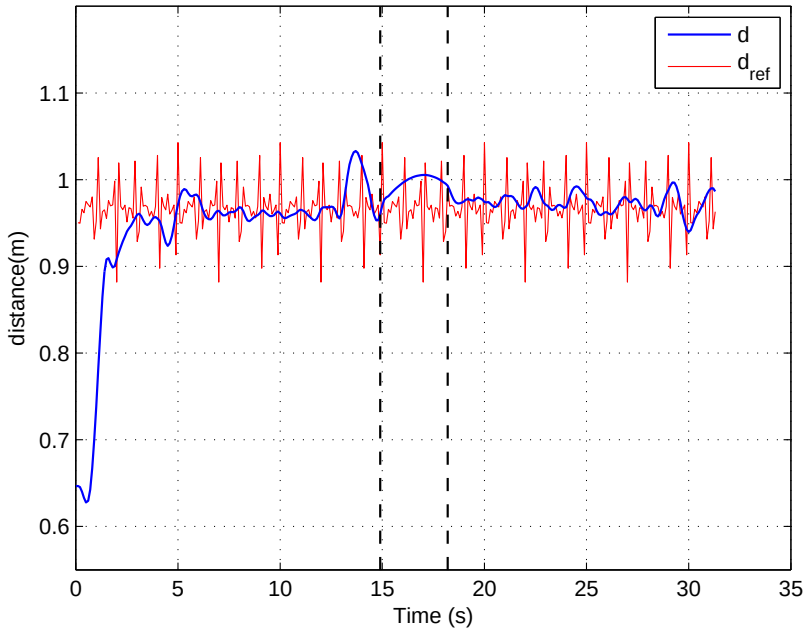

(b) simulated distance to the wall

Fig. 5.13. WMR unfiltered distance reference in connection with the related WMR distance to the wall of the combined scenario with 10% Parkinsonian and 5% Gaussian noise

In Fig. 5.13(a) the already known 100 Hz distance reference of the unfiltered 10% scenario is displayed. In Fig. 5.13(b) this reference distance is shown in 10 Hz, because this is the way the reference enters in the 10 Hz simulation and impacts the optimization process. Fig. 5.13(b) indicates the strong desire of the MPC controller to converge to the distance reference. It also shows the bias of the reference impacting the trajectory of the WMR, because the robot is closer than 1 m to the wall nearly at every point of the simulation.

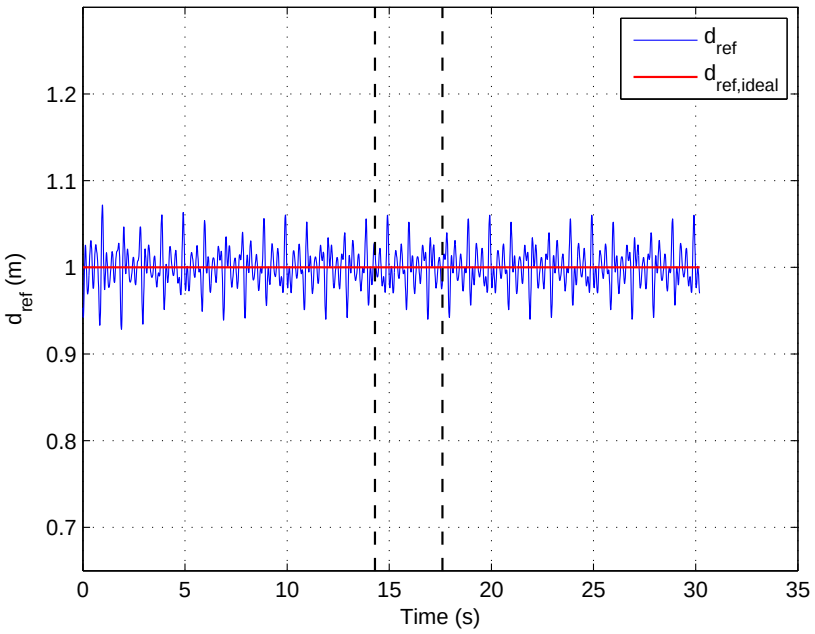

(a) distance to the wall reference

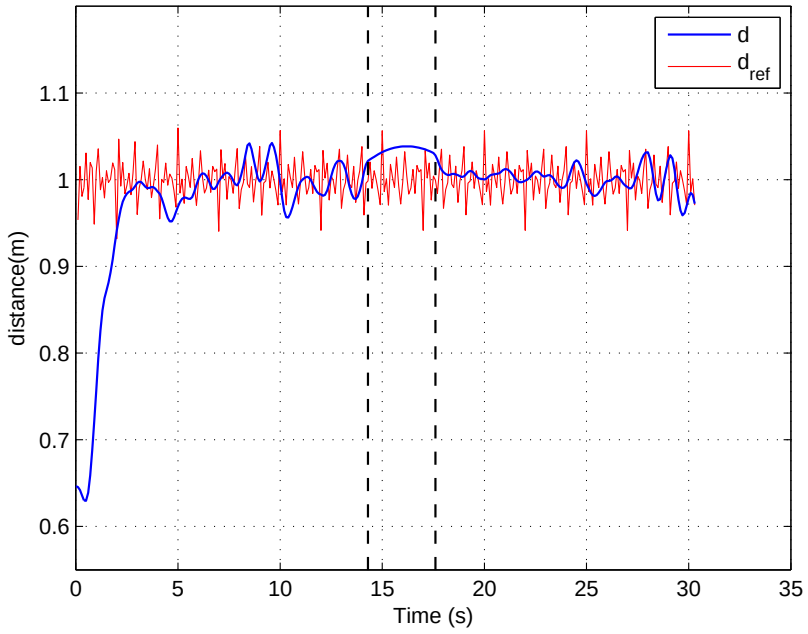

(b) simulated distance to the wall

Fig. 5.14. WMR filtered distance reference in connection with the related WMR distance to the wall of the combined scenario with 10% Parkinsonian and 5% Gaussian noise

In direct contrast the filtered scenario in presented in Fig. 5.14. As expected the simulated distance to the wall in Fig. 5.14(b) is summed up directly on 1 m. This confirms the argument that mainly only a 5% Gaussian noise vector is influencing the WMR. Additional this proves that a main part of the Parkinsonian noise is notched out successfully.

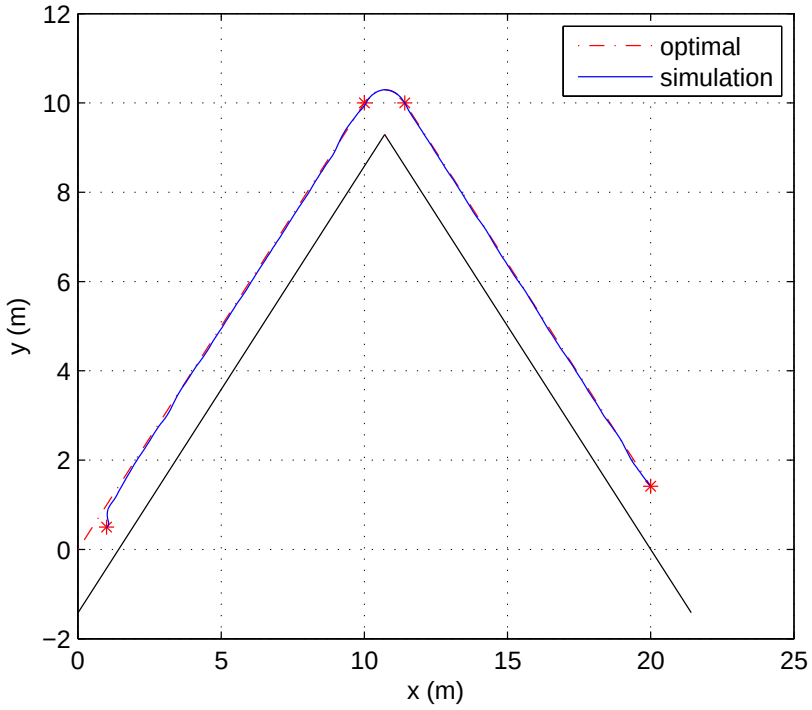

(a) unfiltered

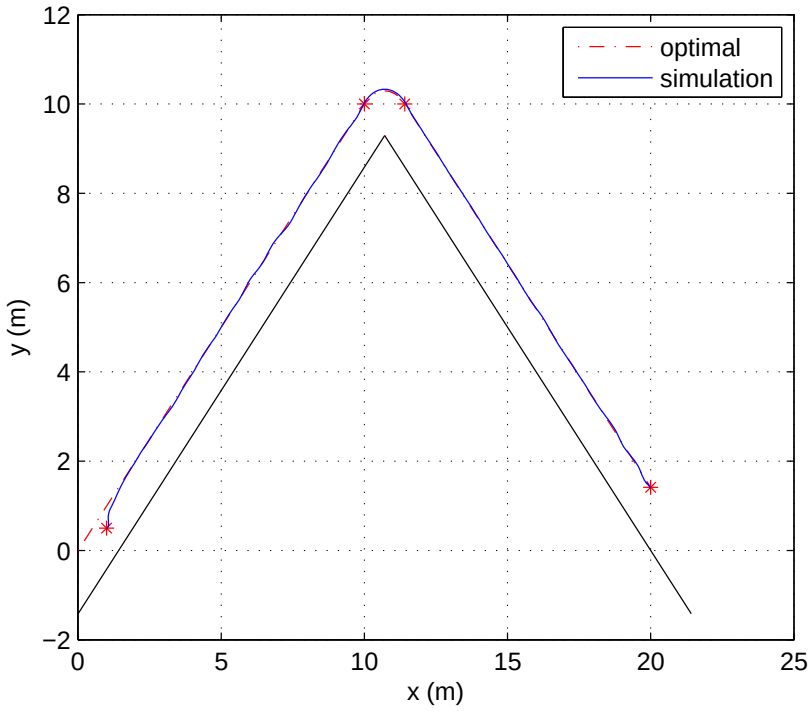

(b) filtered

Fig. 5.15. WMR trajectory of the combined scenario with 10% Parkinsonian and 5% Gaussian noise

In comparison with Fig. 5.15(a) the result of Fig. 5.15(b) shows a smoother trajectory and an good driving behavior improvement. It is not possible to recognize any bigger oscillations in the filtered scenario. As seen in Fig. 5.15(b) the WMR is more on the optimal line and deviations are equally distributed over and under the optimal line. Fig. 5.15(a) is closer to the wall due to a bias caused by the Parkinsonian tremor. Both trajectories are influenced by 5% Gaussian noise on the distance to the wall measurement. Even though this fact has a negative effect the driving performance in both scenarios is extraordinary good. These results support the stability of the chosen model and the robustness of the specific MPC controller.

5.4.2 The 20 percent Parkinsonian noise scenarios

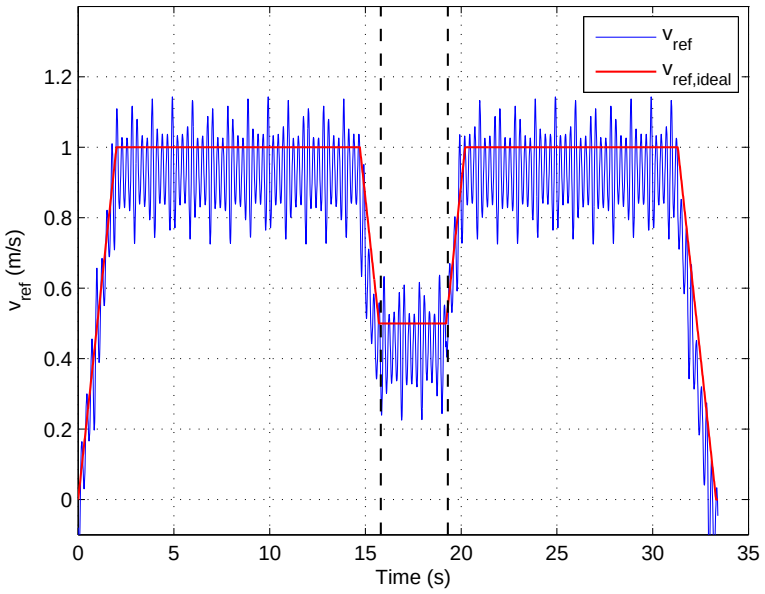

(a) velocity reference

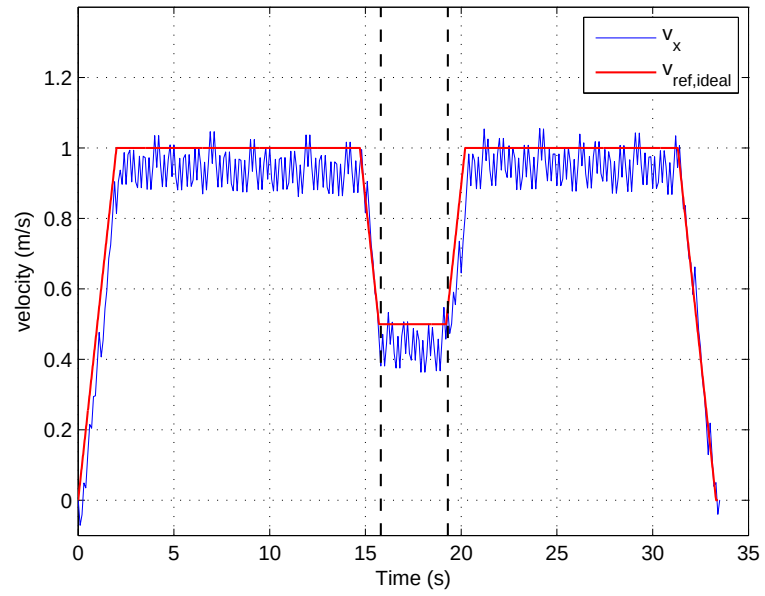

(b) simulated velocity

Fig. 5.16. WMR unfiltered velocity reference in connection with the related WMR forward velocity of the combined scenario with 20% Parkinsonian and 5% Gaussian noise

Similar to the results in the 10% scenario in Fig. 5.17 the reference velocity and the simulated forward velocity v_x of the WMR are shown. In direct contrast the filter has to deal with a much higher peak to peak noise amplitude and the mean of reference velocities in the wall following and cornering parts of the scenario are much lower. Again the peak to peak noise amplitude is much lower in Fig. 5.16(b), because of the already introduced safety bounds of the system and energy penalties of the controller. For example in Fig. 5.16(a), the velocity reference, it is possible that the reference is changing in $t_s = 0.1$ s about 0.3 $\frac{\mathrm{m}}{\mathrm{s}}$. Because of the acceleration bounds in equation (3.2) of the system, the WMR can only change 0.09 $\frac{\mathrm{m}}{\mathrm{s}}$ in 0.1 s. That is less than $\frac{1}{3}$ and similar relations are possible to recognize in Fig. 5.17.

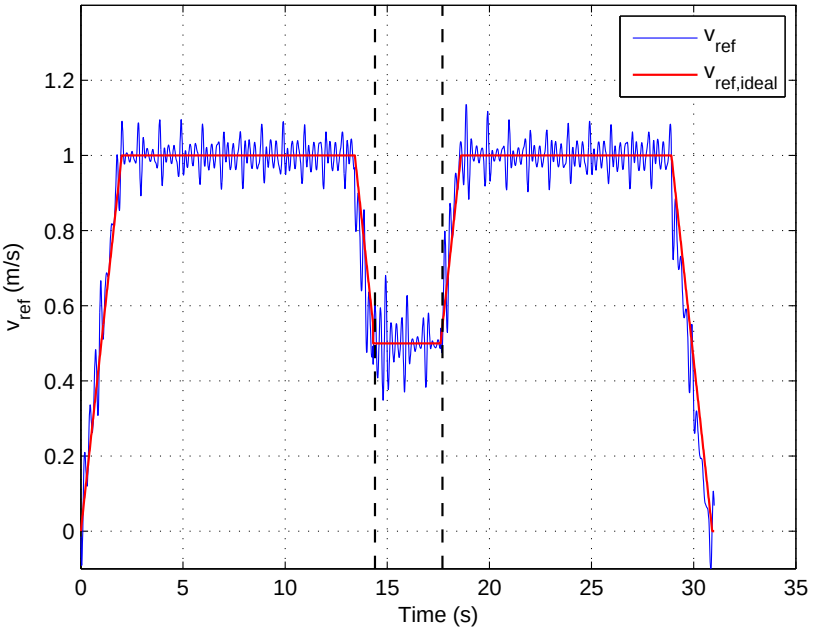

(a) velocity reference

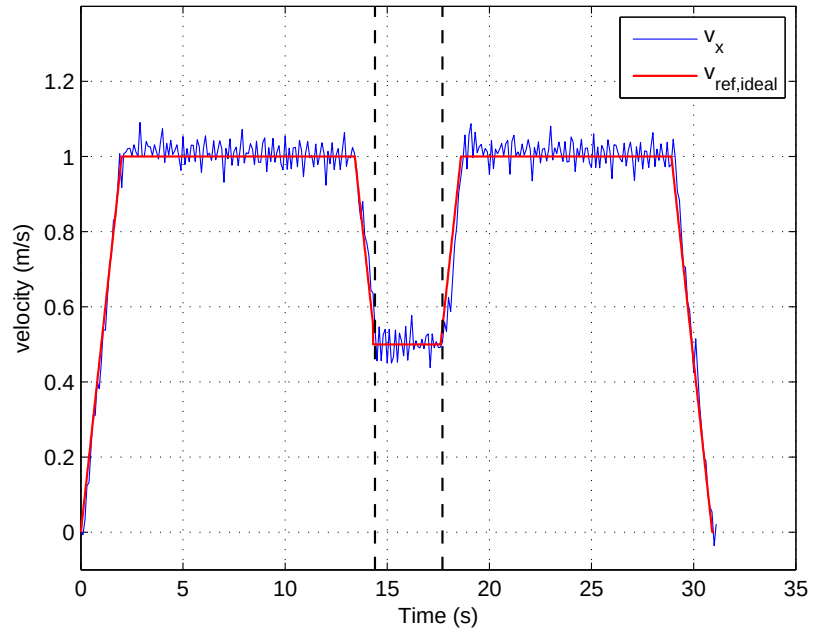

(b) simulated velocity

Fig. 5.17. WMR filtered velocity reference in connection with the related WMR forward velocity of the combined scenario with 20% Parkinsonian and 5% Gaussian noise

In the filtered scenario in Fig. 5.17 the safety bounds have a similar effect on the forward velocity v_x. Here maximum changes of 0.2 $\frac{\text{m}}{\text{s}}$ in $t_s = 0.1$ s are possible. The peak to peak noise amplitude of the forward velocity in Fig. 5.17(b) is only $\frac{1}{2}$ of the reference velocity. In comparison to the scenario without filters used the simulated forward velocity v_x in Fig. 5.17(b) is a big improvement for a smooth driving performance.

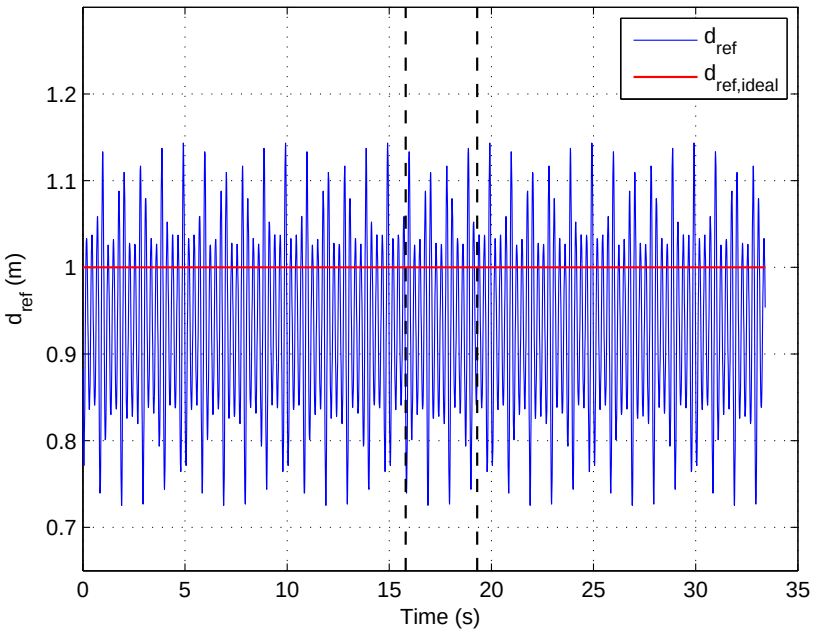

(a) distance to the wall reference

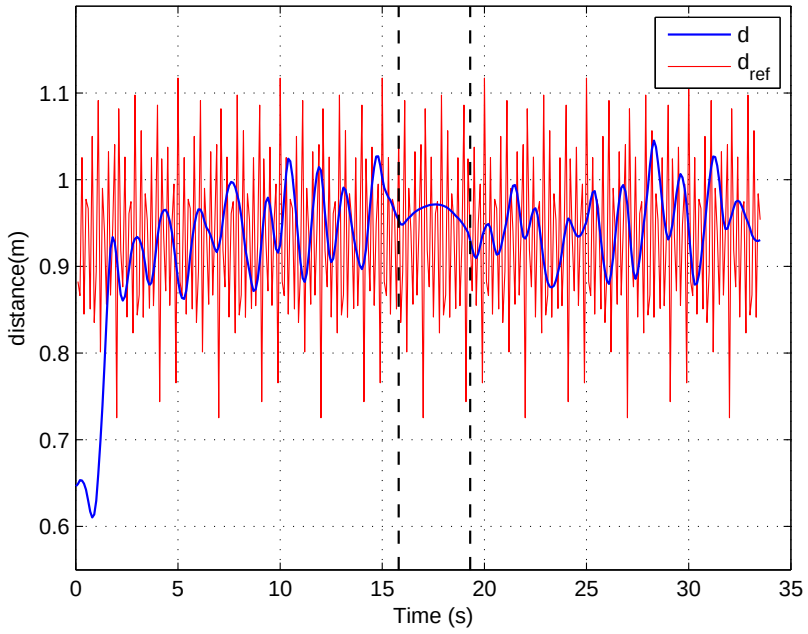

(b) simulated distance to the wall

Fig. 5.18. WMR unfiltered distance reference in connection with the related WMR distance to the wall of the combined scenario with 20% Parkinsonian and 5% Gaussian noise

Similar to the 10% case, in Fig. 5.18(a) the already known 100 Hz distance reference of the unfiltered 20% scenario is displayed. In Fig. 5.18(b) this reference distance is shown in 10 Hz, because this is the way the reference enters in the 10 Hz simulation and impacts the optimization process. Fig. 5.13(b) indicates again the strong desire of the MPC controller to converge to the distance reference. In comparison with the 10% scenario, the oscillations of the simulated distance to the wall in Fig. 5.18(b) are immense and caused by big torques changing the forward direction of the WMR on the way to the goal permanent. The peak to peak oscillations are about 0.1 m. This result shows a bad driving performance. This also indicates that diseased wheelchair users with a similar tremor strength would have problems performing driving tasks on an electric wheelchair without filter strategies used.

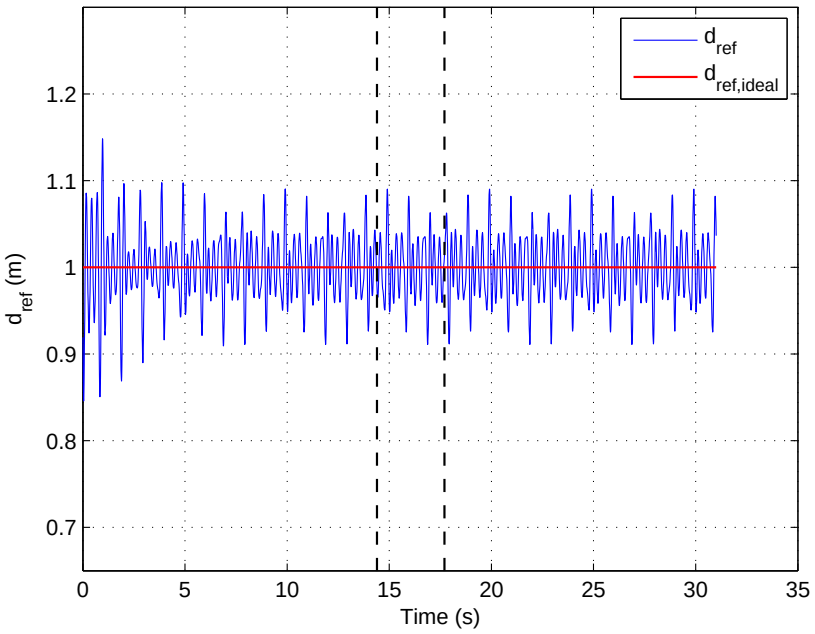

(a) distance to the wall reference

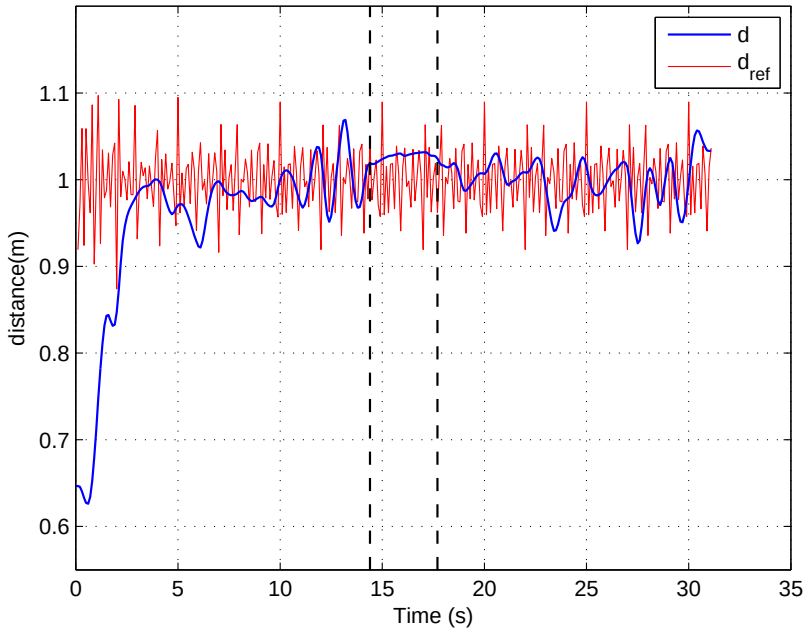

(b) simulated distance to the wall

Fig. 5.19. WMR filtered distance reference in connection with the related WMR distance to the wall of the combined scenario with 20% Parkinsonian and 5% Gaussian noise

In the filtered scenario in Fig. 5.19 the most important point in comparison with the unfiltered scenario are less oscillations in the simulated distance to the wall. Fig. 5.19(b) indicates that for some parts of the scenario no oscillations are possible to see, other parts have oscillations with damped amplitudes. In both diagrams the bias caused by the disease is perfectly erased.

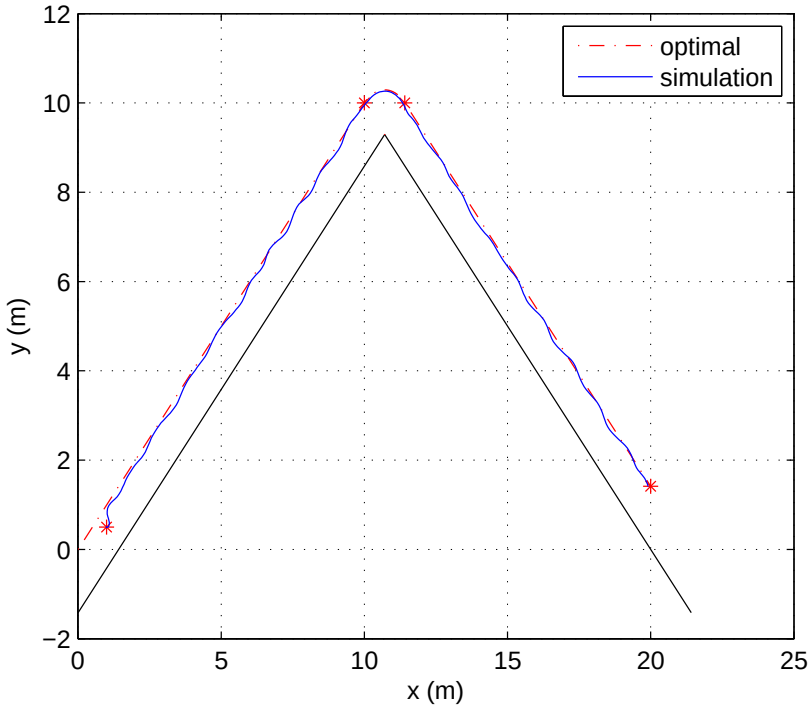

(a) unfiltered

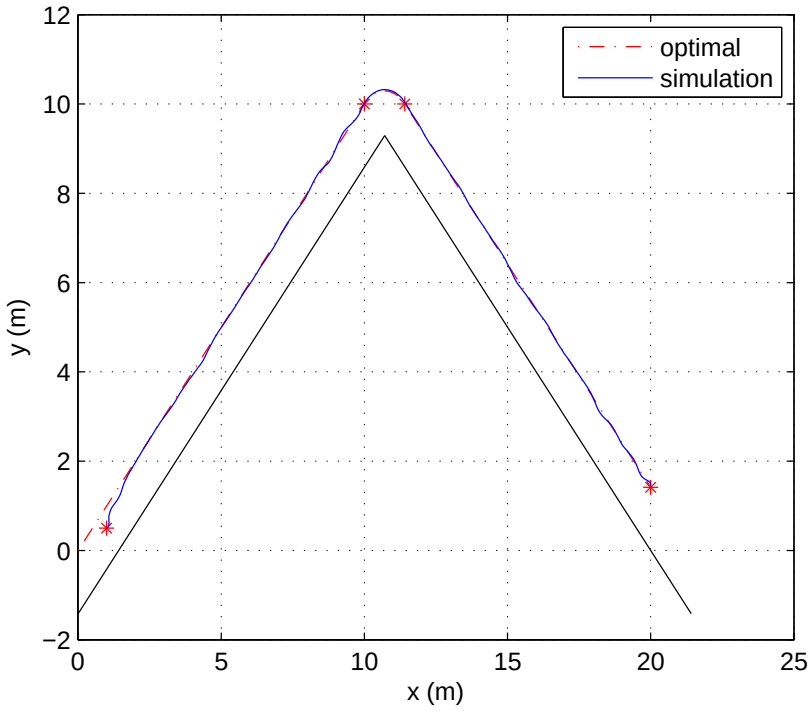

(b) filtered

Fig. 5.20. WMR trajectory of the combined scenario with 20% Parkinsonian and 5% Gaussian noise

In comparison with Fig. 5.20(a) the result of Fig. 5.20(b) shows a very smooth trajectory and an immense improvement. It is not possible to recognize any bigger oscillations. A bias in the trajectory of the WMR is not recognizable. This result supports the utility of our implemented control strategies. It additionally underlines the improved driving performance of the WMR with the filter strategies used and guarantees a safer and smoother driving experience of a diseased user of the electric wheelchair. Although so many uncertainty is imposed on the system in Fig. 5.20(a), this result underlines additionally the robustness of the used MPC control solution.

5.5 Summary of results

Cleary the notch and bias filter achieved the desired objective with significant improvements. In the next chapter we simulate real Parkinsonian tremor on a joystick and apply our approved control and filter strategies.

6. JOYSTICK SIMULATIONS WITH PARKINSONIAN NOISE

6.1 A WMR driving scenario with real joystick data

6.1.1 Introduction of a WMR driving scenario with real joystick data

A real time simulation of the WMR dynamics with a joystick as an input device was designed. The joystick position is interpreted as a torque command, which fulfills the velocity references, rotational velocity references and acceleration references of 100 Hz given by the user.

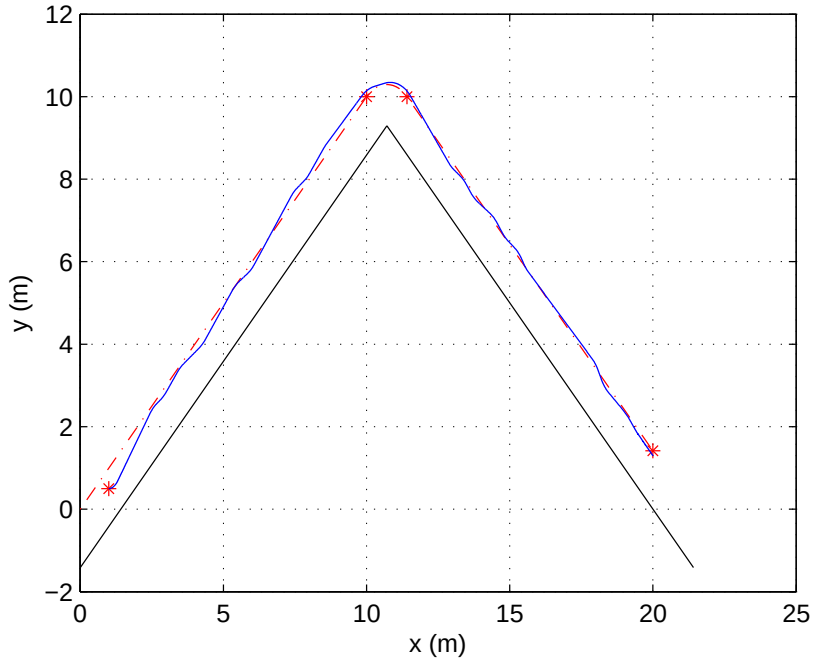

Fig. 6.1. WMR trajectory of the joystick steered scenario of a test user

In Fig. 6.1 a user trying to drive on the red optimal line is shown. The user had no experience with the usage of electric wheelchairs, which explains the small deviation of the optimal line. Because he had visual feedback on a screen, he could compensate his input mistakes similar to a real scenario on a powered wheelchair.

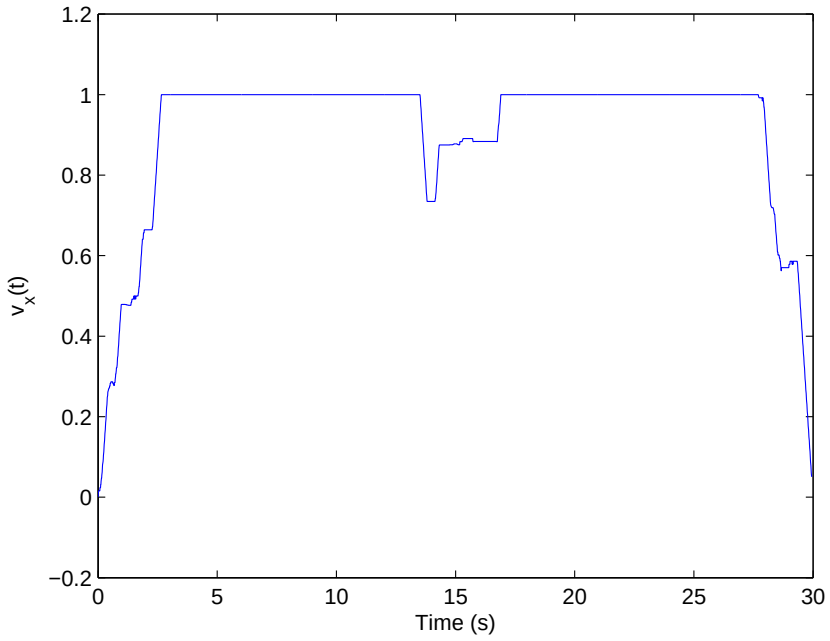

Fig. 6.2. WMR velocity of the joystick steered scenario of a test user

Fig. 6.2 is the forward velocity commanded by the test user. It is possible to see that the shape of his velocity profile is close to our assumptions of velocity references in the past chapters. Constant acceleration and deceleration are used and he tries to maintain a constant driving velocity after he reached a acceptable moving velocity. In the wall following scenarios a similar reference velocity of $1\frac{\mathrm{m}}{\mathrm{s}}$ is used in Fig. 6.2. In the cornering scenario a smaller and nearly constant velocity is used.

For the following simulations with real joystick data references for velocity and distance to the wall have to be defined.

$$v_{ref}(t) = v_{ref,actual}(t) + c_p n_p(t) \tag{6.1}$$

The velocity $v_{ref,actual}(t)$ is the shown actual forward velocity v_x of the WMR as seen in Fig. 6.2. The constant $c_p = \frac{2}{30}$ to mimic a 20% Parkinsonian error with the noise function $n_p(t)$ presented in equation (5.6). For the reference distance to the wall:

$$d_{ref}(t) = d_{exact} + \Delta d_{ref,actual}(t) + c_p n_p(t) = d_{ref,actual}(t) + c_p n_p(t) \tag{6.2}$$

$d_{exact} = 1$ m and $\Delta d_{ref,actual}(t)$ is the deviation from the optimal line in meters based on the underlying real data. Then $d_{ref,actual}(t) = d_{exact} + \Delta d_{ref,actual}(t)$ is the actual calculated distance to the wall of the real joystick data. Again the constant $c_p = \frac{2}{30}$ for a 20% Parkinsonian error with the scaled Parkinsonian noise function $n_p(t)$.

The shown references are the basis for simulations with and without compensation control strategies used. We expect a similar trajectory with the filter and bias shift used. Problematic results for the simulation without these elements used are probable. Then the 100 Hz signals have to be averaged to provide data structure for the following 10 Hz simulation. Therefore the same averaging is used, which provides an additional filter of the raw data.

$$v_{ref}(k) = 0.7 v_{ref}(k) + \frac{1}{30}\left(\sum_{j=1}^{9} v_{ref}(k-j)\right) \tag{6.3}$$

$$d_{ref}(k) = 0.7 d_{ref}(k) + \frac{1}{30}\left(\sum_{j=1}^{9} d_{ref}(k-j)\right) \tag{6.4}$$

The PI used in the following simulations is similar to the PI used in chapter 5. But the angle profile in the cornering part of the scenario is not longer used. This achieves even higher performance, because the optimization is only orientating itself at the velocity and distance to the wall references given. This proves that the cornering,

which is even more complex than the wall following part, can be simulated with a MPC prediction horizon of 0.4 s.

Table 6.1
Weight coefficients in the real joystick data scenarios

	c_{xf}	c_d	c_v	c_e	c_θ	c_n	c_p
wall following	10	1.5	10	0.01	0	0.05	$\frac{2}{30}$
cornering	0	1.5	10	0.01	0	0.05	$\frac{2}{30}$

6.1.2 Simulation of the WMR driving scenario with 20 percent Parkinsonian noise

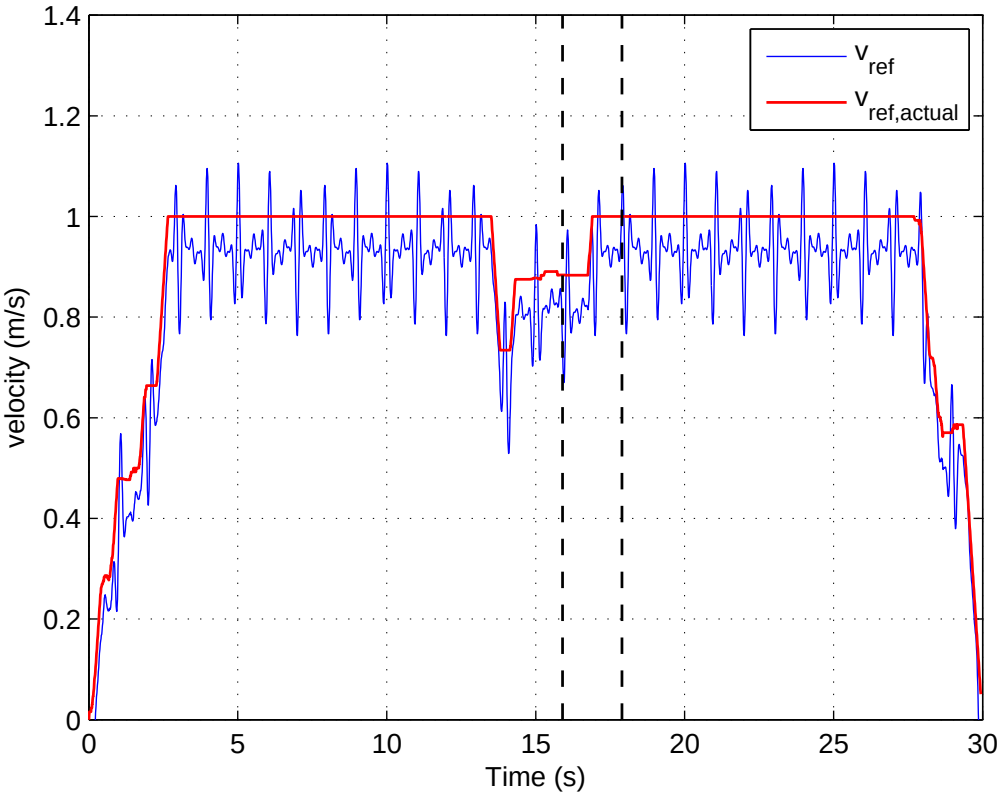

Fig. 6.3. WMR velocity reference of the unfiltered real joystick data scenario with 20% Parkinsonian noise

In Fig. 6.3 the velocity reference v_{ref} calculated at 100 Hz shows the influence of the 20% Parkinsonian noise on the actual velocity reference $v_{ref,actual}$, performed by the wheelchair user via joystick. Similar to chapter 5 the bias influence and the peak to peak noise of about $0.3\frac{\mathrm{m}}{\mathrm{s}}$ is easy to recognize.

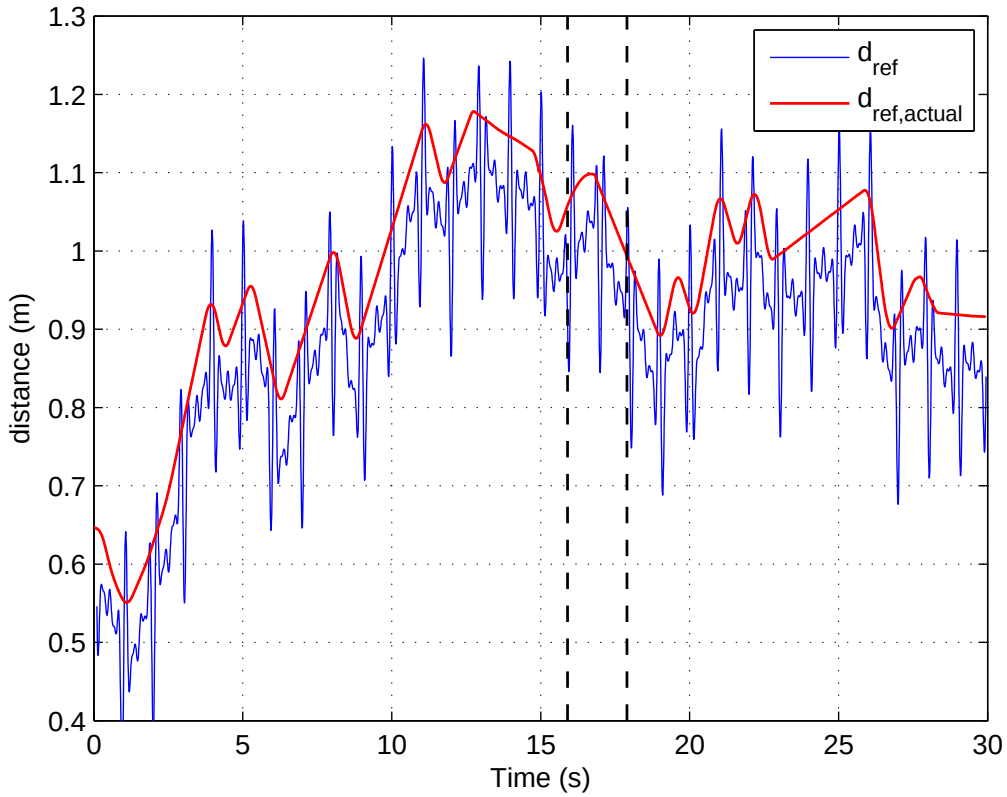

Fig. 6.4. WMR distance to the wall reference of the unfiltered real joystick data scenario with 20% Parkinsonian noise

In Fig. 6.4 the same influence in bias and peak to peak noise on the real data $d_{ref,actual}$ is present.

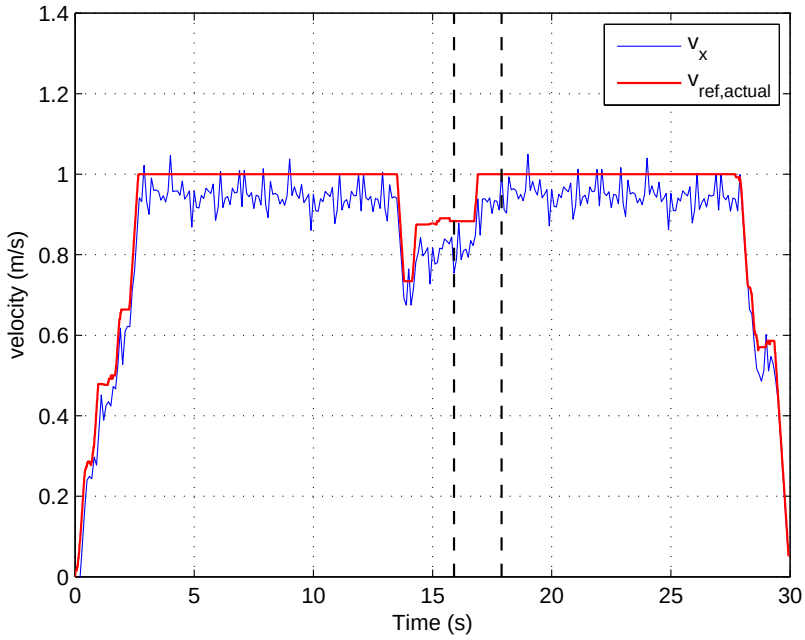

Fig. 6.5. WMR trajectory of the unfiltered real joystick data scenario with 20% Parkinsonian noise

Fig. 6.5 shows the influence of Parkinsonian noise on the forward velocity v_x. The negative bias and the slower forward velocity compared to the real data is causing changes in the time the WMR reaches and finishes the cornering part of the scenario. The peak to peak noise amplitude of only $0.1\frac{\mathrm{m}}{\mathrm{s}}$ is due to the dynamics of the system and the safety bounds of the system on acceleration.

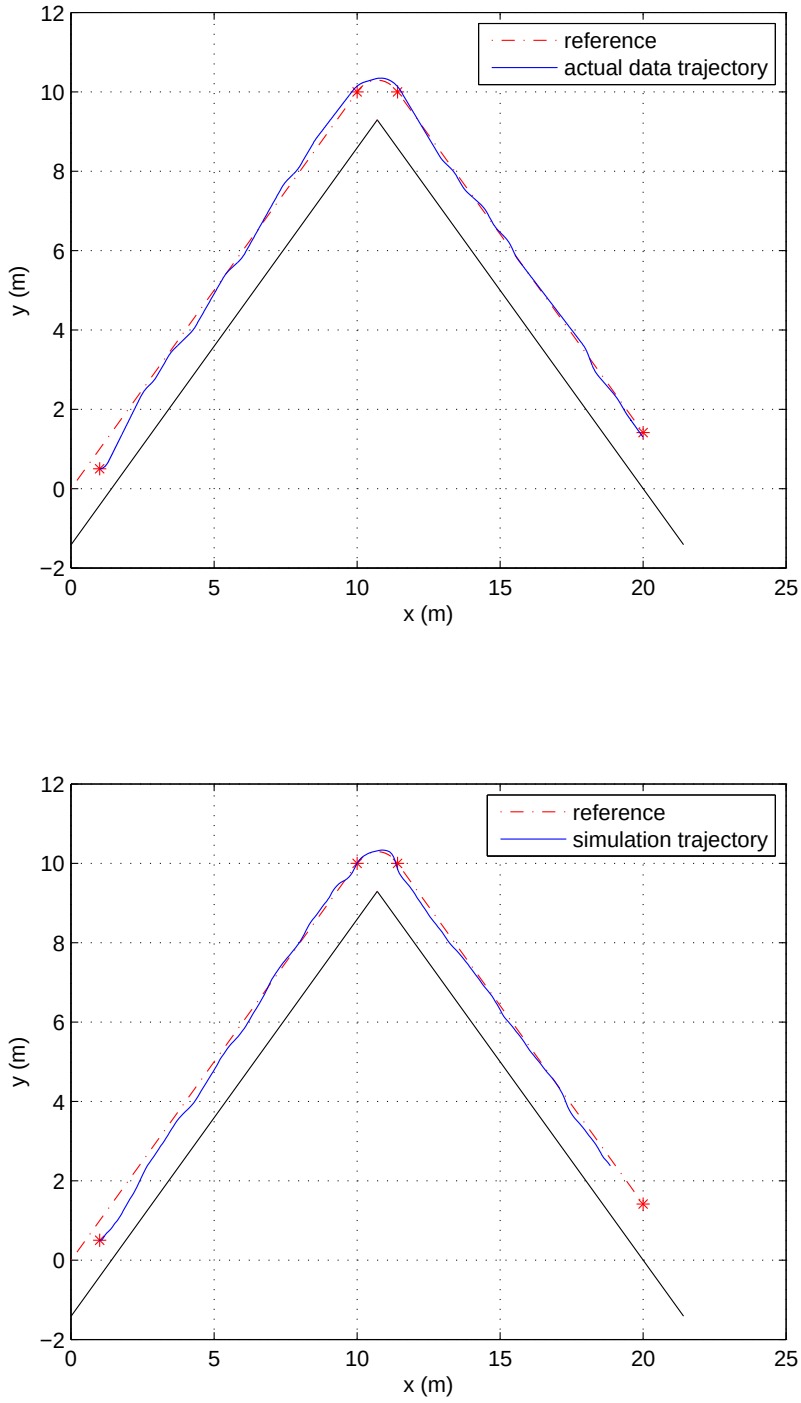

Fig. 6.6. WMR trajectory of the unfiltered real joystick data scenario with 20% Parkinsonian noise

As seen in Fig. 6.5 the Parkinsonian noise causes the WMR to drive slower. With the given limited data it is not possible to reach the final goal in Fig. 6.6. The lower velocity reference designed for the cornering scenario is shifted more into the end of the first wall following scenario. It is easy to see that both trajectories compared don't have a common behavior.

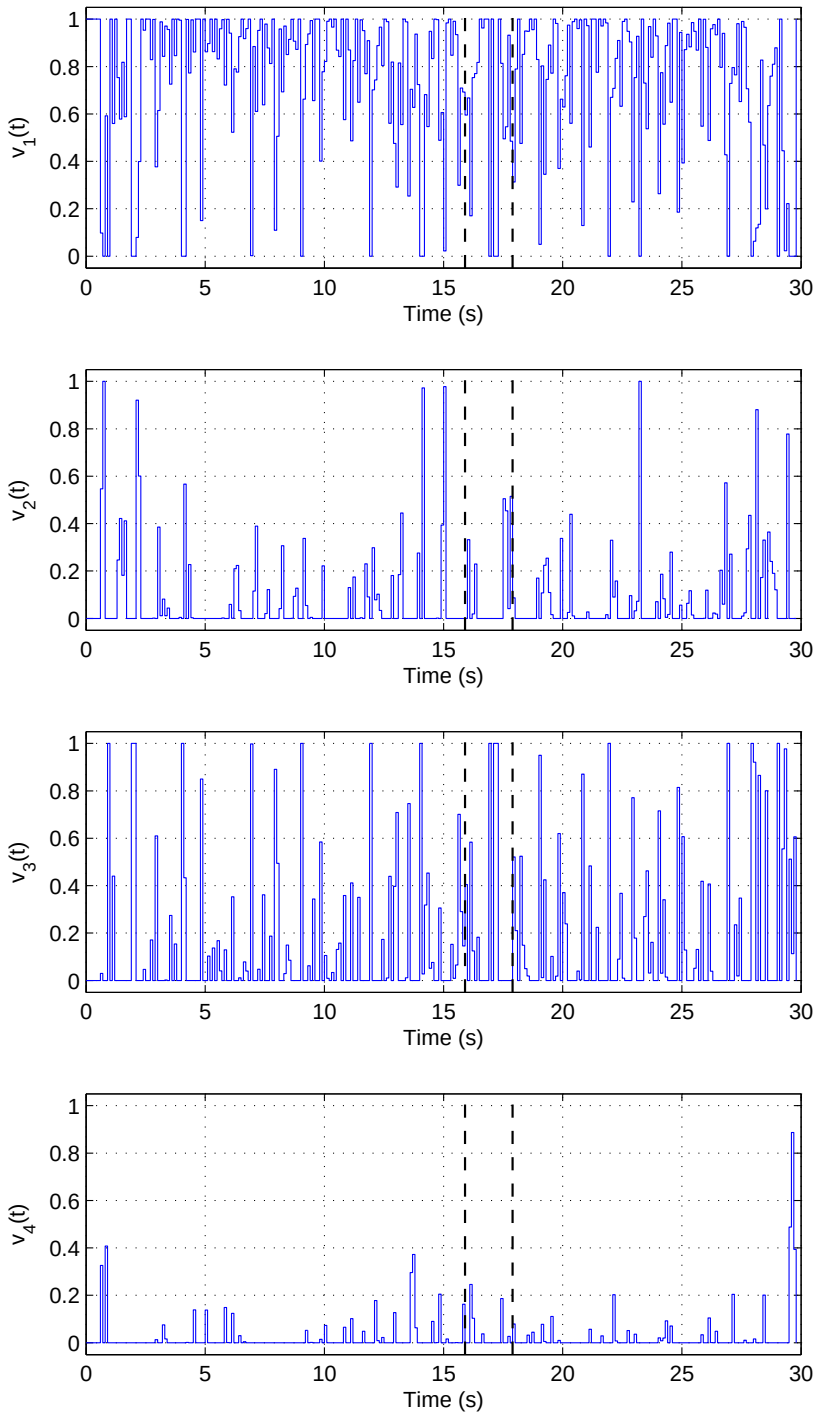

Fig. 6.7. WMR mode values of the unfiltered real joystick data scenario with 20% Parkinsonian noise

As expected due to the noise mode 1 is not as dominant as in other simulations. This driving scenario would not be useful for an electric wheelchair user, because Fig. 6.7 shows a lot of influence of mode 2,3 and 4. That means propel and brake is used in an alternate way too much. In past simulations a dominant mode 1 was a sign of smoothness in trajectory and velocity.

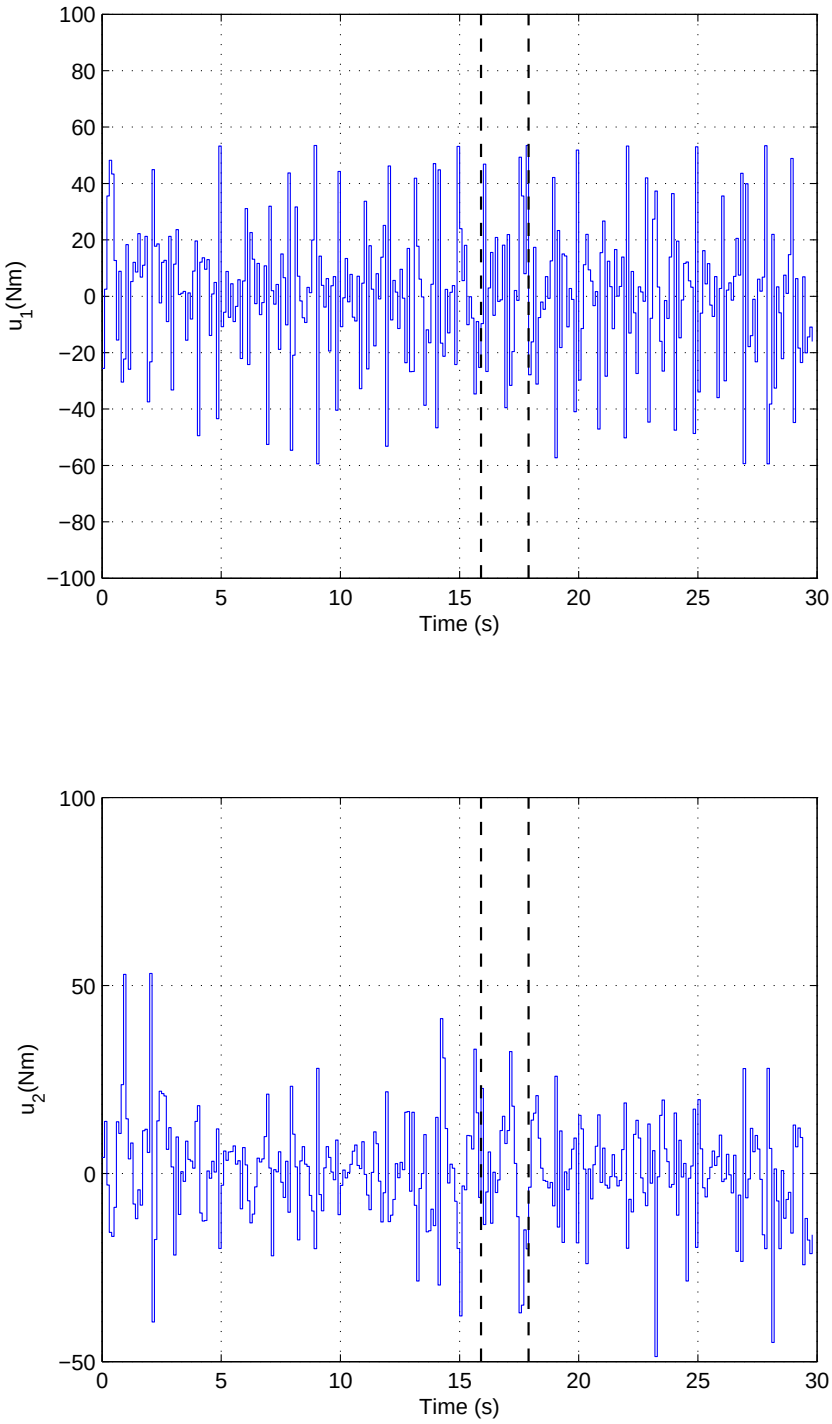

Fig. 6.8. WMR control inputs of the unfiltered real joystick data scenario with 20% Parkinsonian noise

In addition to the mode diagram, Fig. 6.8 reveals that high torques are used to follow the velocity and distance to the wall references. The bounds on torques with 60 Nm and -60 Nm are reached in some intervals in Fig. 6.8. That means without filter strategies used the 20% Parkinsonian noise scenario results show impressively the necessity of our filter strategies.

6.1.3 Simulation of the WMR driving scenario with 20 percent Parkinsonian noise and control strategies used

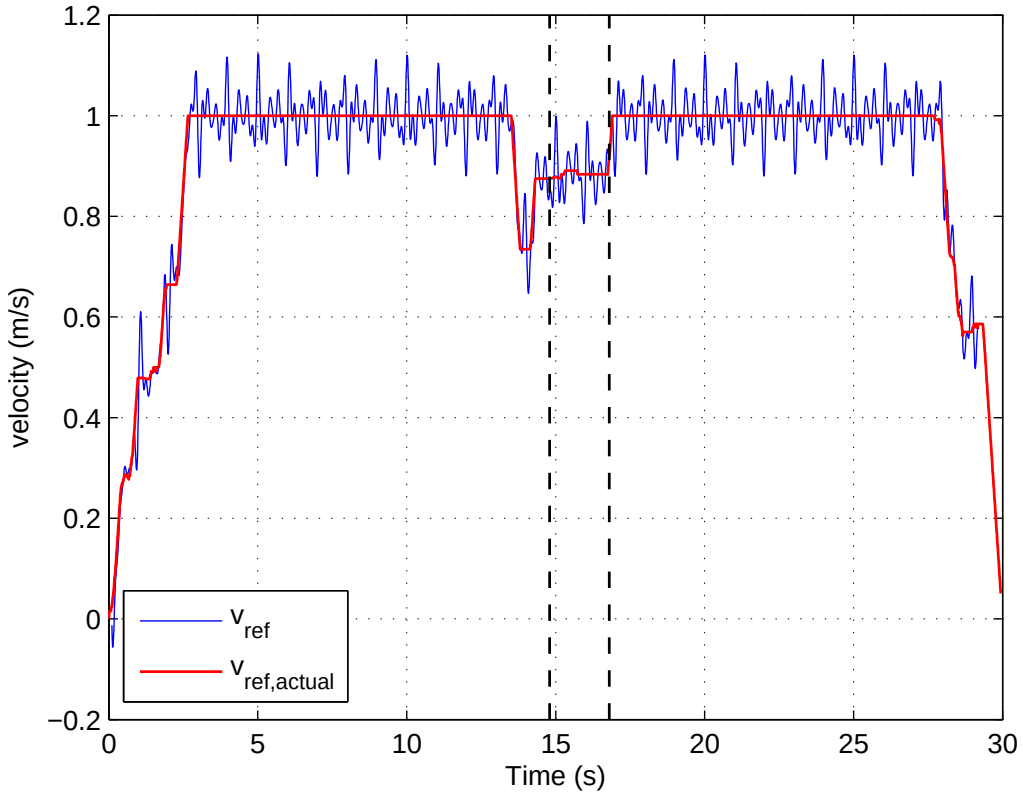

Fig. 6.9. WMR velocity reference of the filtered real joystick data scenario with 20% Parkinsonian noise

In Fig. 6.9 the effects of the filter strategies used can be seen. The bias is out of the calculation and the peak to peak noise amplitude is shrinking to $0.2\frac{\mathrm{m}}{\mathrm{s}}$. These differences in comparison to Fig. 6.3 have an positive impact on the driving behavior of the WMR.

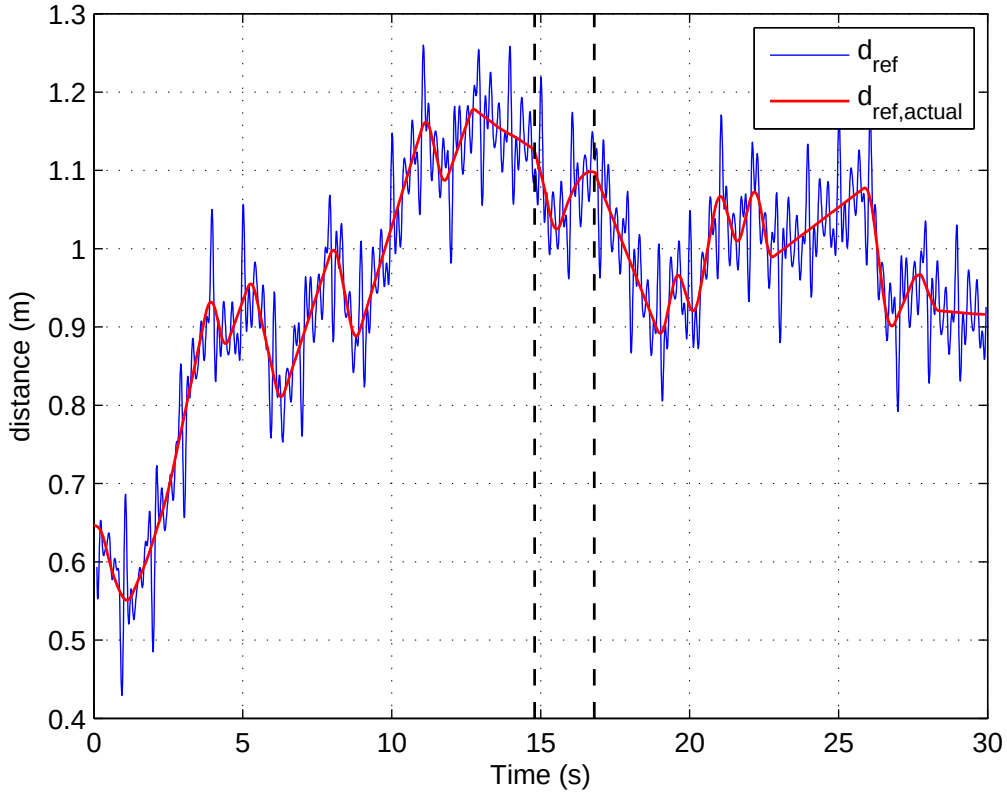

Fig. 6.10. WMR distance to the wall reference of the filtered real joystick data scenario with 20% Parkinsonian noise

In Fig. 6.10 a similar positive effect on the distance to the wall reference is easily detectable. To achieve a smaller peak to peak amplitude the used filter erases the main lobe of the Parkinsonian frequency content.

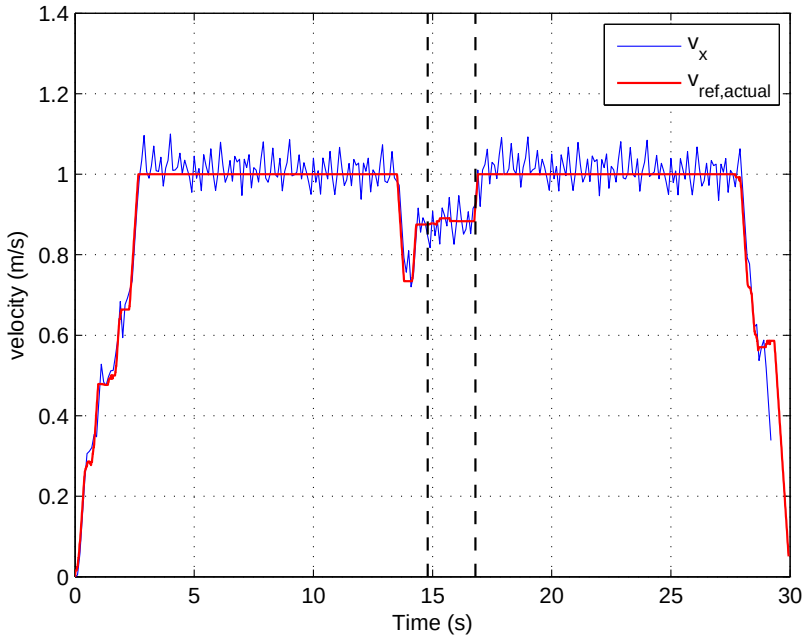

Fig. 6.11. WMR forward velocity of the filtered real joystick data scenario with 20% Parkinsonian noise

As seen in Fig. 6.11 the mean of forward velocity v_x of the WMR matches the actual joystick data. The peak to peak noise is much smaller than in the filtered scenario, which supports the achievements reached with the used filter strategies in the real joystick data scenario.

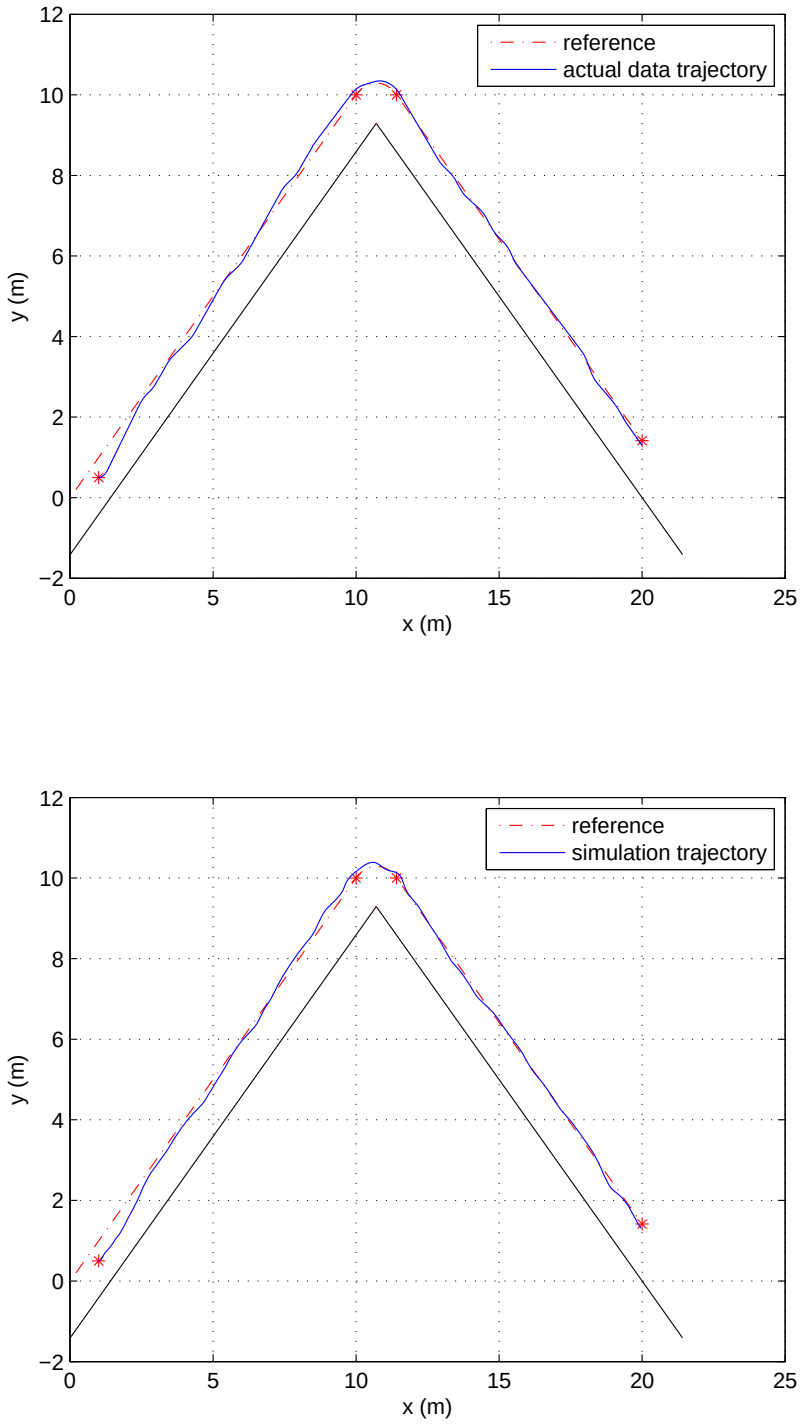

Fig. 6.12. WMR trajectory of the filtered real joystick data scenario with 20% Parkinsonian noise

As seen in Fig. 6.12 both trajectories look very similar. That shows that the used filter strategies are erasing a high percentage of the Parkinsonian noise influencing the system. In this case the actual joystick data is approximately reproduced and following a similar driving performance is reached.

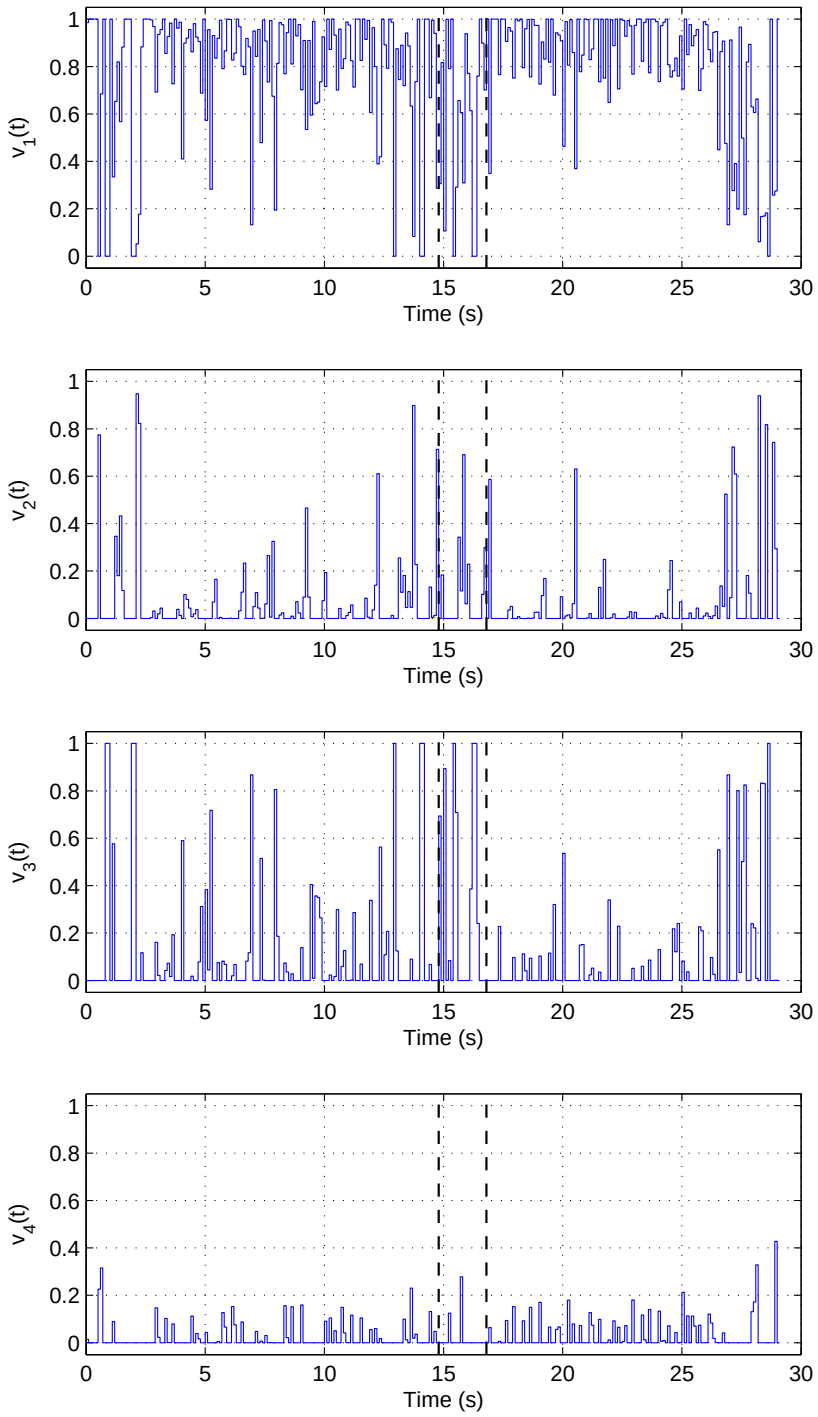

Fig. 6.13. WMR mode values of the filtered real joystick data scenario with 20% Parkinsonian noise

The mode value diagram in Fig. 6.13 underlines the good results in velocity and trajectory plots. In mode 1, where both wheels propel, higher mode values $v_1(t)$ over all intervals can be seen. This dominance of mode 1 is responsible for better and smoother results in trajectory and velocity and shows again the success of the taken filter strategies.

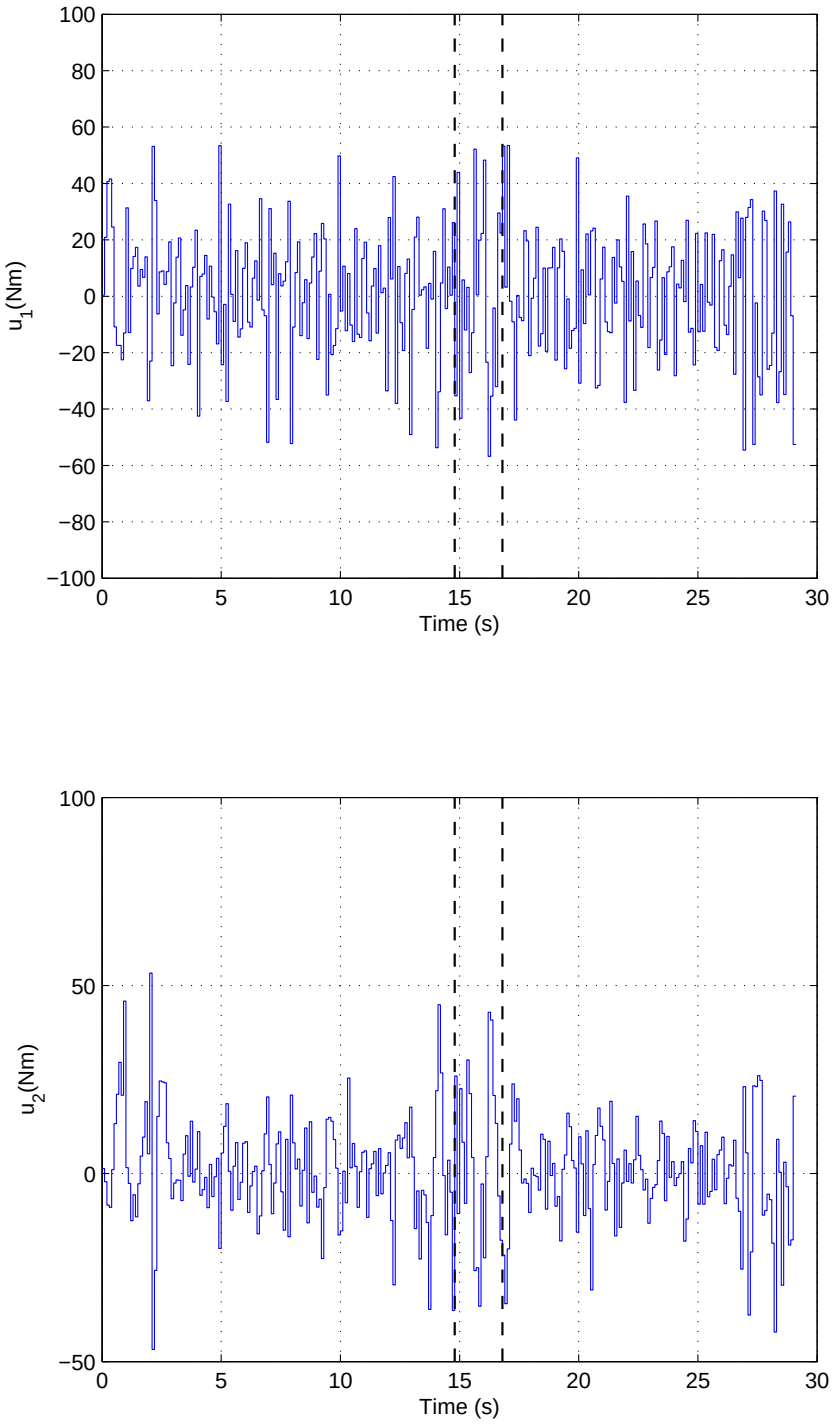

Fig. 6.14. WMR control inputs of the filtered real joystick data scenario with 20% Parkinsonian noise

In Fig. 6.14 the input torques reflect what was already predicted through the good performance in trajectory and velocity plots. Less input torque is used in the simulation, which means that less corrections in direction and speed were taken. This is a result based on the filtered and smoother velocity and distance to the wall references.

6.2 Summary of the WMR driving scenario with real joystick data

One of the main results of this chapter is that Parkinsonian noise imposed on real joystick data has on one hand fatal influence on the driving behavior of a human. On the other hand it was possible to achieve similar good driving performance with filter strategies used and to approximately duplicate the reference scenario. These results are so close to the real joystick data that it is possible to support the use of our filter strategies for further implementations immensely. This would improve life quality of wheelchair users with Parkinson's disease significantly.

7. FURTHER RESEARCH AND PERSPECTIVES

In the last chapter of the thesis changes in the model are presented to improve the driving performance. Additionally the possibility to use the filter strategies for the disease multiple sclerosis is shown.

7.1 Improvements in the WMR model

In this section changes of the terms in the nonlinear constraints of the optimization process and a change of the modes are displayed.

7.1.1 Changes in the regenerative braking term

In this thesis the regenerative braking was depending on the rotational velocity of the wheel only and had a fixed value in the model. The constant $K_b = 10$ has a fixed value and the following equation (7.1) for the input torques fulfills the continuity condition:

$$u_{(i)} = \begin{cases} -K_b \mathrm{w}_i, & \text{if } |\mathrm{w}_i| \leq 6 \\ -60\mathrm{sgn}(\mathrm{w}_i) & \text{if } |\mathrm{w}_i| > 6 \end{cases} \quad i = 1, 2 \tag{7.1}$$

This means if you want to regenerative brake in a wanted constant deceleration scenario, the regenerative braking mode on both wheels v_4 is only able to deliver a specific torque based on the rotational velocity of the wheel that provides a specific deceleration rate. The related value v_4 and the impact of regenerative braking on the system have to change every time depending on the actual fixed special torque given to provide the same wanted deceleration rate. The solution to this problem is the integration of a modulator $m_i(t)$ for each wheel i,$i\epsilon\{1, 2\}$ in the model. The regenerative braking of the system provides a fixed value of torque that is directly

applied on the wheels. In the new implementation the power provided by regenerative braking is only partially with a factor of $m_i(t)$ transferred on the wheels. The modulator $m_i(t)\epsilon\,[0,1]$ can then be used in the system with the following equation:

$$u_{(i)} = \begin{cases} -m_i(t)K_b \mathrm{w}_i, & \text{if } |\mathrm{w}_i| \leq 6 \\ -m_i(t)60\mathrm{sgn}(\mathrm{w}_i) & \text{if } |\mathrm{w}_i| > 6 \end{cases} \quad i = 1,2 \tag{7.2}$$

Before this integration the regenerative braking mode was a one to one mapping from rotational velocity of a wheel to input torque. With given velocity profiles in simulations, the optimization process had to use changes in the mode values to regulate the impact of regenerative braking. With the modulator that can change over time immediately a new dimension is added to the system. The regenerative braking mode is not longer a one to one mapping but a line, where the optimal point can be found in the process of optimization. This is giving a lot of value to the regenerative braking mode. As one result the mode values of regenerative braking will be a lot higher in deceleration scenarios. The effects are caused by the flexibility given to the regenerative braking mode.

7.1.2 Mode changes in the WMR model

In this thesis a convex combination of mode values is used, but for both wheels already combined.

$$\begin{aligned} v_1 &= \text{wheel 1 propelling and wheel 2 propelling} \\ v_2 &= \text{wheel 1 propelling and wheel 2 braking} \\ v_3 &= \text{wheel 1 braking and wheel 2 propelling} \\ v_4 &= \text{wheel 1 braking and wheel 2 braking} \end{aligned} \tag{7.3}$$

A different approach is to divide the mode in two main modes, each representing the behavior of a related wheel. In each wheel mode a convex combination of propelling and braking is used.

$$\begin{aligned} v_1 &= \text{wheel 1 where:} \\ v_{1p} &= \text{wheel 1 propelling} \\ v_{1b} &= \text{wheel 1 braking} \\ v_{1p} + v_{1b} &= 1 \end{aligned} \tag{7.4}$$

$$\begin{aligned} v_2 &= \text{wheel 2 where:} \\ v_{2p} &= \text{wheel 2 propelling} \\ v_{2b} &= \text{wheel 2 braking} \\ v_{2p} + v_{2b} &= 1 \end{aligned}$$

With this new approach it is possible to look at each wheel mode independently, which gives more freedom to the system and it closer to a real scenario implementation.

7.2 Adaptivity of the control strategies to multiple sclerosis tremor

Multiple sclerosis (MS) tremor is affecting the driving behavior of a powered wheelchair user in a similar negative way as Parkinsonian tremor does. But there are major differences in the frequency range of the tremor. In comparison to Parkinsonian postural tremor the multiple sclerosis postural tremor in fingers has two main frequency ranges. The first space is between 2 Hz and 4 Hz. The other important frequency range is between 6 Hz and 10 Hz. [17] The two tremor frequency ranges superimpose to the actual MS tremor. Every limb can have different frequencies similar to Parkinsonian noise. It is important to mention that the actual frequencies with high tremor power are close to tremors healthy elderly people develop. The actual tremor power in MS is doubled in comparison. [17] With the use of two notch filters in the control strategy

the problem can be solved and a huge amount of tremor influenced movements can be erased.

LIST OF REFERENCES

LIST OF REFERENCES

[1] A. Dovzhenok and L. L. Rubchinsky, "On the origin of tremor in parkinsons disease," *PloS one*, vol. 7, no. 7, p. e41598, 2012.

[2] G. Deuschl, J. Raethjen, R. Baron, M. Lindemann, H. Wilms, and P. Krack, "The pathophysiology of parkinsonian tremor: a review," *Journal of neurology*, vol. 247, no. 5, pp. V33–V48, 2000.

[3] A. Lemstra, L. Verhagen Metman, J. Lee, P. Dougherty, and F. Lenz, "Tremor-frequency (3–6 hz) activity in the sensorimotor arm representation of the internal segment of the globus pallidus in patients with parkinson's disease," *Neuroscience letters*, vol. 267, no. 2, pp. 129–132, 1999.

[4] P. E. O'Suilleabhain and J. Y. Matsumoto, "Time-frequency analysis of tremors.," *Brain*, vol. 121, no. 11, pp. 2127–2134, 1998.

[5] P. Rack, "Stretch reflexes and parkinsonian tremor," in *Advances in Stereotactic and Functional Neurosurgery 7*, pp. 51–53, Springer, 1987.

[6] B. Hellwig, P. Mund, B. Schelter, B. Guschlbauer, J. Timmer, and C. Lücking, "A longitudinal study of tremor frequencies in parkinsons disease and essential tremor," *Clinical Neurophysiology*, vol. 120, no. 2, pp. 431–435, 2009.

[7] H. Choset, K. M. Lynch, S. Hutchinson, G. A. Kantor, W. Burgard, L. E. Kavrak, and S. Thrun, *Principles of Robot Motion: Theory, Algorithms, and Implementations*. Reading Massachusetts: MIT Press, 2005.

[8] S. Wei, K. Uthaichana, M. Žefran, and R. A. DeCarlo, "Hybrid Model Predicitive Control for the Stabilization of Wheeled Mobile Robots Subject to Wheel Slippage," *IEEE Transactions on Control Systems Technology*, vol. Preprint, 2013.

[9] M. Oishi, P. Taghipour Bibalan, and A. Cheng, "Modeling and Control of a Powered Wheelchair: Wall-Following Around a Corner with Infrared," in *Proceedings of the 23rd CANCAM*, pp. 25–28, 2011.

[10] G. U. Sorrento, P. S. Archambault, F. Routhier, D. Dessureault, and P. Boissy, "Assessment of Joystick control during the performance of powered wheelchair driving tasks," *Journal of neuroengineering and rehabilitation*, 2011.

[11] K. L. Howie Choset and, S. Hutchinson, G. Kantor, W. Burgard, L. Kavaki, and S. Thrun, *Principles of Robot Motion*. Cambridge, Massachusetts: The MIT Press, 2005.

[12] MaxBotix Inc., "Xl-maxsonar-ez series high performance sonar range finder." `http://www.maxbotix.com/documents/XL-MaxSonar-EZ_Datasheet.pdf`. [Online; accessed September 23, 2013].

[13] S. Morrison, N. Cortes, K. Newell, P. Silburn, and G. Kerr, "Variability, regularity and coupling measures distinguish pd tremor from voluntary 5hz tremor," *Neuroscience letters*, 2012.

[14] I. D. Loram, P. J. Gawthrop, and M. Lakie, "The frequency of human, manual adjustments in balancing an inverted pendulum is constrained by intrinsic physiological factors," *The Journal of physiology*, vol. 577, no. 1, pp. 417–432, 2006.

[15] T. Heida, E. C. Wentink, and E. Marani, "Power spectral density analysis of physiological, rest and action tremor in parkinsons disease patients treated with deep brain stimulation," *Journal of neuroengineering and rehabilitation*, vol. 10, no. 1, p. 70, 2013.

[16] L. De Wet and W. Van Aswegen, "Determining the usability of computer input devices by parkinsons disease sufferers.," *South African Family Practice*, vol. 47, no. 1, 2005.

[17] S. Morrison, J. Sosnoff, B. Sandroff, J. Pula, and R. Motl, "The dynamics of finger tremor in multiple sclerosis is affected by whole body position," *Journal of the neurological sciences*, 2012.